

**3D GROUND-PENETRATING RADAR (GPR) INVESTIGATIONS:
BURIED CULVERTS, HISTORICAL GRAVES, A SANDSTONE RESERVOIR
ANALOG, AND AN IMPACT CRATER**

A Dissertation Presented to
the Faculty of the Department of Earth and Atmosphere Sciences
University of Houston

In Partial Fulfillment
of the Requirements for the Degree
Doctor of Philosophy

By
Azie Sophia Aziz
May 2016

**3D GROUND-PENETRATING RADAR (GPR) INVESTIGATIONS:
BURIED CULVERTS, HISTORICAL GRAVES, A SANDSTONE RESERVOIR
ANALOG, AND AN IMPACT CRATER**

Azie Sophia Aziz

APPROVED:

Robert R. Stewart, Ph.D.
Department of Earth and Atmosphere Sciences

Shuhab D. Khan, Ph.D.
Department of Earth and Atmosphere Sciences

Robert Wiley, Ph.D.
Department of Earth and Atmosphere Sciences

Jacob Borgerson, Ph.D.
Paradigm Consultants, Inc.

Dan Wells, Ph.D.
Dean, College of Natural Sciences and Mathematics

ACKNOWLEDGEMENTS

I would never have been able to complete my Ph.D. dissertation without the support and guidance of my research advisor, committee members, colleagues, family, and friends. I would like to express my sincere gratitude toward Dr. Robert R. Stewart for his unconditional support, guidance, and patience in developing my background in geophysical research and my journey as a graduate student. I thank you for letting me experience the research in GPR and patiently reviewing my writing. I also want to thank Dr. Shuhab D. Khan for technical input, ideas, and suggestions. I give many thanks to Dr. Robert Wiley, who gave his idea about geophysical computation and gave me great help in the field acquisition at the Mueschke Cemetery. I would like to thank Dr. Jacob Borgerson of Paradigm Consultants, Inc. for his continuous feedback on the dissertation content. I would like to thank Susan Green, as a good friend and co-author, who trained me to use GPR and always was willing to help with acquiring data and providing her best technical feedback. I also want to thank the SEG and the Department of Earth and Atmosphere Sciences at the University of Houston for providing some of the financial assistance throughout my studies. I also want to thank my colleagues at the Department of Earth and Atmospheric Sciences for their support during my research: Sharon, Andrew, Jingjing, Jiannang, Fabiola, Long, Chris, Andrea, Abby, Vaughn, Li, Ramya, Proma.

I express my appreciation to Adrian Smith of the University of Calgary for providing PSDM imaging code. I would like to thank Mr. Brian Kyser of Lone Star College-North

Harris for initiating this geo-archaeological work. I give my gratitude to Mr. Marcus Zinecker and Ms. Yesenia Rivera for the assistance they gave me in acquiring the GPR data at the Mueschke Cemetery. I also thank Mrs. Rebecca Stone of the Mueschke Cemetery Association, whose grandparents are buried at Mueschke Cemetery, for permission to perform the excavation near the cemetery and for the oral histories she related to me. I want to thank Mr. Greg Johnson, Ms. Marie Chong, and Mr. Chris Martin of Sensors & Software for the software license and the constructive technical feedback they provided. Thank you to Mr. Ady Geda and Ms. Joan-Marie Blanco, who helped during the excavation. I appreciate the work of Dr. Nikolay Dyaurov of the Allied Geophysical Lab (AGL) for preparing the soil samples and Dr. Yinxu Zhang of the Well Logging Lab at the Department of Electrical Engineering of the University of Houston for conducting the dielectric constant and conductivity experiment. I offer my gratitude to Mr. Greg Sill and the Geochemistry Lab of the University of Houston for the soil moisture experiment. I also want to acknowledge Mr. Darren Hauser of the National Center for Airborne Laser Mapping for the TLS survey. I am grateful to Mr. Li Chang and Ms. Vaughn Robla for the CMP survey. I am grateful to Dr. Julia Wellner, Ms. Yuribia Munoz, and Ms. Helena Manuel of the Wellner Sedimentology Lab at The University of Houston for providing the equipment and assisting me to perform the soil grain size experiment. I give my appreciation to Mr. Ismail Abir, Ms. Aubrey Hepler and Mr. William Savage for the TLS processing guidance. I am grateful to Ms. Larkin Spires and Dr. Stephanie Ingle for reading my dissertation and providing corrections. I would like to thank my colleagues at Lumina Geophysical for their technical suggestion and support. I am also grateful to Dr. Claudio Patriarca of Statoil for the continuous technical guidance in GPR. I am thankful to Reza

Iskandar, Marlin Murdock, Dr. Anastasija Cabolova and Dr. Andrew Melkonian for their support throughout my Ph.D. studies.

I would also like to thank my parents and six siblings in Malaysia who always support me unconditionally. Finally, I would like to thank Joseph McNally, who was always there to ensure that I was on the right track towards my graduation and stood by me through the bad and good times. I could not have made it without you.

To my Mother and my Father, Siti and Aziz.

**3D GROUND-PENETRATING RADAR (GPR) INVESTIGATIONS:
BURIED CULVERTS, HISTORICAL GRAVES, A SANDSTONE RESERVOIR
ANALOG, AND AN IMPACT CRATER**

An Abstract of a Dissertation

Presented to

the Faculty of the Department of Earth and Atmosphere Sciences

University of Houston

In Partial Fulfillment

of the Requirements for the Degree

Degree of Philosophy

By

Azie Sophia Aziz

May 2016

ABSTRACT

Ground-penetrating radar (GPR) is used to characterize a variety of subsurface targets such as buried culverts, historical graves, reservoir analogs, and impact craters. In the first case of “buried culverts” I evaluated the GPR performance across five antenna frequencies to determine which would best image buried culverts. Laboratory measurements of soil were made to provide independent measurements to compare measurements and estimates from the field experiments and other sources. Estimates of radar velocities for the set of GPR antenna frequencies were made by a variety of GPR processing techniques together with survey measurements. These velocities were then used in the imaging and time-to-depth conversion of the GPR data. The best velocity used for the various migrations showed a frequency dependence. In the second case of “historical graves” Terrestrial Laser Scanning (TLS) was used before GPR to provide an elevation map of the survey area. This map was analyzed to find anomalous mounds and depressions which provided leads to the location of undocumented graves that could be surveyed in depth with GPR for verification. In the third case of “reservoir analogs” I used 3D GPR to visualize the internal structure of terminal distributary mouth bars in the Cretaceous Ferron Sandstone in southeastern Utah. Three radar facies were observed including a terminal distributary channel of 1.25 m thickness filled with distributary mouth bars, a progradational mouth bar with a dip angle of approximately 20° , and a laterally continuous basal planar bed. GPR images revealed the geometry of architectural elements such as small-scale bedding (0.6

m) and the extent (9 m) of major bounding surfaces. In the fourth case of “craters” I used 3D GPR to image ejecta elements and to map the alluvium thickness at the Barringer (Meteor) Crater in Arizona. Some software was developed to assist the processing. Workflows were developed for TLS data and 3D GPR data. The results for all four cases were interpreted successfully and recommendations for future acquisition, processing, and interpretation were compiled. The wide range of imaging cases shows the usefulness of GPR in the imaging of buried culverts, historical graves, reservoir analogs, and impact craters.

CONTENTS

ACKNOWLEDGEMENTS	iii
ABSTRACT	viii
CONTENTS	x
LIST OF FIGURES	xiv
Chapter 1:	xiv
Chapter 2:	xiv
Chapter 3:	xvii
Chapter 4:	xxiii
Chapter 5:	xxv
Appendix:	xxvii
LIST OF TABLES	xxix
Chapter 2	xxix
Chapter 3	xxix
Chapter 4	xxix
LIST OF ABBREVIATIONS	xxx
LIST OF SYMBOLS	xxxii
1 INTRODUCTION	1
1.1 Background	1
1.2 Research gaps and significance	2
1.3 Research aims and objectives	8
1.4 Thesis structure	10
1.5 Research contributions	11
References	12
2 IMAGING BURIED CULVERTS USING 3D GROUND-PENETRATING RADAR (GPR) WITH VARYING ANTENNA FREQUENCIES (100 MHZ -1 GHZ)	17
Abstract	17
2.1 Introduction	18

2.2	Test site	20
2.3	Soil measurement and numerical modeling	21
2.4	Data acquisition.....	23
2.5	Data processing	28
2.6	Comparison of the antenna frequencies on GPR images	40
2.7	Conclusions	46
	Acknowledgement	47
	References.....	47
3	LOCATING AND CHARACTERIZING BURIAL USING 3D GROUND- PENETRATING RADAR (GPR) AND TERRESTRIAL LASER SCANNING (TLS) AT THE HISTORIC MUESCHKE CEMETERY, HOUSTON, TEXAS.....	52
	Abstract.....	52
3.1	Introduction	53
3.2	Mueschke Cemetery	56
3.3	Geological description.....	58
3.4	Terrestrial laser scanning (TLS) survey	60
3.5	Soil physical properties	64
3.6	GPR numerical modeling	69
3.7	2D GPR templates	71
3.8	Velocity estimation.....	77
3.9	3D-GPR templates surveys	80
3.10	Survey results.....	86
3.11	Conclusions.....	97
	References.....	99
4	3D GROUND-PENETRATING RADAR (GPR) CHARACTERIZATION OF SANDY MOUTH-BARS IN AN OUTCROP RESERVOIR ANALOGS: CRETACEOUS FERRON SANDSTONE, SOUTHEASTERN UTAH, USA.	104
	Abstract.....	104
4.1	Introduction	105
4.2	Geological setting and stratigraphy	108
4.3	Study area.....	115
4.4	GPR data acquisition	116

4.5	Data processing and analysis.....	120
4.6	2D-GPR interpretation	123
4.6.1	Observation	124
4.6.2	Interpretation.....	126
4.6.3	Observation	127
4.6.4	Interpretation.....	129
4.6.5	Observation	130
4.6.6	Interpretation.....	131
4.7	3D GPR interpretation.....	131
4.7.1	Observation	131
4.7.2	Interpretation.....	132
4.8	Discussion	136
4.9	Conclusions	138
	Acknowledgements.....	140
	References.....	140
5	3D GPR INVESTIGATION AT BARRINGER (METEOR) CRATER, ARIZONA	
	148	
	Abstract.....	148
5.1	Introduction	149
5.2	Survey location and geological setting.....	150
5.3	Data acquisition.....	153
5.4	Results	155
5.4.1	Survey grid 3.....	155
5.4.2	Survey grid 8.....	159
5.4.3	Survey grid 9.....	161
5.5	Conclusions	170
	Acknowledgements.....	171
	References.....	171
6	SUMMARY.....	173
6.1	Summary of contributions	173
7	APPENDIX	179

A-1	Spherical divergence exponential gain	179
A-2	Investigation into the interference between culverts.....	182
A-3	TLS processing flow chart	185

LIST OF FIGURES

Chapter 1:

- Figure 1.1.** A GPR cross section of 250 MHz data acquired by the beach in Galveston, Texas..... 1
- Figure 1.2.** The number (150) of published GPR studies based on sediments is more focused on Quaternary deposit (Akinpelu, 2010).....7

Chapter 2:

- Figure 2.1.** Photograph of the culverts supporting a road over a bayou at the University of Houston's geophysical test site near Houston, Texas. The diameter, distance between the adjacent culverts, and the depth to the top of the culvert are annotated.....20
- Figure 2.2.** A GPR section (stretched to depth) from the 250 MHz system is overlain on a photograph of the culverts.....21
- Figure 2.3.** Schematic diagram of two adjacent culverts with material dielectric values annotated (b) Simulated GPR at 250 MHz. (c) 250 MHz field data. (d) 250 MHz field data wavelet of the reflected signal. The deflection of the reflected wave at about 17 ns produces a positive signal (white).....23
- Figure 2.4.** A forward and reverse collection method was employed to obtain an orthogonal survey grid.....24
- Figure 2.5.** Average precipitation at La Marque, Texas between 1st of June to 12th of June 2013.26

Figure 2.6. (a) 250 MHz after rain raw data with dewow applied (b) 250 MHz with 48 hours drying data with dewow applied.....	27
Figure 2.7. (a) 250 MHz after rain data with dewow and gain applied. (b) 250 MHz with 48 hours drying data with dewow and gain applied. Both have the same gain parameters applied.....	27
Figure 2.8. (a) Average-Frequency spectrum of 250 MHz after rain data (b) Average-Frequency spectrum of 250 MHz with 48 hours drying data.....	28
Figure 2.9. (a) Average-Time amplitude plot of 250 MHz after rain data (b) Average-Time amplitude plot of 250 MHz with 48 hours drying data.....	28
Figure 2.10. GPR profiles at the La Marque, Texas test site for 100, 250, 400, 900, and 1000 MHz frequency antennas after time-zero correction, dewow, deconvolution, background subtraction, and gain were applied. All profiles run from East to West.....	29
Figure 2.11. Frequency spectrum of 100, 250, 400, 900, and 1000 MHz.....	30
Figure 2.12. (a) GPR gather from the CMP survey with a hyperbola (dashed black curve) fit to the reflector. The hyperbola fit on the reflector arrival results in an average velocity of 0.08 m/ns. (b) Velocity semblance results in the range of 0.07 to 0.10 m/ns.....	31
Figure 2.13. Migrated sections of 250 MHz data using velocities from 0.07 m/ns to 0.08 m/ns. Basic processing includes time-zero correction, dewow, deconvolution, background subtraction, and gain before the migration. Optimal migrated sections are found in Figures 2.13a and 2.13b using velocities of 0.07 m/ns and 0.08 m/ns, respectively with diffractions largely collapsed.....	33

Figure 2.14. Migrated sections of 250 MHz data using velocities from 0.09 m/ns to 0.10 m/ns. Basic processing includes time-zero correction, dewow, deconvolution, background subtraction, and gain before the migration. Migrated sections in Figures 2.14a and 2.14b using velocities of 0.09 m/ns and 0.10 m/ns yield over migration.....	34
Figure 2.15. (a) The migration result of 100 MHz data using the velocity of 0.07 m/ns. (b) The migrated image overlain on the culvert photograph shows the shape of the migrated image indicates the culverts' tops but with a lower image resolution than that of 250 MHz.....	35
Figure 2.16. Migration result of 400 MHz data using the velocity of 0.10 m/ns. The result shows the culverts' top and	36
Figure 2.17. Migration result of 900 MHz data using the velocity of 0.10 m/ns. The top of the culvert is evident; however, there is limited information about the culverts' shape as seen in Figures 2.9 and 2.10.....	37
Figure 2.18. Migration result of 1000 MHz data using the velocity of 0.12 m/ns. The culvert's tops are clear with some coverage of the culvert's curvature.....	37
Figure 2.19. Migration result of 250 using MHz data using the Gabor deconvolution followed by shot-record Gazdag prestack depth migration (PSDM) with a velocity of 0.10 m/ns.....	38
Figure 2.20. Best migration velocity versus antenna frequency shows frequency dependency.....	39

Figure 2.21. The 3D volume of 250 MHz data (with the top at depth 0.71 m) shows the high amplitude regions (A) corresponding to the top of the four buried culverts.....	40
Figure 2.22. Schematic diagram of propagation distance calculation.....	42
Figure 2.23. The plot of the propagation distance as a function of frequency. The comparison with the depth estimate as a function of the frequency reported by Annan (2004) shows a reasonable agreement with the calculated propagation distance.....	43
Figure 2.24. The effect of SNR with the varying frequencies.....	44
Figure 2.25. The plot between GPR depth and total station depth for five antennas. The black line is the equality line to represent a slope of 1.0 between GPR and the total station.....	45

Chapter 3:

Figure 3.1. The survey location in northwest Houston and GPR suitability map and (USDA, 2009). The majority of the study area is classified as having a moderate to high suitability index. The black dash divides the Pleistocene Lissie (NW) and Beaumont Formation.....	57
Figure 3.2. Mueschke Cemetery base map showing GPR surveys (Grids 1, 2, 3, Line A, and CMP, C) and our excavated test burial-pit location, T.....	58
Figure 3.3. The red outline shows the parameter of the excavated pit (1.8 m x 1.2 m x 1.5 m). The yellow dotted lines mark the rebar's interval location. The rebar was used as a velocity calibration. A concrete was buried in the pit to simulate the	

concrete-vaulted burial. The wood in the photo was also buried	59
Figure 3.4. (a) Three major layers were identified based on the soil features: sandy loam (between the surface and at 0.7 m), sandy clay loam (between 0.7 and 1.1 m), and mostly clay (below 1.1 m). (b) Dielectric constant measurement of the four soil samples from Mueschke Cemetery. (c) Moisture content percentage measurement of the four soil samples. (d) Electrical conductivity measurement of the four soil samples. (e) Stacking velocity (Red line) and interval velocity (green line) versus depth.....	60
Figure 3.5. In plan-view: it is hypothesized that the wooden burial is characterized by a depression but the concrete burial is identified by a surface mound.....	61
Figure 3.6. TLS picture taken at three locations (white hexagons) using a survey-grade laser scanner, RIEGL VZ-400 to study the surface elevation profile.....	62
Figure 3.7. The surface elevation from terrestrial laser scanning (TLS) (after Inverse Distance Weighting) with headstones. The image shows the areas with depressions (red), some of which coincide with the known wooden burial locations as shown by blue dashed circles. The image also shows the areas with mounds (green), some of which coincide with the known concrete burial locations as shown by red dashed circles.....	63
Figure 3.8. The surface elevation residual from terrestrial laser scanning (TLS) (after detrending) with headstones. There are some correlations of surface mounds on TLS image with known concrete burials (after 1940) as highlighted by red dashed circles. The image shows the areas with depressions (red), some of which coincide with the known burial locations as shown by blue dashed	

circles.....	64
Figure 3.9. Four soil samples (from depths of 0.35 m, 0.75 m, 1.1 m, and 1.3 m) from Mueschke Cemetery used for the dielectric constant, moisture content, and conductivity experiments.....	65
Figure 3.10. The percentage of the grain size of four soil samples at the indicated depths.	65
Figure 3.11. The dielectric constant of four soil samples (from depths of 0.35 m, 0.75 m, 1.1 m, and 1.3 m) measured at frequencies of 100 and 250 MHz as a function of moisture content.....	67
Figure 3.12. (a) Modeling of one concrete burial (yellow rectangle) and two wooden burials (orange rectangle) in soil. (b) The hyperbola from the concrete burial has a rectangular shape top while wooden burials have a regular hyperbola shape.....	70
Figure 3.13. A photograph showing a University of Houston team member (Mr. Marcus Zinecker, with Lone Star's Ms. Janet Flores) pushing the Noggin Plus SmartCart 250 MHz antenna. The photograph also shows headstones in the Mueschke Cemetery.....	72
Figure 3.14. GPR profile of Line A shows burials between 1989 and 2009 are characterized by planar and strong diffractions similar to the numerical modeling results. Green arrows indicate concrete burials while yellow arrows mark wooden burials.....	74
Figure 3.15. (a) GPR section showing a 2D profile of the concrete and wooden burials in the excavated pit. Yellow and blue dashed rectangles outline the concrete burial and the wooden burial, respectively. Red arrows indicate the transition	

area between the disturbed/fresh soil that was used to bury the concrete and the compacted soil.....	77
Figure 3.16. (a) Hyperbola matching over the diffraction of rebar (R1) buried at a depth of 0.50 m yields 0.067 m/ns. (b) The velocity obtained from the hyperbola matching over the diffraction of rebar (R2) is 0.064 m/ns. The green hyperbolas mark tree roots in the.....	78
Figure 3.17. Velocity semblance from a CMP survey using 100 MHz antenna at the cemetery results in a range of velocity between 0.055 to 0.067 m/ns.....	79
Figure 3.18. Migrated GPR section showing burials of Nelson (RIP: 1979) (A), Ernest (RIP: 1988) (B), and Elsie (RIP: 2007) (C) Ligon marked by the strong reflections.	81
Figure 3.19. GPR depth slice at 0.57 m indicates the top of burial B and C seen by the high amplitude areas in the rectangular box. The high amplitude anomaly in the top right corner is interpreted as clay. (b) GPR depth slice at 0.65 m indicates the top of burial A.....	83
Figure 3.20. GPR depth slice at 0.6 m shows the high amplitude anomaly in the top right corner is interpreted as clay. The corresponding GPR section indicates continuity of the reflector and this verifies the high amplitude anomaly is interpreted as clay layer.....	84
Figure 3.21. GPR depth slice at 0.75 m shows the high amplitude anomaly in the bottom half of the survey grid is interpreted as clay. The corresponding GPR section indicates continuity of the reflector and this verifies the high-amplitude anomaly is interpreted as clay layer.....	84

- Figure 3.22.** (a) GPR depth slice map overlain on the detrended TLS elevation profile to look for the surface mounds or depression of the burials. Two black lines are the investigation section. (b) The graph of L1-L1' shows a mound over the known concrete burial correspond to the burial C in Figure 3.19a. (c) The graph of L2-L2' shows a mound over the known concrete curial correspond to the burial B in Figure 3.18a.....85
- Figure 3.23.** GPR section showing a 2D profile of the Greger survey where we are searching for the unmarked burial of James Culven Poland. A strong GPR reflection is observed between 11 m and 12 m. A fiducial marker F1 was made during the survey to mark the suspected location of the burial.....87
- Figure 3.24.** Depth slice shows the high amplitude area A corresponding to the suspected wooden burial at 0.42 m deep.....87
- Figure 3.25.** (a) GPR depth slice map overlain on the exaggerated TLS elevation profile to look for surface depressions of the unmarked burials. The image shows an area of surface depression, A, which corresponds to the burial A in Figure 3.20 and Figure 3.21 Figure (b) Line B-B' shows the surface depression corresponds to the high amplitude area of A.....88
- Figure 3.26.** A marker was placed at the location based on the result from the geophysical investigation.....89
- Figure 3.27.** A photograph showing the estimated location of James West's burial which 1.5 m south of Eliza West's burial place.....90
- Figure 3.28.** Unmigrated GPR section is showing GPR reflections of known burials, labeled E for Eliza West and F for an unnamed headstone. D is suspected to be

the burial of James West. The location of D matches the location from the archaeological record.....	91
Figure 3.29. Unmigrated GPR section is showing GPR reflections of known burials, labeled E for Eliza West and F for an unnamed headstone. D is suspected to be the burial of James West. The location of D matches the location from the archaeological record.....	92
Figure 3.30. Migrated GPR section is showing GPR reflections of known burials, labeled E for Eliza West and F for an unnamed headstone. D is suspected to be the burial of James West. The location of D matches the location from the archaeological record.....	93
Figure 3.31. Photograph showing the location of nearby trees that are in the GPR survey line.....	94
Figure 3.32. GPR depth slice at 0.85 m indicates the top of the suspected burial of James West (D). E and F belong to burials of Eliza West and the unnamed headstone. The anomaly located at D is harder to identify on the depth slice because of the presence of the high amplitude anomaly. The high amplitude anomaly is suspected to be a tree root system from nearby trees. D is the corresponding location on the TLS elevation map with a surface depression.....	95
Figure 3.33. GPR depth map overlain on the exaggerated TLS elevation profile shows areas of surface depression D and E corresponding to the burials D and E in Figure 4.23. Area D shows the suspected burial of James West lies on a slope.	96

Chapter 4:

- Figure 4.1.** Oblique depositional strike sequence stratigraphic framework of the Notom delta by Li et al., (2010) shows the distributary mouth bar located in parasequence 6 of sequence 2 which is the focus of this study (marked by a red rectangle).....110
- Figure 4.2.** A. photograph of vertical section of the river-dominated Parasequence 6 (Li and Bhattacharya, 2013).....111
- Figure 4.3.** The distributary mouth bar (red box) model depicted by Li (2013).....112
- Figure 4.4.** (A) Photograph of the cross section of unit bars. (B) A plan-view exposure of large-scale foresets (classic rib-and-furrow pattern) interpreted as unit mouth bars (Li et al., 2014). The width range of the individual rib is up to a few tens of meters and the flow direction is perpendicular to the rib-elongation direction (Ahmed et al, 2014).....114
- Figure 4.5.** Base map A shows the regional area of stud and red box in the base map B shows the location of the study area located in the Coalmine Wash area (modified from Ullah et al., 2015)..... 116
- Figure 4.6.** (A) Photograph of the survey area with the arrow pointing to the GPR survey location. The elevation of the study area is 1509 m. (B) The Google Earth image of the GPR survey location with the GPR grid. The Google Earth view is pointing toward the south.....118
- Figure 4.7.**A photograph of the 3D GPR survey acquisition using Sensors and Software's Noggin Plus SmartCart 250 MHz antenna. A rectangular 3D GPR survey of 25 m (inline) by 15 m (crossline) was undertaken on the top of the outcrop.

Virtual black dash lines were drawn on the photograph to show the inline and crossline survey lines (Not to scale).....	120
Figure 4.8. Detailed GPR data processing flow diagram.....	121
Figure 4.9. Velocity estimation using hyperbola matching method overlaid over a distinct hyperbola yields 0.131 m/ns.....	122
Figure 4.10. GPR image shows the upper dune-scale cross beds interpreted to be deposited in a friction-dominated environment. These are estimated to be deposited subaqueously, in a water depth no more than a few meters.....	126
Figure 4.11. GPR image shows the underlying units are the botomset facies. The bar is estimated deposited subaqueously, in water depth no more than a few meters.....	127
Figure 4.12. The dip is interpreted to be in the general downstream direction with a dip angle of 20°	128
Figure 4.13. GPR image shows the progradational unit mouth bar with a dip angle of 20° deposited by friction-dominated river flow. The laterally continuous basal planar bed at the bottom of the figure is interpreted to be deposited in an inertia-dominated river mouth during a flood event.....	129
Figure 4.14. GPR image shows the progradational unit mouth bar with a dip angle of 20 degrees deposited by friction-dominated river flow. The laterally continuous basal-planar bed at the bottom of the figure is interpreted to be deposited in an inertia-dominated.....	130
Figure 4.15. GPR image in strike-direction. It displays a terminal distributary channel deposit with a depth of 1.5 m.....	131

Figure 4.16. GPR image in strike-direction. It displays a terminal distributary channel deposit with a depth of 1.25 m.....	133
Figure 4.17. 3D-GPR volume showing the strike direction cuts the 3D volume and reveals the details of the channel shape and base displays a terminal distributary channel deposit with a depth of 1.25 m.....	134
Figure 4.18. Fence diagram of the 3D GPR volume showing the continuity of the bottom of the channel in the strike direction and the erosional boundary.....	135
Figure 4.19. Amplitude depth slice at 0.4 m of the 3D-GPR data. The radius of curvature of the ribs are observed with an interpreted width of 9 m.....	136
Figure 4.20. Schematic diagram of a depositional model showing 3D reconstruction of the distributary mouth bars and terminal distributary channels derived from GPR vertical and amplitude depth section.....	138

Chapter 5:

Figure 5.1. Google Earth photograph shows the Meteor Crater image. The location of the survey is marked by the red rectangular grid.....	151
Figure 5.2. An example of the Canyon Diablo (Meteor Crater) meteorite (Photo: Robert R. Stewart).....	151
Figure 5.3. The geologic map of the distribution of materials at the Meteor Crater. Red rectangular grid marks the GPR survey area (Russell, 2013).....	152
Figure 5.4. The geologic cross section of Meteor Crater (Pilon and Grieve, 1991).....	153
Figure 5.5. A photograph shows the survey area with the Noggin Smart Cart 250 MHz in sight.....	154

Figure 5.6. GPR survey grids at the Meteor Crater.....	154
Figure 5.7. Hyperbola matching to extract radar velocity yields 0.102 m/ns.....	155
Figure 5.8. Unmigrated GPR profile (Line Y6).....	157
Figure 5.9. Depth slice of grid 3 at 2 m shows a high amplitude area approximately at 72.5 m.....	157
Figure 5.10. Migrated GPR profile with a velocity of 0.10 m/ns (Line Y6).....	158
Figure 5.11. Migrated GPR profile with a velocity of 0.11 m/ns (Line Y6).....	158
Figure 5.12. Migrated GPR profile with a velocity of 0.12 m/ns (Line Y6).....	159
Figure 5.13. Migrated GPR profile with a velocity of 0.13 m/ns (Line Y6).....	159
Figure 5.14. Unmigrated GPR profile shows various anomalies characterized by high amplitude reflectors at various locations marked by yellow dashed circles (Line X6).....	160
Figure 5.15. Migrated GPR profile with a velocity of 0.10 m/ns (Line X6) shows various anomalies characterized by high amplitude reflectors at various locations marked by yellow dashed circles (Line X6).....	160
Figure 5.16. Unmigrated GPR profile (Line X4).....	161
Figure 5.17. Migrated GPR profile with a velocity of 0.10 m/ns (Line X4).....	162
Figure 5.18. Depth slice at the interval of 2.38 m and 2.39 m shows the high-amplitude area interpreted as ejecta elements observed in the GPR profile.....	162
Figure 5.19. Depth slice at the interval of 2.38 m and 2.39 m shows the high amplitude area interpreted as ejecta elements observed in the GPR profile.....	163
Figure 5.20. Depth slice at the interval of 0.92 m and 0.93 m shows various locations of high amplitude areas interpreted as ejecta elements observed in the GPR	

profile.....	164
Figure 5.21. Depth slice at the interval of 0.92 m and 0.93 m shows various locations of high amplitude areas interpreted as ejecta elements observed in the GPR profile.....	164
Figure 5.22. Depth slice at the interval of 0.84 m and 0.85 m shows various locations of high amplitude areas interpreted as ejecta elements observed in the GPR profile.....	165
Figure 5.23. The alluvium thickness change from Southeast to Northwest at the survey grid 8.....	166
Figure 5.24. The alluvium thickness contour plot of the survey grid 8.....	166
Figure 5.25. The alluvium thickness change from Southeast to Northwest at the survey grid.....	167
Figure 5.26. The alluvium thickness contour plot in survey grid 9.....	168
Figure 5.27. The alluvium thickness change from Southwest to Northeast at the survey grid.....	169

Appendix:

Figure 7.1. 250 MHz data with varying Spherical Divergence Exponential Gain applied.....	181
Figure 7.2. The interference between the culverts produces an artifact that appears as a third hyperbola in between the adjacent hyperbolas.....	182
Figure 7.3. The photograph of the culverts with dimension of the buried culverts.....	183
Figure 7.4. The simulated wave propagation based on equations (1), (2) and (3). It can	

be observed and an interference was produced due to the multipathing of traveling wave between the two culverts.....184

Figure 7.5. TLS processing flow.....186

LIST OF TABLES

Chapter 2

Table 2.1. Survey parameters for the five antenna systems.....25

Table 2.2. Comparison of five antenna frequencies on the migrated GPR images.....46

Chapter 3

Table 3.1 Summary of the GPR survey at the Mueschke Cemetery.....71

Chapter 4

Table 4.1. GPR survey parameters to acquire 3D data to image a single set of forward-accreting mouth-bar deposits.....119

Table 4.2. Facies description and the associated architectural elements.....137

LIST OF ABBREVIATIONS

<i>GPR</i>	Ground-penetrating radar
<i>NASA</i>	National Aeronautics and Space Administration
<i>2D</i>	Two dimensions
<i>3D</i>	Three dimensions
<i>GSSI</i>	Geophysical Survey Systems Inc.
<i>AGU</i>	American Geophysical Union
<i>SAGEEP</i>	Symposium on the Application of Geophysics to Engineering and Environmental Problems
<i>SEG</i>	Society of Explorations Geophysicists
<i>CMP</i>	Common Mid-Point
<i>WARR</i>	Wide Angle Reflection and Refraction
<i>STFT</i>	Short Time Fourier Transform
<i>EM</i>	Electromagnetics
<i>RC</i>	Reflection coefficient
<i>PSDM</i>	Prestack depth migration
<i>TLS</i>	Terrestrial Laser Scanning
<i>USDA</i>	U.S. Department of Agriculture
<i>USGS</i>	U.S. Geological Surey
<i>FDTD</i>	Finite-difference time domain
<i>RIP</i>	Rest in peace
<i>TCF</i>	Trillion Cubic Feet

NW Northwest

SE Southeast

LIST OF SYMBOLS

σ	Electrical conductivity
μ	Magnetic permeability
μ_r	Relative magnetic permeability
μ_o	Permittivity in free space
ε	Dielectric permittivity
ε_r	relative permittivity or dielectric constant
ε_o	Dielectric permittivity in free space
λ	Wavelength
ρ	Resistivity
δ	Skin depth
ν	Radar velocity
ω	Angular frequency
f	Frequency
D	Depth

1 INTRODUCTION

1.1 Background

Ground-penetrating radar (GPR) enables imaging near the surface (often within several meters of the surface) for applications such as geotechnical engineering, archaeology, sedimentology, and planetary studies. Apart from the high-resolution mapping benefits, analysis of GPR data allows for investigations of subsurface physical properties such as the dielectric permittivity (or dielectric constant), velocity, electrical conductivity, and moisture content. GPR is a fast, high-resolution, and non-invasive geophysical technique operating between 10 MHz and 2.5 GHz. Figure 1.1 shows an example of GPR data acquired by the 250 MHz Sensors & Software Noggin SmartCart system in Galveston, Texas.

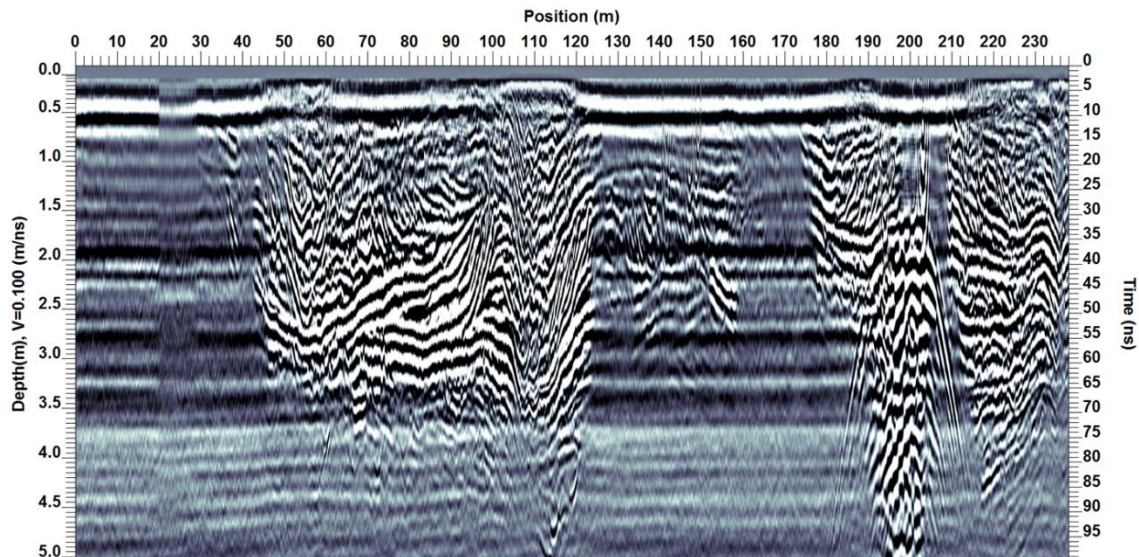


Figure 1.1. A GPR cross section of 250 MHz data acquired by the beach in Galveston, Texas.

Historically, GPR was first used in Austria in 1929 to measure glacier thickness (Stern, 1929). In the late 1950s, one of the US Air Force aircrafts crashed during landing in Greenland because their radar pulses were penetrating the glacial ice (Clarke, 1987). This incident led to numerous investigations of GPR applicability in detecting subsurface targets and layers. In 1967, the National Aeronautics and Space Administration (NASA) built the first GPR prototype to investigate the surface of the moon (Simmons et al., 1972). Since its commercial introduction in the early 1970s, GPR has been applied in planetary analogs (Stewart, 2003; Khan et al., 2007), geotechnical engineering (e.g., Al-Qady and Lahouar, 2005, Patriarca et al., 2011, Tosti, et al., 2016,), geotechnical engineering (e.g., Fruhwirth and Mueller, 1994), fracture mapping (e.g., Grandjean and Gourry, 1996; Tsoflias, 2004), archaeological works (e.g., King et al., 1993; Stanberg and McGill, 1995; Ruffell et al., 2009; Fiedler et al., 2009), and shallow hydrocarbon reservoir analog studies (e.g., Dominic, et. al., 1995; Corbeanu et al., 2001; Neal, 2004; Mukherjee et al., 2006; Lee et al., 2007; Li and Bhattacharya; 2013).

1.2 Research gaps and significance

GPR surveys will cost \$2,500 to \$5,000 per day, so it is important to design an effective GPR survey from the beginning to avoid unexpected failure and expensive multiple acquisition campaigns. While there are a variety of commercial GPR systems, users are constrained by the budget, equipment portability, equipment availability at hand, access to the survey site, weather, and condition of the survey location. One of the key steps in

designing GPR surveys is to select the optimum antenna frequency, an important parameter controlling the depth of penetration and the image resolution. In turn, the depth of penetration and the image resolution defines GPR operating performance (Davis and Annan, 1989). These performance aspects are strongly affected by the soil's electromagnetic properties. Lower frequencies penetrate deeper in the subsurface but with lower image resolution. Conversely, higher frequencies have a higher resolving power but the signal will be considerably attenuated, resulting in a shallower depth of penetration. Hence, the inverse dependency on frequency complicates the selection of GPR frequency. While various publications and tips report on how to select the best antenna for GPR surveys, (e.g., Annan and Cosway 1990), researchers have not yet fully explored the impact of varying frequencies on GPR resultant images under key criteria such as target detectability, shape, image clarity, propagation distance, and depth accuracy to determine the optimal frequency for imaging shallow buried targets. To address this gap, Chapter 2 details a study aimed to determine the antenna frequency which would best image four buried culverts and observe key parameters in the analysis. The study extends the existing GPR performance criteria to better predict survey success.

In detecting burials, GPR success is linked to the soil's electromagnetic properties (such as the dielectric constant and conductivity) and clay content. These parameters are often unknown, highly variable over a small distance, and site-specific. A GPR soil suitability map provides an indication of the relative suitability of soils to GPR within broadly defined soil and physiographic areas. However, the actual GPR performance depends on the local soil properties and the target characteristic within any broadly defined area. Therefore,

soil studies are necessary to verify the suitability of the on-site location because of the inhomogeneity of soil delineations (USDA, 2009). Also, it is a challenge to identify a small area on the compact map. Locating the survey location on the suitability map is an estimate and may not be accurate and reliable. In order to circumvent the limitations of these maps, this study used a lab experiment to analyze the soil grain size and determine the clay content, which in turn provided evidence for GPR suitability in the area. A burial pit was also excavated to provide a close-up on the soil stratigraphy. Present studies to locate unmarked burials usually estimate dielectric constant from the literature and assume it to be similar to the area of study. This research used soil lab experiments including the dielectric constant, conductivity, and soil moisture measurements. Dielectric constant and conductivity were used in the numerical modeling to simulate the various types of burials. Grain-size experiments indicated that the soil at the survey location is reasonable for GPR.

Because the success of GPR often depends on selecting an appropriate area, it is very desirable to determine an area's viability before spending money and time with GPR surveys. Although many studies demonstrate GPR suitability in detecting burials, none mentioned integrating Lidar data as a reconnaissance technique before getting into a detailed study with GPR. Chapter 3 details the soil studies used to determine the suitability of GPR in the area. The study also demonstrates the integration of Lidar with GPR data in finding geophysical evidence of unmarked burials. While GPR has gained popularity in detecting unmarked burials, some published studies reported the use of remote sensing methods including airborne thermal imaging (Dickinson, 1976) and satellite imagery and aerial photography (Brillis et al., 2000) to detect unmarked burials.

Ruffell et al. (2009) used aerial imagery and geophysical surveying to locate 150-year-old unmarked burials. There were no studies, to our knowledge, that have used GPR and Lidar to locate and characterize burials. Many integrations of geophysical techniques were used simultaneously such as GPR and resistivity surveys to identify unmarked burials. While additional geophysical data assisted GPR to reduce uncertainties of unmarked burial locations, this methodology assumed that GPR worked in the first place. This study suggests the use of Lidar as a reconnaissance tool to detect surface depressions or mounds is useful.

In chapter 4, the study investigates GPR potential to resolve the 3D internal architecture, geometry, and dimension of friction-dominated, radial distributary mouth bars at the Ferron sandstone. Reservoir analogs or reservoir environments that outcrop the Earth has been studied to assist in reconstructing accurate 3D models of the internal structures of hydrocarbon reservoirs. Such 3D models are important elements in the fluid flow simulation used during the petroleum production stage (Tomutsa et al., 1991; Tyler et al., 1992; Fisher et al., 1993a, b). Outcrop analog studies have periodically been used to understand the complex sedimentology and stratigraphy of subsurface reservoir architecture for accurate well placement and enhanced oil recovery (EOR) planning during field development.

For reservoir analog studies, surface seismic data is excellent in sampling the whole reservoir geometry, but it is often lacking enough resolution to visualize the geobody (Howell et al., 2014). Well data are sparse and we tend to interpolate data between available wells, and this is a rather inaccurate representation of the lateral variation of the reservoir

architecture. GPR provides a solution by acquiring high-resolution images of shallow subsurface reservoirs with wavelengths in the range of centimeters (Asprion and Aigner, 1997). In addition, GPR is efficient in mapping lithofacies because it offers real-time output and requires minimal processing (Bridge, 2003).

With 3D GPR data, the horizontal and vertical accuracy of resultant images are improved (Szerbiak, et al., 2001). Very few studies on outcrop imaging using 3D GPR were documented due to the extensive survey time, logistics, limited access to the survey area, and equipment portability. Howell et al., 2014 reported that the number of datasets in the fluvial depositional system is still minimal. While available studies have demonstrated GPR capability in the fluvial sedimentology, most available studies are focused towards the recent, unconsolidated, and quaternary fluvial deposits (Corbeanu et al., 2001). Akinpelu (2010) reported an analysis on 150 published GPR studies and showed that 89% of the studies are biased towards the quaternary deposits as shown in Figure 1.2. There is little information in the GPR study to understand the ancient river deposits. Well-documented facies architectural studies of ancient deltas are also minimally reported (Gani and Bhattacharya, 2007).

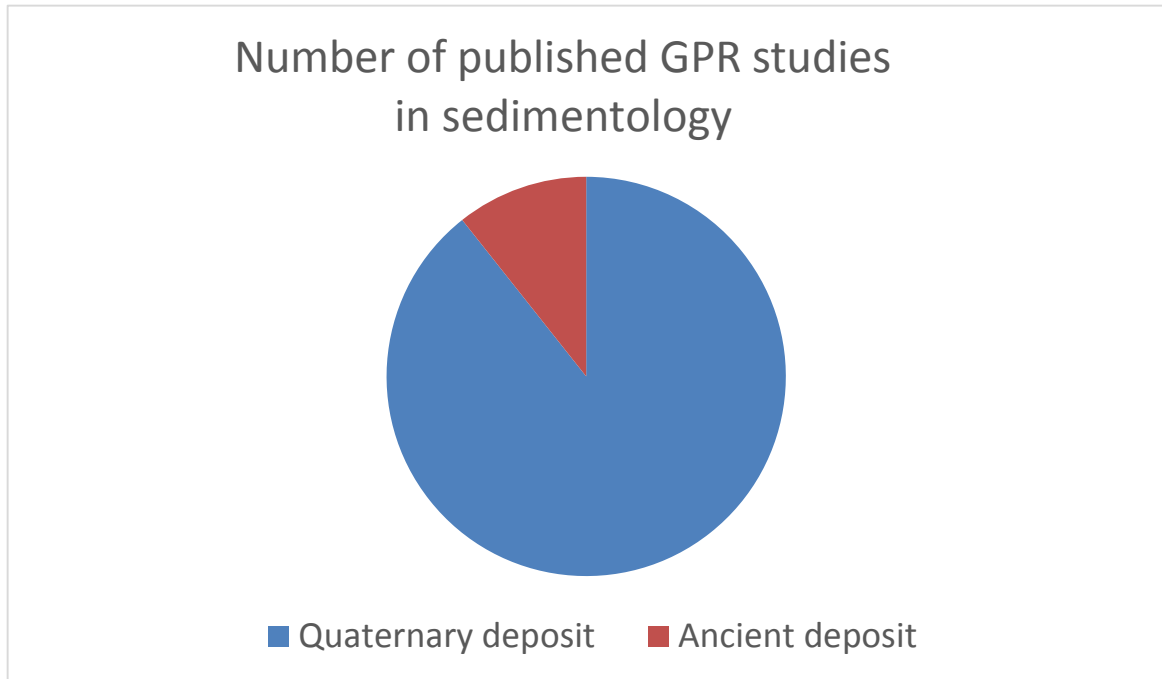


Figure 1.2. The number (150) of published GPR studies based on sediments is more focused on Quaternary deposit (Akinpelu, 2010).

On Earth, 3D GPR can provide insight into the physical properties of the nature of geological layering, topography, and the three dimensional image of craters. This can be used to analyze data from extraterrestrial bodies by remote sensing from the Earth and then by performing a GPR survey on remote bodies. GPR has been used in various studies to understand the subsurface in the planetary analogs environment. GPR is able to reveal the near-surface geological characteristics as has been demonstrated by scientific studies (e.g., Grant and Schultz, 1994; Khan et al., 2007; Russell et al., 2013). Chapter 5 examines the GPR applicability to studying near-surface layering and the distribution and dimension of ejecta elements in the Barringer (Meteor) Crater in Arizona. Alluvium thickness can give insight into the sedimentation of the layer that overlies the ejecta elements and can reveal the shape of the post-impact surface. This study also contributes to the study of 3D GPR

acquisition and imaging at a meteor's craters.

1.3 Research aims and objectives

The main objective of this thesis is to evaluate 3D GPR capability in four different critical applications: geotechnical, archaeological, hydrocarbon reservoir analog, and impact craters.

The specific objectives centered on the 3D geophysical acquisition, soil studies, data processing flow, novel methodologies applied to the research scope, and the interpretation of the images. The specific objectives are:

- To study the soil dielectric constant of the soil at La Marque, Texas using an experimental setup.
- To obtain corresponding radar velocities and to study the effect of the frequency-dependent dispersion.
- To determine the radar velocity to best image shallow buried anomalies.
- To observe and evaluate the effect of varying frequencies on the target detectability, image clarity, shape, propagation distance, and depth accuracy.
- To apply a remote sensing technique as a reconnaissance tool before GPR surveys.
- To investigate GPR suitability at the Mueschke Cemetery in the generally clay-rich Houston area.
- To characterize a variety of burials (types, sizes, and depths).
- To find previously unknown burials including the oldest known burial.

- To investigate GPR's potential to resolve 3D internal architecture, geometry, and dimension of friction-dominated, radial-distributary mouth bars.
- To identify radar facies and relate them to architectural and sedimentological stratigraphic interpretation.
- To interpret these various proximal delta front mouth bar facies from the GPR images and then compare our interpretation with the finding by Li (2014) in 2D-vertical sections.
- To extract geophysical information, such as the radar velocity, depth of penetration, vertical resolution, and porosity.
- To estimate the alluvium thickness and to directly characterize and observe the distribution of the ejecta elements of a well-known meteorite impact crater at Barringer (Meteor) Crater, Arizona.

In this study, field works employing a range of GPR antenna frequencies by Sensors & Software (100, 250, and 1000 MHz) and GSSI (400 and 900 MHz) was employed at La Marque, Texas to collect the data from summer 2013 to summer 2015. GPR software by Sensors & Software and Radan 7 by Geophysical Survey Systems Inc. (GSSI) were used to process the data. GPR and Lidar field works were conducted at Mueschke Cemetery in Houston, Texas. GPR field works at the Ferron sandstone, Utah and Barringer (Meteor) Crater were performed using 250 MHz Sensors & Software's system. I use a Matlab-based computer program, MatGPR to perform the GPR numerical modeling. The study period encompassed a wide range of geological settings and soil conditions that yielded

various GPR responses. The results and interpretation of the soil studies and GPR provided valuable information about four survey locations and different applications.

1.4 Thesis structure

This thesis is organized into six chapters, including four main chapters that were written as independent research papers. In each chapter, background information on the investigation is included. Chapter 1 details the introduction of the thesis including the discussion on research gaps, project objectives, thesis structure, and research contributions. Chapter 2 shows the imaging of buried culverts using 3D GPR with varying antenna frequencies (100 MHz-1GHz). Chapter 3 details the study of using GPR, terrestrial laser scanning (TLS), cemetery records, and oral histories to locate and characterize unmarked burials at the Mueschke Cemetery in Houston, Texas. Chapter 4 investigates the use of 3D GPR surveys to visualize architectural elements of friction-dominated distributary mouth bars in proximal delta-front deposits in the Cretaceous Ferron Sandstone at the top of the Notom Delta in southeastern Utah, U.S.A. Chapter 5 summarizes GPR investigations to estimate the alluvium thickness and to directly characterize the ejecta elements of a well-known planetary analog at Barringer Meteor Crater, Arizona. Finally, Chapter 6 details the main contributions of this dissertation and recommendations for future studies. Appendix A details the computer code, additional data processing, and other information that support the main chapters of the thesis.

1.5 Research contributions

A few chapters of this thesis have been submitted to peer-reviewed journals and published in peer-reviewed conferences. Each contribution is listed below.

1. **Aziz, A. S.,** R. R. Stewart, S. L. Green, J. B. Flores, 2016, Locating and characterizing burials using 3D ground-penetrating radar (GPR) and terrestrial laser scanning (TLS) at the historic Mueschke Cemetery, Houston, Texas: Journal of Archaeological Science: Reports (In review).
2. **Aziz, A. S.,** R. R. Stewart, M. S. Ullah, and J. P. Bhattacharya, 2015, Imaging architectural elements of distributary mouth bars using 3D GPR: examples from Cretaceous Ferron Sandstone, Notom Delta, South-East Utah, 28th Annual Symposium on the Application of Geophysics to Engineering and Environmental Problems, SAGEEP, Expanded Abstract.
3. **Aziz, A. S.,** R. R. Stewart, M. S. Ullah, and J. P. Bhattacharya, 2015, 3D GPR characterization of sandy mouth bars in an outcrop reservoir analog: Cretaceous Ferron Sandstone, south-east Utah, Annual Meeting, SEG, Expanded abstracts. (Awarded as the top 31 best presented technical paper by the SEG Technical Committee).
4. **Aziz, A. S.,** R. R. Stewart, S. L. Green, J. B. Flores, 2014, 3D GPR Modeling and Imaging of Burials: Mueschke Historic Cemetery, Houston, Texas: American Geophysical Union (AGU) Fall Meeting, Expanded abstract.
5. **Aziz, A. S.,** R. R. Stewart, S. L. Green, J. B. Flores, 2014, 3D GPR Modeling and Imaging of Burials: Mueschke Historic Cemetery, Houston, Texas, 29th Annual

Symposium on the Application of Geophysics to Engineering and Environmental Problems, SAGEEP, Expanded Abstract.

6. **Aziz, A. S.**, R. R. Stewart, S. L. Green, 2013, Imaging Buried Culverts Using Ground Penetrating Radar: Comparing 100 MHz through 1 GHz Antennae: American Geophysical Union (AGU) Fall Meeting, Expanded abstract.

References

Akinpelu, O, 2010, Ground Penetrating Radar Imaging of Ancient Clastic Deposits: A Tool for three-dimensional Outcrop Studies: Ph.D. Thesis, University of Toronto.

Al-Qadi, I. L. and S. Lahouar, 2005, Measuring layer thickness with GPR – Theory to practice: Construction and Building Materials, 19, 763-772.

Annan, A.P., and S. W. Cosway, 1994, GPR frequency selection, 5th International Conference on GPR, Extended Abstract.

Bridge, J.S., 2003, Rivers and Floodplains, Blackwells, Oxford, 491 p.

Asprion, U., and T. Aigner, 1997, Aquifer architecture analysis using ground-penetrating radar: Triassic and quaternary examples: Environmental Geology, 31, 66–75.

Clarke, G. K. C., 1987, A short history of scientific investigations on glaciers: Journal of Glaciology, Special Issue, 4-24.

Corbeanu, R. M., K. Soegaard, R. B. Szerbiak, J. B. Thurmond, G. A. McMechan, D. Wang, S. H. Snelgrove, C. B. Forster, and A. Menitove, 2001, Detailed internal

architecture of fluvial channel sandstone determined from outcrop and 3-D ground penetrating radar: Example from mid Cretaceous Ferron Sandstone, east-central Utah: AAPG Bulletin, 85, 1583–1608.

Dominic, D.F., Egan, K., Carney, C., Wolfe, P.J. and Boardman, M.R., 1995. Delineation of shallow stratigraphy using ground penetrating radar: Journal of Applied Geophysics, 33, 167-175.

Fruhworth, R., and R. Mueller, 1994, Application of ground penetrating radar to geotechnical problems : 56th Meeting and Technical Exhibition, European Association of Exploration Geophysicists, Technical Programme and Abstracts of Papers, 56, 1012-1013.

Fiedler, S., B. Illich, J. Berger, and M. Graw, 2009, The effectiveness of ground penetrating radar surveys in the location of unmarked burial sites in modern cemeteries: Journal of Applied Geophysics, 68, 380-385.

Fisher, R. S., M. D. Barton, and N. Tyler, 1993a, Quantifying reservoir heterogeneity through outcrop characterization: 1. Architecture, lithology, and permeability distribution of a landward-stepping, fluvial-deltaic sequence, Ferron Sandstone (Cretaceous), central Utah: Gas Research Institute Topical Report GRI-93-0022.

Fisher, R. S., M. D. Barton, and N. Tyler, 1993b, Quantifying reservoir heterogeneity through outcrop characterization: 2. Architecture, lithology, and permeability distribution of a landward-stepping, fluvial-deltaic sequence, Ferron Sandstone (Cretaceous), central Utah: Gas Research Institute Topical Report GRI-93-0023.

Grandjean, G. and Gourry, J.C., 1996. GPR data processing for 3D fracture mapping in a marble quarry (Thassos, Greece): Journal of Applied Geophysics, 36, 19-30.

- Howell, J. A., A.W. Martinius, and T. R. Good, 2014, The application of outcrop analogues in geological modeling: A Review, present status and future outlook, *in* A. W. Martinius, J. A. Howell, and T. R. Good, eds., Sediment body geometry and heterogeneity: Analogue studies for modeling the subsurface: The Geological Society, 387, 1-25.
- King, J.A., 1993, B. W. Bevan, and R. J. Hurry, Reliability of Geophysical Surveys at Historic-Period Cemeteries: An Example from the Plains Cemetery, Mechanicsville, Maryland: Historical Archaeology, 27(3), 4-16.
- Khan, S. D., E. Heggy, J. Fernandez, 2007, Case History: Mapping exposed and buried lava flows using synthetic aperture and ground-penetrating radar in Craters of the Moon lava field, Geophysics: 72, B161-B174.
- Lee, K., M. Tomasso, W. A. Ambrose, and R. Bouroullec, 2007, Integration of GPR with stratigraphic and lidar data to investigate behind-the-outcrop 3D geometry of a tidal channel reservoir analog, upper Ferron Sandstone, Utah: The Leading Edge, 26, 994–998.
- Li. Y., and J. P. Bhattacharya, 2013, Facies Architectural Study of a Stepped, Forced Regressive Compound Incised Valley System in the Ferron Notom Delta, Southern Utah: Journal of Sedimentary Research, 83, 206-225.
- Mukherjee, D., Khan, S.D., and Sullivan, C.E., 2006. Integration of GPR, GPS, Remote Sensing and Geochemistry for Shallow Reservoir Studies in Central and South-Central Texas, Call for Abstracts, AAPG Annual Convention, Houston, TX.
- Neal, A., 2004, Ground-penetrating radar and its use in sedimentology: principles, problems and progress: Earth Science.

- Patriarca, C., S. Lambot, M. R. Mahmoudzadeh, J. Minet, and E. Slob, 2011, Reconstruction of sub-wavelength fractures and physical properties of masonry media using full-waveform inversion of proximal penetrating radar: *Journal of Applied Geophysics*, 74, 26-37.
- Ruffell, A., McCabe, A., Donnelly, C., Sloan, B., 2009, Location and assessment of an historic (150-160 years old) mass grave using geographic and ground penetrating radar investigation, NW Ireland: *Journal of Forensic Science*, 54(2), 382-94.
- Simmons, G., D. W. Strangway, L. Bannister, R. Baker, D. Cubley, G. La Torraca, and R. Watts, 1972, The Surface Electrical Properties Experiment: Lunar Geophysics Conference, Lunar Science Institute, Proceedings.
- Stern, W., 1929, Versuch einer elektrodynamischen Dickenmessung von Gletschereis: *Ger. Beitr. zur Geophysik*, 23, 292-333.
- Sternberg, B. K., and J. W. McGill, 1995, Archaeology Studies in Southern Arizona Using Ground-Penetrating Radar: *Journal of Applied Geophysics*, 33, 209-225.
- Stewart, R.R., 2003, Mars in Canada: The NASA Haughton-Mars Project: Devon Island, Nunavut: *CSEG Recorder*, 5, 5-9.
- Tomutsa, L., M. M. Chang, and S. Jackson, 1991, Application of outcrop data for characterizing reservoirs and deriving grid-block scale values for numerical simulation: Third International Reservoir Characterization Technical Conference, 3RC-08, 1-18.
- Tosti, F., A. Benedetto, L.B. Ciampoli, S. Lambot, C. Patriarca, and E. C. Slob, 2016, GPR analysis of clayey soil behavior in unsaturated conditions for pavement engineering and geoscience applications: *Near Surface Geophysics*, 14, 23-37.

Tsoflias, G.P., Van Gestel J., Stoffa P.L., Blankenship D.D. and Sen M.K., 2004. Vertical fracture detection by exploiting the polarization properties of ground-penetrating radar signals: *Geophysics*, 69, 803-810.

Tyler, N., M.D. Barton, D. G., Bebout, R.S. Fisher, J. D. Grigsby, E., Guevara, M., Holtz, C., Kerans, C., H. S. Nance, R. A., Levey, 1992, Characterization of oil and gas reservoir heterogeneity: U.S. Department of Energy Report 14403-3.

USDA, 2009, Ground Penetrating Radar Suitability Map, 1:600,000: Retrieved from http://www.nrcs.usda.gov/Internet/FSE_DOCUMENTS/nrcs142p2_052162.pdf.

2 IMAGING BURIED CULVERTS USING 3D GROUND-PENETRATING RADAR (GPR) WITH VARYING ANTENNA FREQUENCIES (100 MHZ -1 GHZ)

Abstract

Ground-penetrating radar (GPR) is a useful imaging tool for subsurface investigations. The frequency of the GPR system's antenna is a critical aspect of survey design and success to characterize buried targets. This study aims to determine the antenna frequency which best images four buried culverts, as evaluated by the following criteria: target detectability, shape, image clarity, propagation distance, and depth error. This 3D GPR study uses five different systems with antenna frequencies of 100, 250, 400, 900, and 1000 MHz. The work was undertaken to examine buried culverts. The four buried culverts, at the University of Houston's La Marque Geophysical Observatory near Houston, Texas which support a road crossing one of the area's bayous. Laboratory measurements of the dielectric constant of an unconsolidated soil sample from the site give a dielectric constant of 5.2 and a velocity of 0.13 m/ns. Common mid-point (CMP) measurements using 100 MHz give a range of velocity between 0.07 and 0.10 m/ns. The average velocity estimate of the 250 MHz data using the culvert top known depth and the picked time at the zero-offset yields 0.08 m/ns. Various radar velocities (0.07-0.13 m/ns) were estimated in the subsequent migrations. We found that the best velocity used for the migration indicates some frequency dependency.

2.1 Introduction

Ground-penetrating radar (GPR), usually operating between 10 MHz and 1000 MHz, has been applied in numerous geotechnical fields (Annan et al., 1990; Tong, 1993; Czarnowski et al., 1994; Graf, 1994; Stockbauer and Kalinec, 1995; Powers and Ohoeft, 1996; Zheng and McMechan, 1997; Orlando, 2007; Hugenschmidt et al., 2010). The antenna frequency of the GPR is directly linked to the exploration penetration depth and the image resolution of the method. As a common practice, low-frequency antennas are often selected for deep probing. Singh and Francke (2015) successfully demonstrate the use of a 40 MHz antenna to image mine galleries in East Basuria and Tetulmari Collieries up to 40 m in depth. GPR may penetrate up to 150 m depth by performing signal processing including vertical stacks of up to 32,000 (Francke, 2014). Although lower frequency antennas can penetrate deeper, their wavelengths are longer resulting in a lower resolution images.

While GPR is routinely used to detect man-made, buried targets, there have been fewer studies published that investigate the impact of varying antenna frequencies on the data. Also, there is a gap in the literature that focuses on optimal antenna selection for shallow imaging. Smith and Jol (1995) tested four antennas to predict the maximum probable depths of penetration which were: 57 m (25 MHz), 47 m (50 MHz), 37 m (100 MHz), and 28 m (200 MHz).

Benedetto et al. (2015) highlight the importance of the effect of the antenna frequency on the estimated structures spatial scales. In this study, we use synthetic and field data to examine the effect of varying frequencies on performance criteria such as target detectability, image clarity, shape, propagation distance, and depth accuracy.

Selecting the optimum parameters such as the antenna frequency before GPR surveys is critical. Consequently, by selecting the proper antenna frequency, survey time and cost can be reduced. Also, appropriate antenna frequency helps to achieve an acceptable accuracy in determining the depth of buried targets. For example, in subsurface utility mapping, an accuracy of (+/- 10 cm or better) in locating buried targets is a requirement for the Quality Level A by the American Society of Civil Engineers (ASCE) (Jaw and Hashim, 2013). This shows that serious consideration must be undertaken regarding the choice of the antenna frequency.

The objectives of this study at our La Marque Geophysical Observatory near Houston are to: (1) study the soil dielectric constant and the corresponding radar velocity, (2) determine the radar velocity to best image shallow buried anomalies, (3) observe the effect of varying frequencies on the target detectability, image clarity, shape, propagation distance, and depth accuracy, and (4) provide a definitive data set for analysis tests. All of the radar data used in this study can be found at www.agl.uh.edu/GPRdataUHCoastalCenter.zip

2.2 Test site

We selected a test site that would have a strong target response with verifiable characteristics. Our targets were culverts, at the University of Houston's La Marque Geophysical Observatory near Houston, Texas, which support a road crossing one of the area's bayous (Figure 2.1). The culverts are made of corrugated steel pipe coated with zinc-galvanized aluminum and make excellent GPR targets. The culverts' major axis lies in the north-south direction; their diameter is 2.5 m, and the distance between adjacent centers is 3.3 m. The length of each culvert is 12.36 m. A mixture of crushed limestone and oyster shells covers the first 15 cm of the top of the surface road. Stabilizer sand filled the remaining space to the culverts top (Smith et al., 2014). A telephone line is suspended over the north side of the culvert. The shortest distance of the telephone line to the perimeter of the grid is 2.57 m (two-way travel time in air of 17 ns). However, inspection of our subsequent data shows no evidence of scattering from the telephone line.

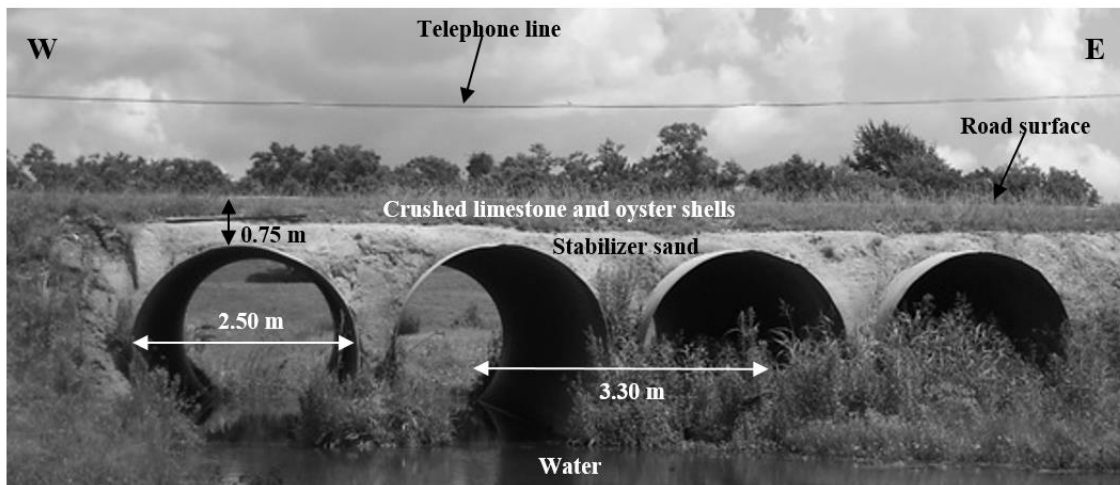


Figure 2.1. Photograph of the culverts supporting a road over a bayou at the University of Houston's geophysical test site near Houston, Texas. The diameter, distance between the adjacent culverts, and the depth to the top of the culvert are annotated.

To illustrate the general GPR data quality and illumination (to be discussed in detail later), we overlaid a depth-stretched GPR section from the 250 MHz system over a photograph of the buried culverts (Figure 2.2). As would be anticipated, the data identifies the culvert tops very well.



Figure 2.2. A GPR section (stretched to depth) from the 250 MHz system is overlain on a photograph of the culverts.

2.3 Soil measurement and numerical modeling

In addition to the antenna frequency, GPR success is often affected by the soil physical parameters such as the dielectric constant and conductivity. It is often that these parameters are unknown, highly variable, and depend on a specific site. In this study, we collected an unconsolidated, dry soil sample taken from the top of the culverts. The soil was emplaced in a 0.08 m diameter and 0.13 m long plexiglass cylinder tube. An Agilent 85070E Dielectric Probe Kit was used to test the sample across a range of frequencies (100 – 1000 MHz); the dielectric constant was 5.2 for all frequencies. This is within the range of the dielectric constant of dry sand measured at 100 MHz in the literature (4 - 6) as

reported by Daniels (1996). Van Heteran et al. (1998), Davis and Annan (1989), Theimer et al. (1994), Van Overmeeren (1994), and Neal and Roberts (2000) stated a dielectric constant of 3.5 to 6.5 for unsaturated sand measured at 80 – 120 MHz. For low-loss, and non-magnetic materials ($\sigma/\omega\epsilon \approx 0$), we use the Equation (2.1) to estimate the radar velocity:

$$v = \frac{c_o}{\sqrt{\epsilon_r}}, \quad (2.1)$$

where c_o is the radar velocity in the vacuum (0.3 m/ns), and ϵ_r is the dielectric constant of the material. The calculated velocity for the dry sand is 0.13 m/ns.

Water saturation lowers the velocity of the dry matrix (Conyers, 2004). As a consequence, the dielectric constant of the matrix increases. Mukherjee, 2010 showed that dielectric constant values are inversely proportional to frequencies. To represent the soil condition in the field which is compacted and moist, we selected a dielectric constant value of 9 for the forward modeling (Daniels, 1996; Conyers and Goodman, 1997), which is consistent with stabilizer sand (5-15) and crushed shells (6-15) as indicated by Jol (2008). The corresponding velocity of saturated and compacted soil is 0.10 m/ns. Picking the top of the culvert is assisted by the polarity of the wavelet of the reflected signal (Figure 2.3d). The positive signals are displayed in black while negative signals are indicated in white. Modeling indicates that the wavelet polarity is reversed from the air wave upon reflection - as we expect from the low-impedance steel (Annan, 2004). The radargrams show the culvert response as a positive event (white) in the reflected signal (Figure 2.3c). Our pick for the culvert top will be based on a positive polarity arrival.

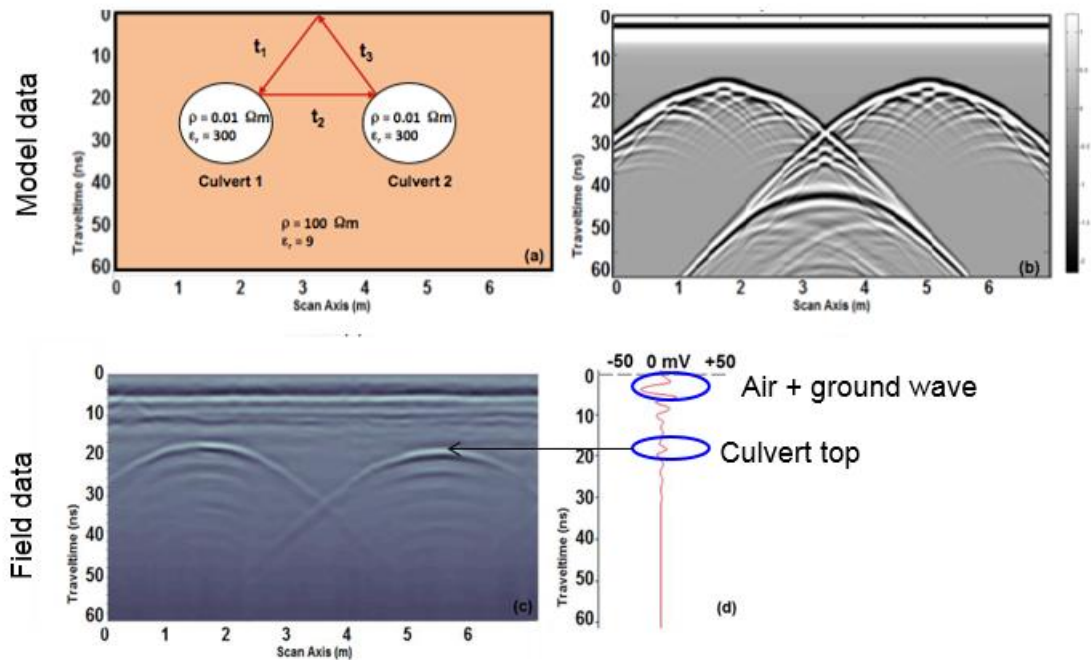


Figure 2.3. Schematic diagram of two adjacent culverts with material dielectric values annotated (b) Simulated GPR at 250 MHz. (c) 250 MHz field data. (d) 250 MHz field data wavelet of the reflected signal. The deflection of the reflected wave at about 17 ns produces a positive signal (white).

2.4 Data acquisition

We acquired a total of 177 GPR lines in the X and Y directions (Figure 2.4) using three different antenna frequencies (100 MHz, 250 MHz, 1000 MHz) during two days in the summer of 2013. The data is available for download at (<http://www.agl.uh.edu/GPRdataUHCoastalCenter.zip>). The 250 MHz data were acquired on the first day (28° C, 82 % humidity, 8-knot wind) and the remaining surveys done on the second day. It had rained before the surveys (average precipitation of 2.5 in.) although the road materials are very permeable and drained rapidly. The second day's

weather was dry with no rain, and the average temperature was 30° C. We used the integrated Sensors & Software Noggin Smart Cart (250 MHz and 100 MHz) and Pulse EKKO PRO systems (100 MHz and 1000 MHz).

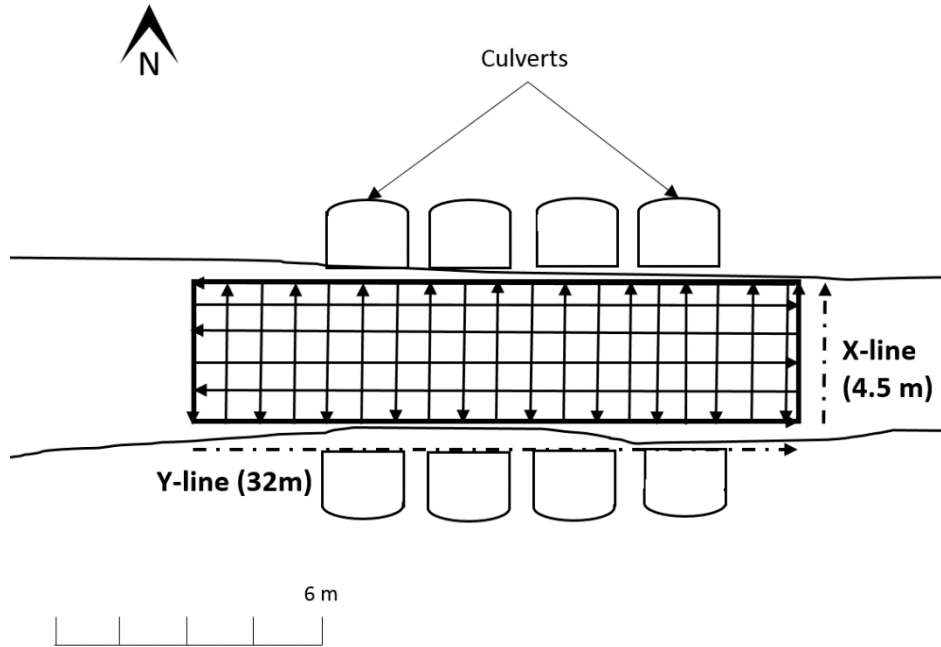


Figure 2.4. A forward and reverse collection method was employed to obtain an orthogonal survey grid.

A 32 m by 4.5 m horizontal survey grid was designed on the road above the culverts. Inline sampling was from 1 cm to 10 cm (from 1000 MHz to 100 MHz antenna) with inline and crossline spacing ranging from 20 cm to 50 cm respectively. It took approximately 2.5 hours to build the grid and another 2 hours to complete the scanning for the 100 MHz and 250 MHz. Acquiring the 1000 MHz data required more care and time because of the sensitive equipment over the gravel road. We used spray paint and strings to mark the survey grid. We also collected GPR lines perpendicular to the culvert's major axis using 400 MHz and 900 MHz antennas manufactured by Geophysical Survey Systems, Inc.

(GSSI). These data were acquired in the summer of 2014, and the weather was again humid (84 % average humidity) with an average temperature of 26 °C. The average wind was 14 mph with no precipitation and dry soil. The details of the survey parameters are summarized in Table 2.1.

Table 2.1. Survey parameters for the five antenna systems.

Antenna frequency	100 MHz	250 MHz	400 MHz	900 MHz	1000 MHz
Date	06/12/2013	06/10/2013	09/12/2013	05/21/2014	01/18/2014
Soil conditions	Unsaturated	Saturated	Unsaturated	Unsaturated	Unsaturated
Survey dimension	32 m x 4.5 m	32 m x 4.5 m	32 m	18 m	1.6 m x 1.6 m
Line spacing	Y-line:0.5 m X-line:0.5 m	Y-line:0.25 m X-line:0.5 m	N/A	N/A	Y-line:0.2 m X-line:0.2 m
Step size	0.1 m	0.05 m	0.017 m	0.016 m	0.01 m 0.02
Vertical stacking	128	64	64	64	32
Sample rate	0.80 ns	0.40 ns	0.11 ns	0.08 ns	0.1 ns
Antenna separation	0.5 m	0.27 m	0.16 m	0.15 m	0.07 m
Average number of traces	333	636	1920	1152	3442
Number of points/trace	111	217	512	512	700

Moisture content and effective porosity have a strong control over dielectric properties of rocks which in turn affect GPR signal penetration directly in carbonate terrains. Inverse relation exists between the depth of penetration and moisture content for all antenna frequencies (50, 200, 400, and 500 MHz) (Damayanti, 2010). We investigated the effect of the variation of saturation in the soil to the GPR response in 250 MHz data. It had rained about 0.5 in. on June 9th then the soil drained for at least 10 hours before the first 250 MHz data set was acquired. On June 10th. The soil drained for another 48 hours before another GPR profile was acquired on June 12th as shown in Figure 2.5 (Weather Almanac). It is observed the data quality in Figure 2.7 are similar except the surface shows fuzziness between 0 to 12 m in Figure 2.7b. Hyperbola fitting shows the average velocity is higher (0.114 m/ns) in the less saturated 250 MHz data compared to the velocity of more saturated data (0.109 m/ns). Neal (2004) stated that the percentage velocity change from saturated to unsaturated sand is 25 %. We observed the percentage change in the velocity between the more saturated and less saturated 250 MHz data is about 5 %. This shows the effect of the saturation can be seen in the data and measured but relatively modest in the data quality and velocity.

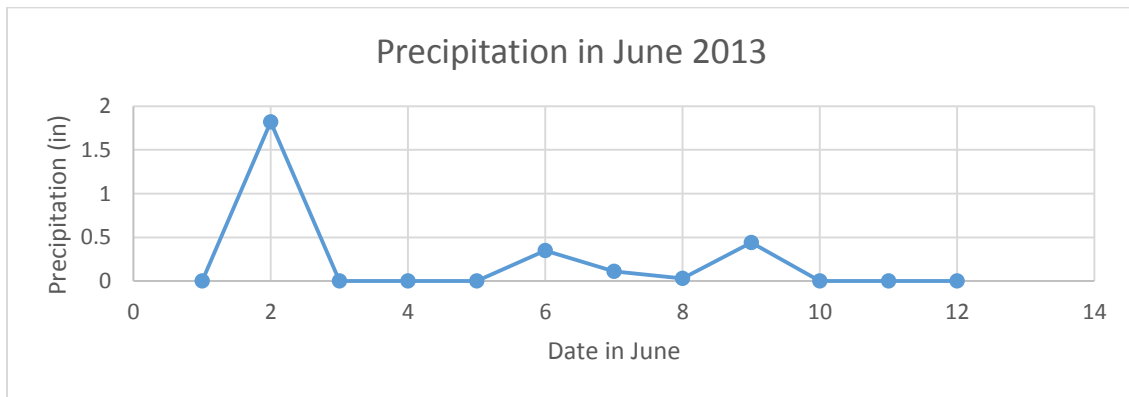


Figure 2.5. Average precipitation at La Marque, Texas between 1st of June to 12th of June 2013.

We observed the GPR responses by comparing the GPR radargram as shown in Figure 2.6 and Figure 2.7.

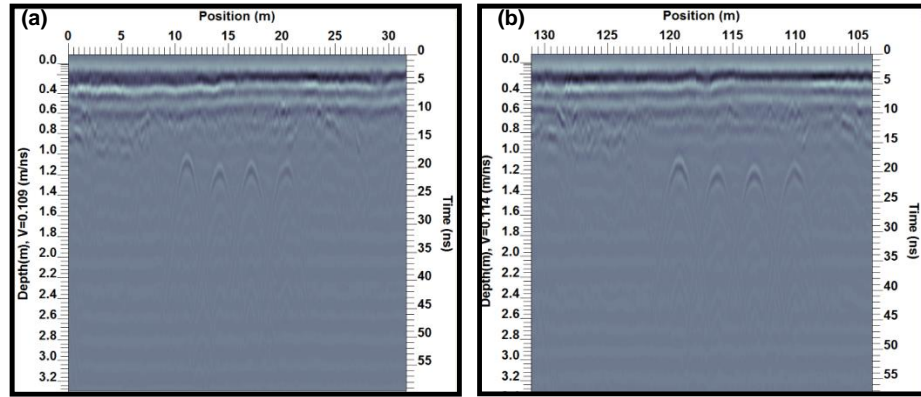


Figure 2.6. (a) 250 MHz after rain raw data with dewow applied (b) 250 MHz with 48 hours drying data with dewow applied.

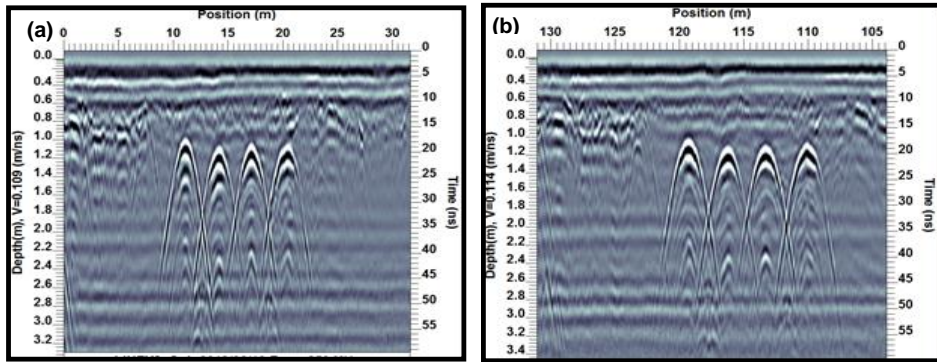


Figure 2.7. (a) 250 MHz after rain data with dewow and gain applied. (b) 250 MHz with 48 hours drying data with dewow and gain applied. Both have the same gain parameters applied.

We also compared the frequency spectrum and the average-Time amplitude plot to look for any differences as shown in Figure 2.8 and Figure 2.9 respectively. The frequency spectrum of both data do not show much difference.

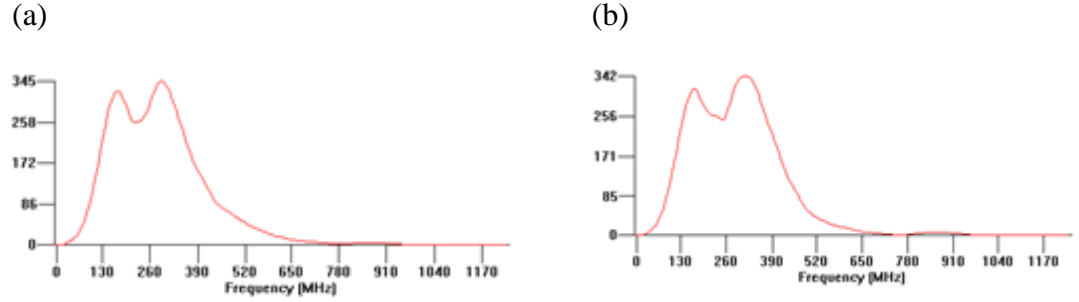


Figure 2.8. (a) Average-Frequency spectrum of 250 MHz after rain data (b) Average-Frequency spectrum of 250 MHz with 48 hours drying data.

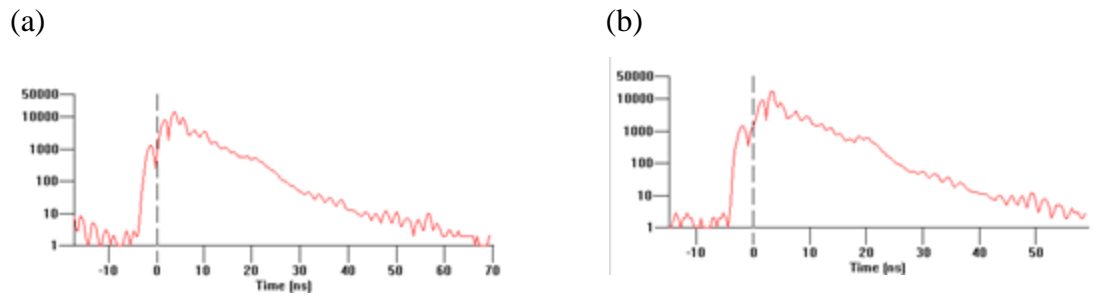


Figure 2.9. (a) Average-Time amplitude plot of 250 MHz after rain data (b) Average-Time amplitude plot of 250 MHz with 48 hours drying data.

2.5 Data processing

The processing for the 100 MHz, 250 MHz, and 1000 MHz data was undertaken using Sensors & Software processing package EKKOView Deluxe while 400 MHz and 900 MHz data were analyzed with GSSI's RADAN 7. The main steps in the standard data processing are time-zero correction, dewow, deconvolution, background subtraction, and gain (Ulriksen, 1982; La Fleeche et al., 1991; Fisher et al., 1992; Fisher et al., 1996). Additional data processing such bandpass filtering were also performed and the results are in Appendix. The dewow is to remove the low frequency component of the GPR system

(Aitken, 2008). Figure 2.10 shows our GPR profiles for 100, 250, 400, 900, and 1000 MHz frequency antenna after time-zero correction, dewow, deconvolution, background subtraction, and gain.

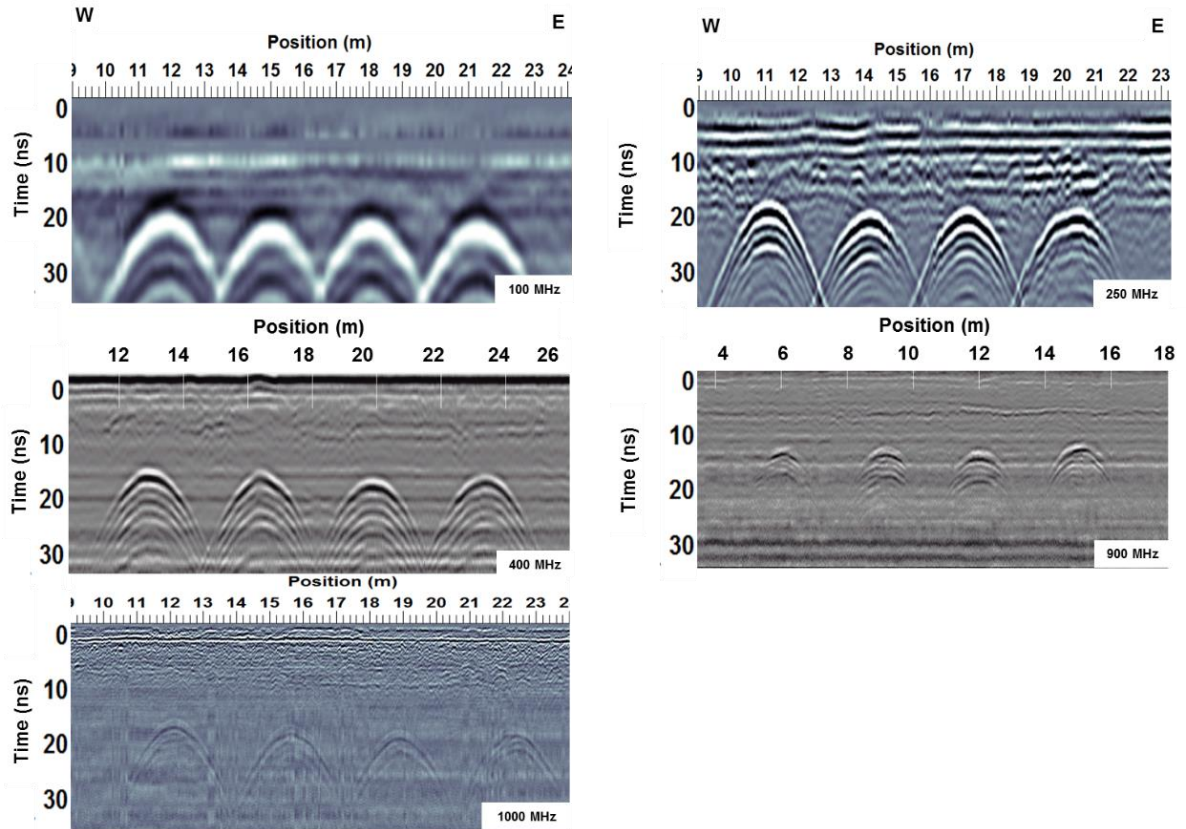


Figure 2.10. GPR profiles at the La Marque, Texas test site for 100, 250, 400, 900, and 1000 MHz frequency antennas after time-zero correction, dewow, deconvolution, background subtraction, and gain were applied. All profiles run from East to West.

Figure 2.11 shows the frequency spectrum of 100, 250, 400, 900, and 1000 MHz data.

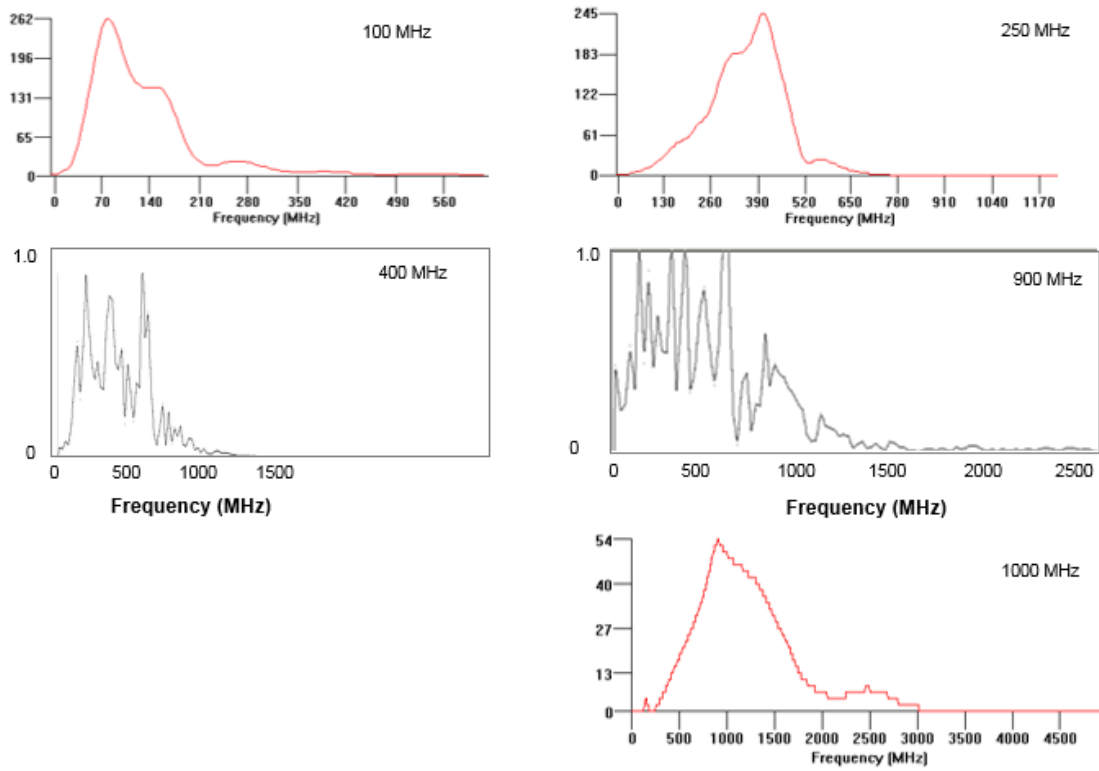


Figure 2.11. Frequency spectrum of 100, 250, 400, 900, and 1000 MHz.

To estimate the soil's GPR velocity, we employ several techniques: soil measurements in the lab, a common-midpoint (CMP) or expanding spread survey along the axis of the culvert, calculation of the culvert's known depth and the picked time at the zero-offset, and migration focusing. The CMP survey data were acquired using a bistatic Pulse EKKO PRO 100 MHz system in October 2013 with no precipitation prior to the survey. The transmitter and the receiver positions are incremented along the culvert axis at a fixed step (20 cm). The analysis in the lab using a best-fit hyperbola yielded a velocity of 0.08 m/ns (Figure 2.12a). Figure 2.12b shows the semblance analysis indicating velocities between 0.07 and 0.10 m/ns. The average velocity estimate of the 250 MHz data using the culvert

top known depth and the picked time at the zero-offset yields 0.08 m/ns.

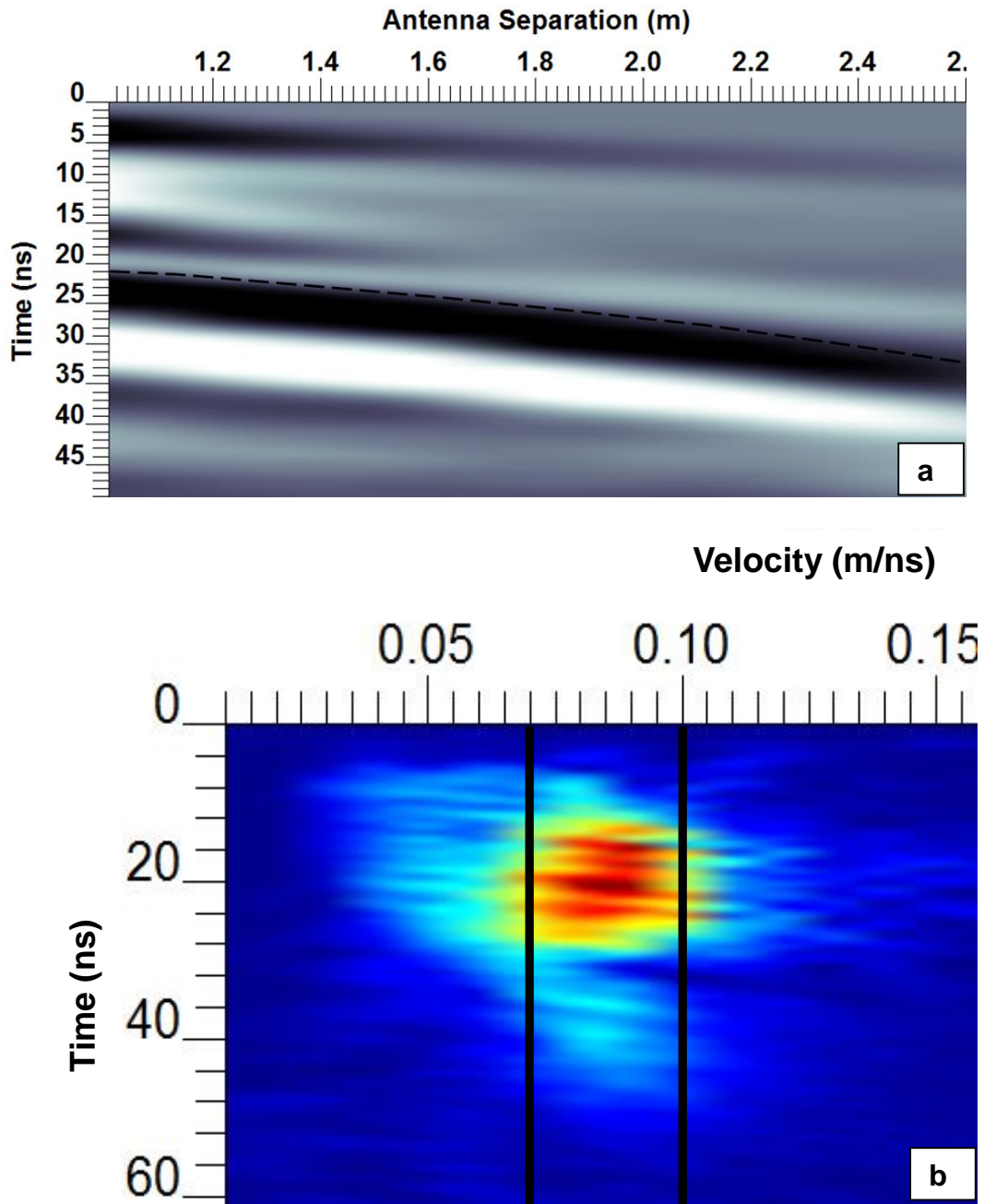


Figure 2.12. (a) GPR gather from the CMP survey with a hyperbola (dashed black curve) fit to the reflector. The hyperbola fit on the reflector arrival results in an average velocity of 0.08 m/ns. (b) Velocity semblance results in the range of 0.07 to 0.10 m/ns.

We applied 2D Kirchhoff migration as shown in Figure 2.13 and Figure 2.14 with different migration velocities (0.07 m/ns to 0.10 m/ns) applied to the 250 MHz data. The migration aim is to collapse the diffraction energy to their "original point source" (Aitken, 2008). Time-zero correction, deconvolution, dewow, background subtraction, and gain were applied before the migration. Sections in Figures 2.13a and 2.13b, using velocities of 0.07 m/ns and 0.08 m/ns, respectively, seem to provide optimal migrated sections which resemble the shape of the culverts. Figure 2.13b is overlain on the photograph of the culvert to show that the data identifies the top of the culvert as expected.

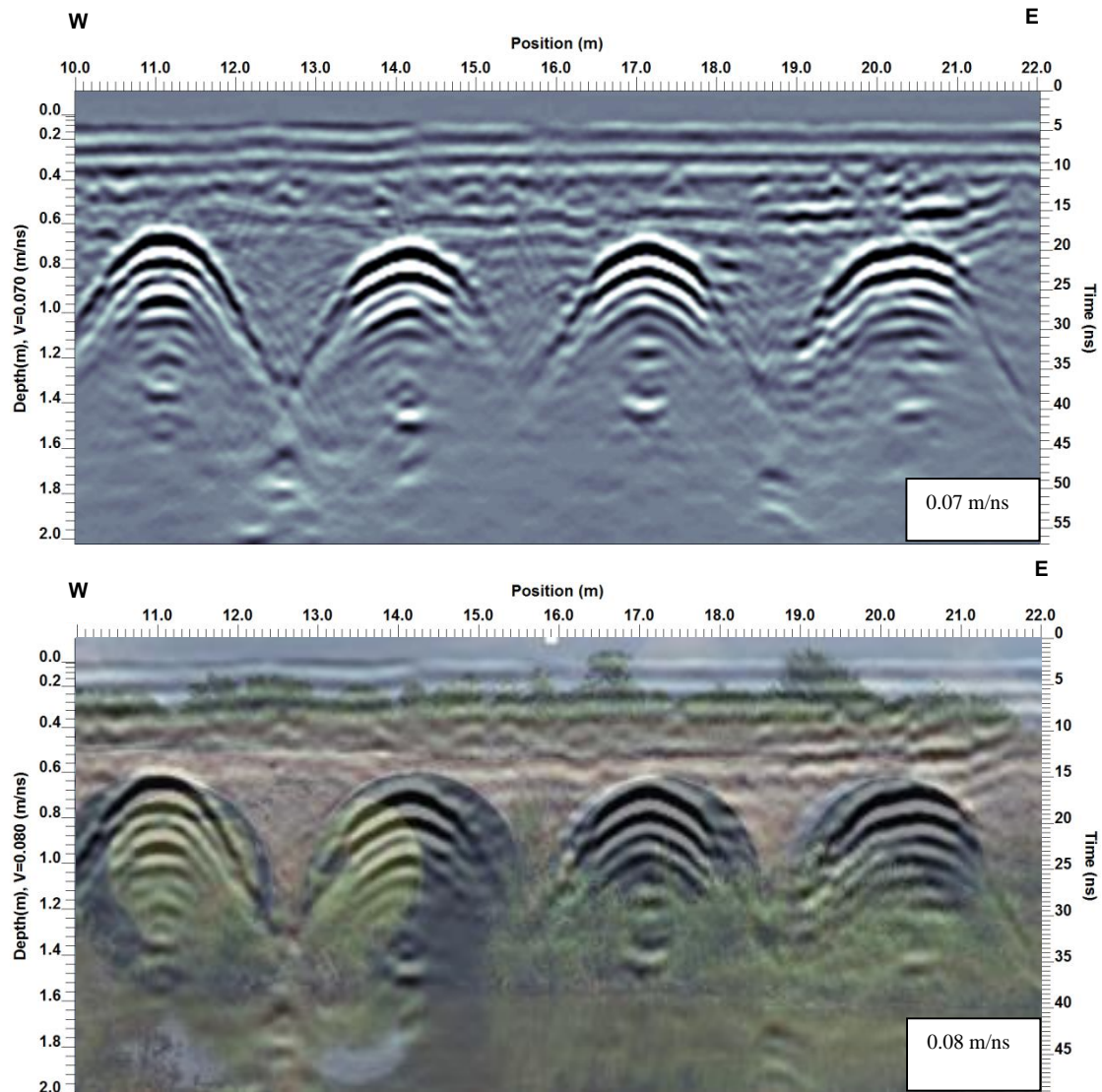


Figure 2.13. Migrated sections of 250 MHz data using velocities from 0.07 m/ns to 0.08 m/ns. Basic processing includes time-zero correction, dewow, deconvolution, background subtraction, and gain before the migration. Optimal migrated sections are found in Figures 2.13a and 2.13b using velocities of 0.07 m/ns and 0.08 m/ns, respectively with diffractions largely collapsed.

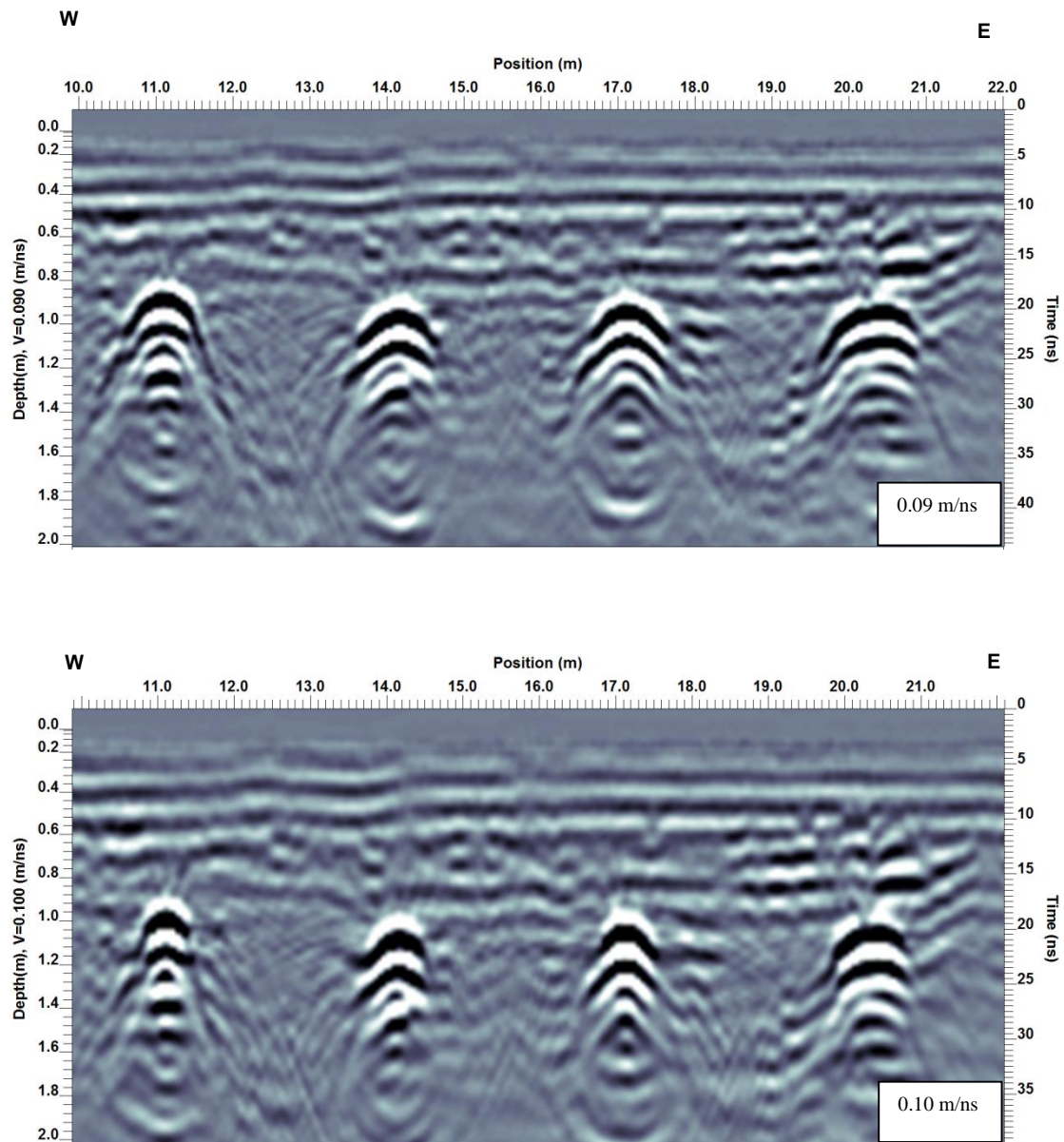


Figure 2.14. Migrated sections of 250 MHz data using velocities from 0.09 m/ns to 0.10 m/ns. Basic processing includes time-zero correction, dewow, deconvolution, background subtraction, and gain before the migration. Migrated sections in Figures 2.14a and 2.14b using velocities of 0.09 m/ns and 0.10 m/ns yield over migration.

We used the time-zero correction, dewow, deconvolution, background subtraction, gain, migration to process 100 MHz data (Figure 2.15a). Horizontal banding has been reduced using background subtraction. The migrated shape indicates the culverts' tops but with a

lower image resolution than that of 250 MHz data (Figure 2.15b).

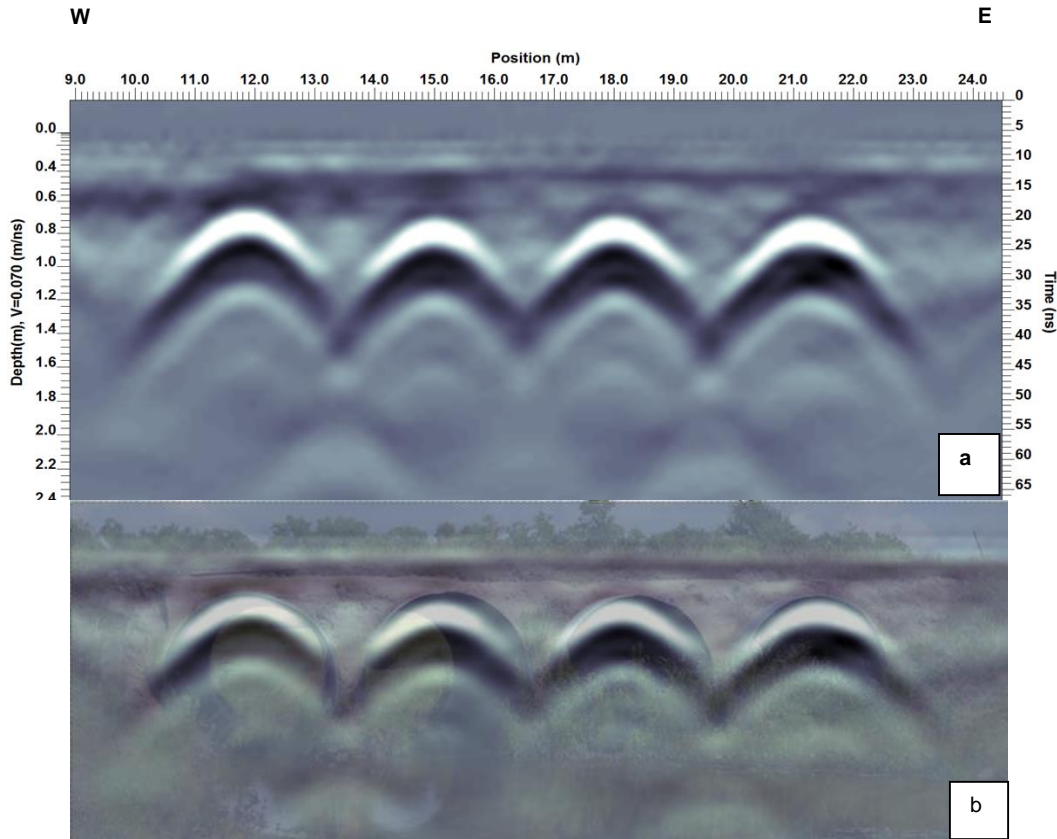


Figure 2.15. (a) The migration result of 100 MHz data using the velocity of 0.07 m/ns. (b) The migrated image overlain on the culvert photograph shows the shape of the migrated image indicates the culverts' tops but with a lower image resolution than that of 250 MHz.

We used time-zero correction, dewow, deconvolution, background subtraction, gain, and migration to process 400 MHz data. The result shows the culverts' top and shape (Figure 2.16). We used a range of velocities to achieve an optimum migration result. We found 0.10 m/ns seemed to provide the most reasonable image outlining the culverts' shape. The migrated image has a higher resolution than 250 MHz data.

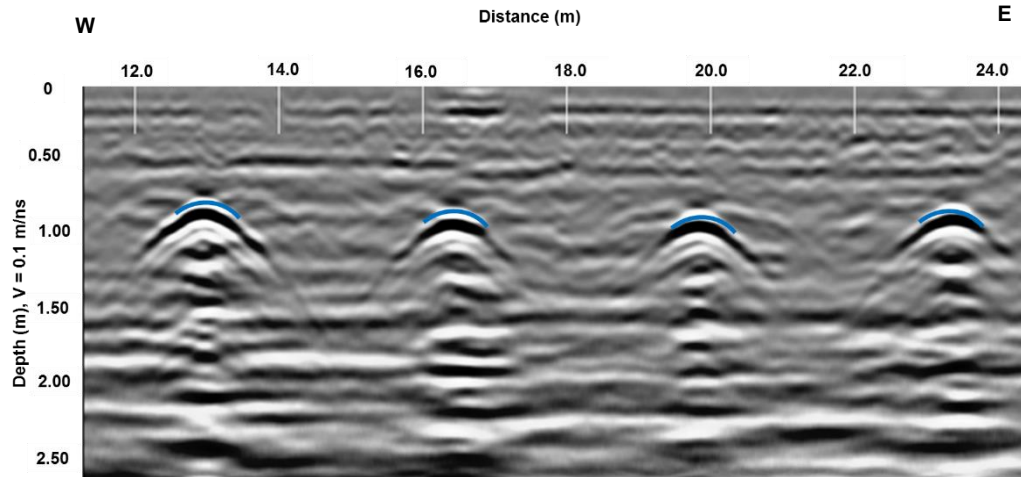


Figure 2.16. Migration result of 400 MHz data using the velocity of 0.10 m/ns. The result shows the culverts' top and provides some shape information. The culvert shape is outlined in blue.

Figure 2.17 shows the migrated 900 MHz data. We again applied time-zero correction, dewow, deconvolution, background subtraction, and migration to process the data. The resultant image has a higher frequency than 400 MHz data. The top of the culvert is evident; however, there is little information about the culverts' shape.

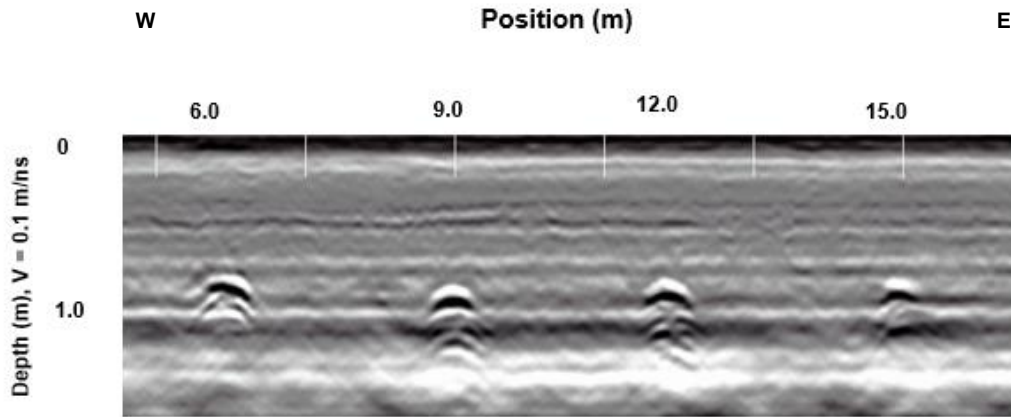


Figure 2.17. Migration result of 900 MHz data using the velocity of 0.10 m/ns. The top of the culvert is evident; however, there is limited information about the culverts' shape as seen in Figures 2.9 and 2.10.

Lastly, Figure 2.18 shows the 1000 MHz data after pre-processing and migration with a velocity of 0.12 m/ns. The top of the culvert was obvious, but the culvert shape was not clearly imaged. The image has a higher resolution than 900 MHz data.

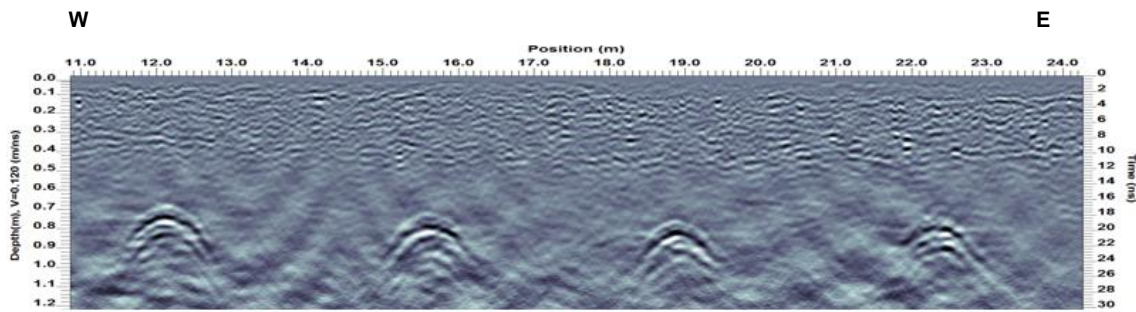


Figure 2.18. Migration result of 1000 MHz data using the velocity of 0.12 m/ns. The culvert's tops are clear with some coverage of the culvert's curvature.

We also examined a different processing flow (Gabor deconvolution followed by shot-record Gazdag prestack depth migration (PSDM) for the GPR data (Smith et al., 2014). The migrated result was very similar to the Kirchhoff migration (Figure 2.19).

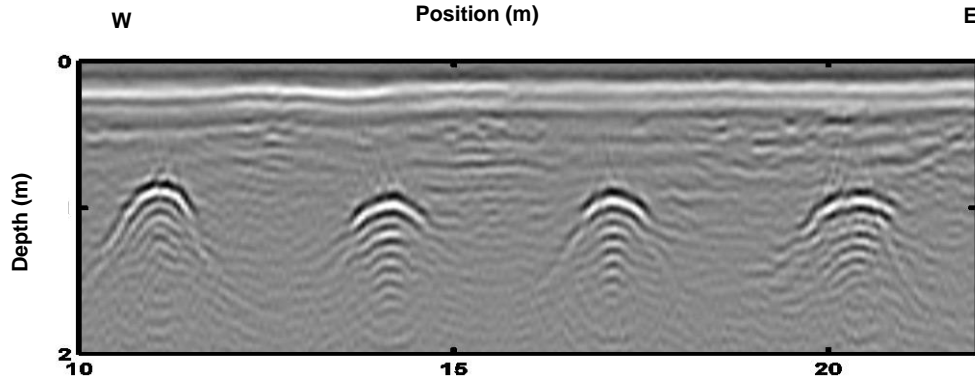


Figure 2.19. Migration result of 250 using MHz data using the Gabor deconvolution followed by shot-record Gazdag prestack depth migration (PSDM) with a velocity of 0.10 m/ns.

We note that the migration velocities giving our interpretation of the best-collapsed diffractions, measured across antenna bands (100 MHz to 1000 MHz) ranged from 0.07 m/ns to 0.12 m/ns. We summarize the velocity used to migrate each frequency data in Figure 2.20. While there is some range of usable imaging velocities, we see a suggestion of frequency dependency of the velocity. The velocity increased from the 100 MHz to 400 MHz, unchanged from the 400 MHz to 900 MHz, and increased again from the 900 MHz to 1000 MHz. Lai et al. (2011) suggest that GPR velocity changes from 0.07 m/ns to 0.11 m/ns in the low-frequency region and approaches a relatively constant at a higher frequency range. Patriarca et al. (2013) reported Q often increases linearly across a frequency region of 300 KHz and 1.5 GHz. This suggests the frequency dispersion is higher in the lower frequency. Soil materials can show significant dispersive properties in the GPR frequency range (Lambot et al., 2005).

The migrated GPR data for the 250 MHz antenna were exported to Voxler 3D visualization software from EKKO Mapper. We display a representative volume (with the top at the depth of 0.71 m) in Figure 2.21. The culverts' shape, orientation, and dimension are visible with their strong reflection events.

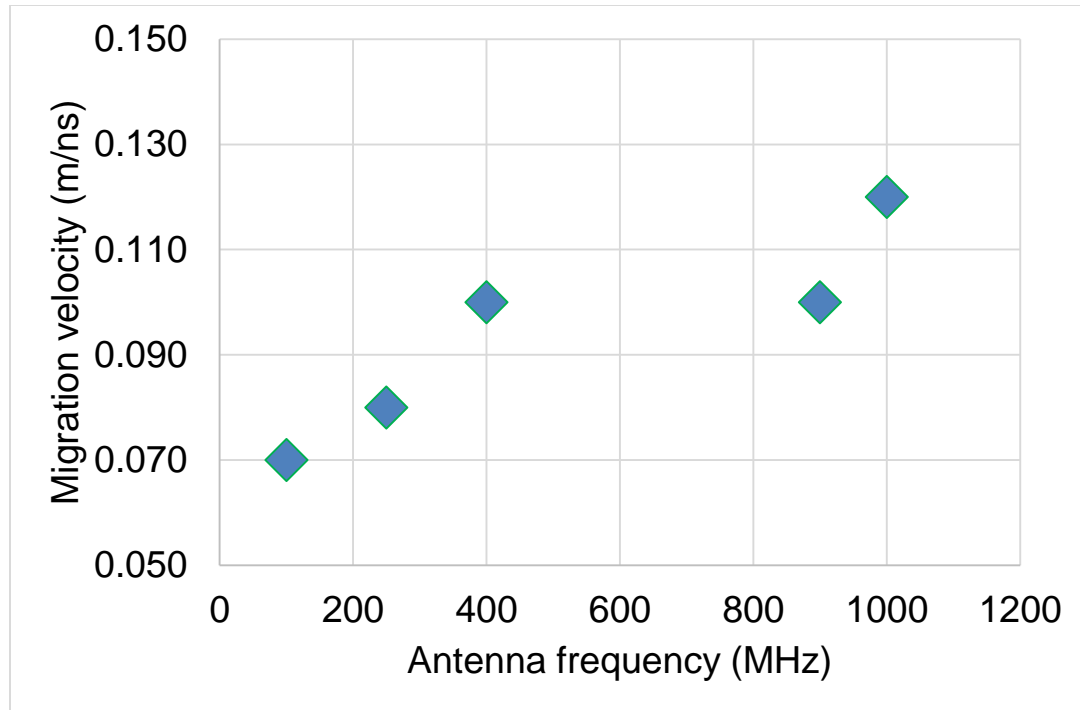


Figure 2.20. Best migration velocity versus antenna frequency shows frequency dependency.

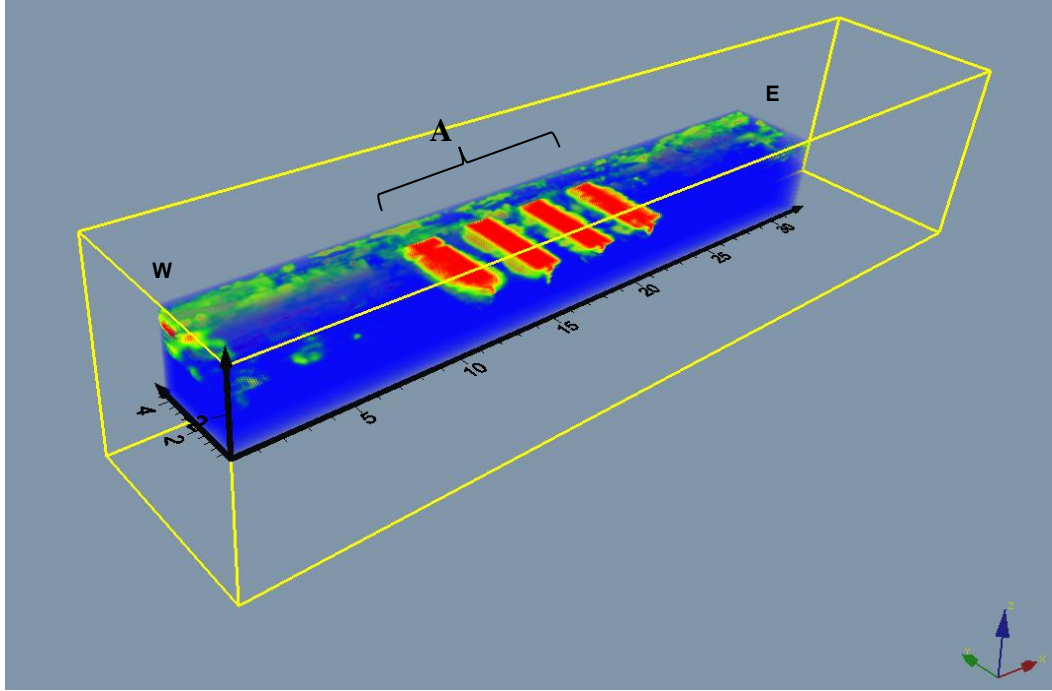


Figure 2.21. The 3D volume of 250 MHz data (with the top at depth 0.71 m) shows the high amplitude regions (A) corresponding to the top of the four buried culverts.

2.6 Comparison of the antenna frequencies on GPR images

To evaluate the antenna frequency impact on the GPR image, we observed the target detectability, shape, image clarity, and the propagation distance. The comparison of the five antenna frequencies on the migrated GPR images is summarized in Table 2.2. The GPR data from all frequencies imaged the four diffraction hyperbolas which suggest the presence of anomalies. This implies all the frequencies can be used to detect the culverts. The 100, 250, and 400 MHz systems provided overall the most representative image of the target culverts. Data acquired with 900 and 1000 MHz antenna showed less information about the culvert shape. This may be due to the antenna directivity effect in the higher frequency region where it is narrower than in the lower frequency range as reported by

Annan (2004). The observation on the hyperbola radius of curvature shows it increases as the frequency decreases. Hyperbolas in the higher frequency antennas (900 MHz and 1000 MHz) GPR images have a smaller radius of curvature, and they only capture the top of the culvert. This suggests 100, 250, and 400 MHz were best suited to image the shape of the culvert. The GPR images show that overall the 100 MHz image is blurry while the images for the rest are sharp. This shows that the 100 MHz system is not suitable for inspecting the condition of the culvert. The propagation distance can be used as a proxy to determine the maximum penetration depth. The maximum penetration depth can be estimated by the Equation (2.2):

$$d_{max} < \frac{0.035}{\sigma} , \quad (2.2)$$

Where σ is the soil conductivity in S/m (Sensors & Software). We used $\sigma = 0.01$ S/m (used in the forward model) and obtained the maximum depth of penetration of 3.5 m. The propagation distance is measured from the point on the surface that is directly above the location when the diffraction tail disappears to the point tangential to the culvert radius of curvature as shown in Figure 2.22.

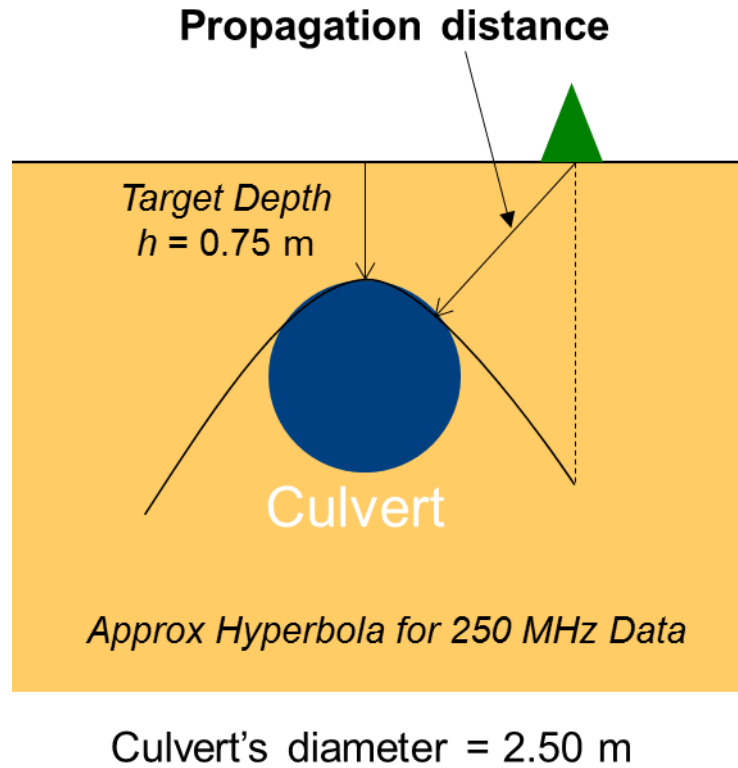


Figure 2.22. Schematic diagram of propagation distance calculation.

We take into account the 250 MHz after the rain and with 48 hours drying data. The results of the calculation of the propagation distance and the average velocity of the 250 MHz data in saturated and unsaturated is minimal. The calculated propagation distance of 250 MHz in the saturated soil is 2.1 and the propagation distance in the unsaturated soil is 2.2 m. These suggest that the differences in frequencies are due to the different antennas and not due to the different conditions. We observe a decreasing trend in the propagation distance as the frequency increases as shown in Figure 2.23.

The maximum propagation distance given by the 100 MHz is within the calculated value above. The comparison with the depth estimate as a function of the frequency reported by Annan (2004) shows a reasonable agreement. The relationship also predicts the maximum frequency that can be used to achieve the desired propagation distance. The calculated propagation distance for the unsaturated is 2.2 m compared to 2.13 for the saturated data.

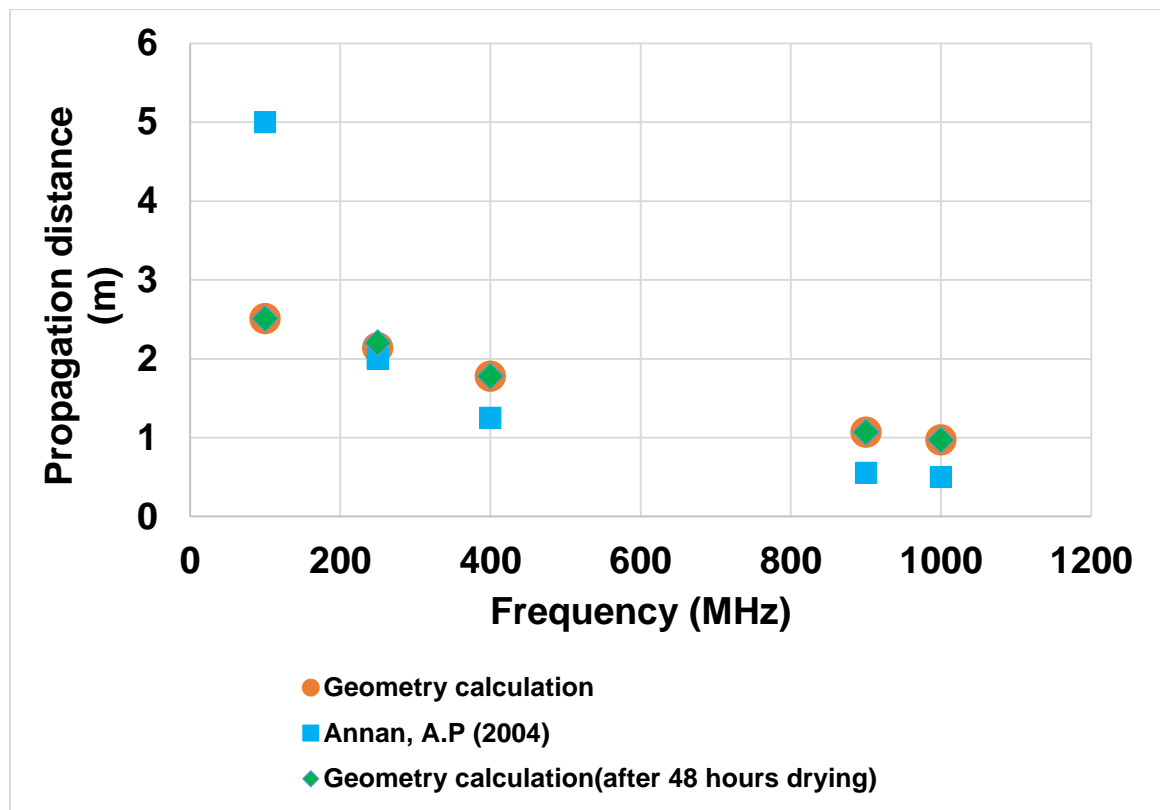


Figure 2.23. The plot of the propagation distance as a function of frequency. The comparison with the depth estimate as a function of the frequency reported by Annan (2004) shows a reasonable agreement with the calculated propagation distance.

We also calculated the SNR in dB and compared the values across the antenna frequencies as shown in Figure 2.24. 250 and 400 MHz yielded the highest SNR values which are 10.71 and 9.4 dB respectively.

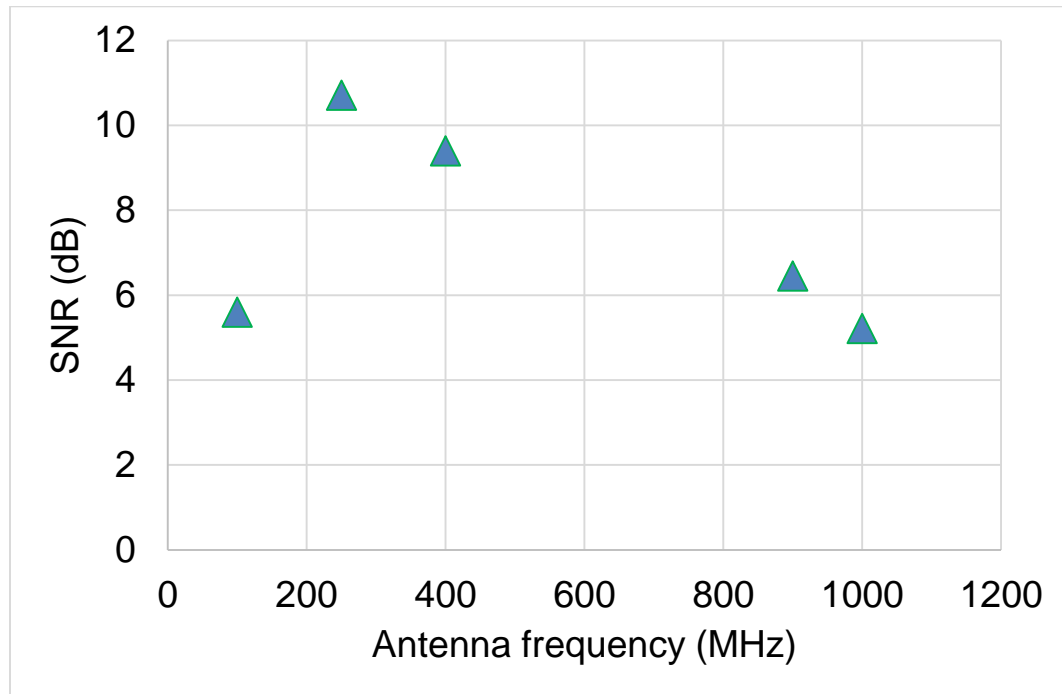


Figure 2.24. The effect of SNR with the varying frequencies.

To further assess, we compared the depth estimate from the migrated GPR images to the total station elevation data. Total station elevation data with 1.5 mm accuracy was acquired to determine the actual depths of the culverts. Figure 2.25 shows a cross plot of GPR depth and total station depth. The depth obtained from the 250 MHz and 900 MHz antenna are consistent with the depth measured by the total station. Determining the top of the culvert on 250 MHz, and 900 MHz data was easier due to the sharper reflection

events while it was achieved with less confidence level for the 100 MHz data. We observe the average absolute deviation is consistent with the 250, 400, 900, and 1000 MHz antenna. 100 MHz antenna gives 2 cm deviation. We predicted a linear increment in the depth accuracy as the frequency increases. However, we found that the depth accuracy is constant across the frequency except at the 100 MHz antenna. The higher error can be attributable to the lower depth picking confidence on the blurry 100 MHz GPR image.

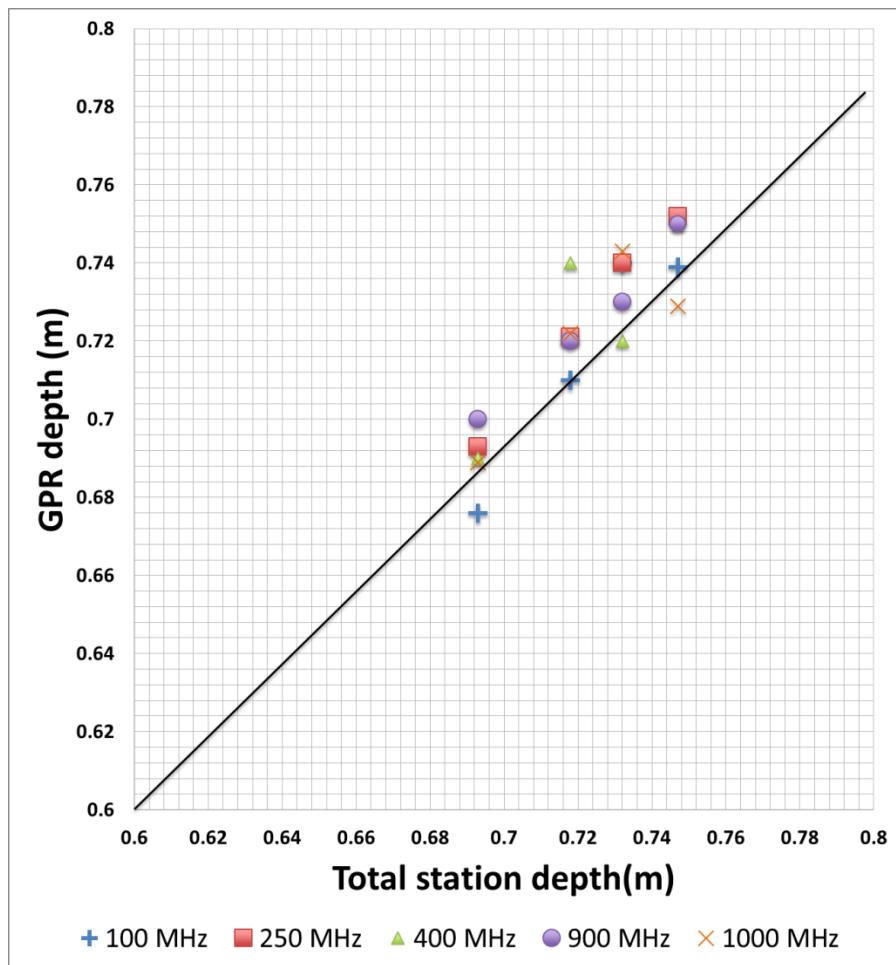


Figure 2.25. The plot between GPR depth and total station depth for five antennas. The black line is the equality line to represent a slope of 1.0 between GPR and the total station.

Table 2.2. Comparison of five antenna frequencies on the migrated GPR images.

Frequency (MHz)	Target Detected	Hyperbola Shape	Image Clarity	Propagation Distance (m)	Depth Accuracy
100	Yes	Resembles culvert shape	Blurry	3.2	+/- 0.02
250	Yes	Resembles culvert shape	Sharp	2.8	+/- 0.01
400	Yes	Resembles culvert shape	Sharp	2.3	+/- 0.01
900	Yes	Resembles culvert top	Sharp	1.2	+/- 0.01
1000	Yes	Resembles culvert top	Sharp	1.0	+/- 0.01

2.7 Conclusions

We have presented a case study of subsurface culvert imaging using a variety of GPR antenna frequencies, systems, and processing flows. Data from this GPR study can be found at www.agl.uh.edu/GPRdataUHCoastalCenter.zip. A soil sample from our La Marque, Texas test area, gave a dielectric constant of 5.2 from lab measurement with a corresponding soil velocity of 0.13 m/ns (dry and unconsolidated). Velocities from a common-mid point (CMP) survey, using the 100 MHz antenna, were between 0.07 m/ns to 0.10 m/ns. The average velocity estimate of the 250 MHz data using the known depth to culvert top and the picked time at the zero-offset yields 0.08 m/ns. Various velocities were used for the migration of each antenna's data (to allow possible velocity dispersion). The 100 MHz data were best migrated using 0.07 m/ns, 0.08 m/ns for the 250 MHz data, 0.10 m/ns for the 400 MHz, 0.10 m/ns for the 900 MHz, and 0.12 m/ns for the 1000 MHz. We found that the best velocity used for the migration suggests frequency dependency. We investigated the target detectability, shape, image clarity, propagation distance, and depth accuracy to evaluate the effect of varying frequencies in GPR imaging. The presence of

diffraction hyperbolas in the GPR image confirmed that all the antenna frequencies were suitable to image the culverts. 100 MHz, 250 MHz, and 400 MHz defined the culvert top reasonably well and provided an image which suggested the culverts' shape. The propagation distance decreases as the frequency increases. We found that the depth accuracy is consistent across the frequency except at the 100 MHz antenna. Higher percentage error at the lower frequency such as 100 MHz may be attributable to the higher dispersion and lower resolution image. The result highlights that antenna frequency selection is critical, and it is controlled by the specific objective of the survey. The study also suggests an objective criteria that can be established for selecting the most suitable antenna frequency to image buried culverts in the same soil conditions.

Acknowledgement

The authors would like to thank the Allied Geophysical Lab (AGL) of the University of Houston for funding the project. We express our appreciation to Adrian Smith of University of Calgary for providing PSDM imaging code. We are thankful to Dr. Yinxi Zhang of Baker Hughes for the soil dielectric measurement.

References

Aitken, J. A, 2008, Exploring Maya ruins in Belize, Central America using ground-penetrating radar (GPR): M.S. thesis, University of Calgary.

Annan, A.P., J. E. Scaife, and P. Giamou, 1990, Mapping buried barrels with magnetics and

ground-penetrating radar: 60th Annual International Meeting, SEG, Expanded Abstracts, 422–423.

Annan A. P., 2004, Ground Penetrating Radar: Principles, Procedures & Applications. Sensors & Software, Inc., Toronto, Canada.

Benedetto, D. D., R. Quarto, A. Castrignano, and D. A. Palumbo, 2015, Impact of data processing and antenna frequency on spatial structure modelling of GPR data: Sensors, 16430-16447.

Conyers L. B and D. Goodman, 1997, Ground-Penetrating Radar – An Introduction for Archaeology: Walnut Creek.

Conyers L. B, 2004, Ground-Penetrating Radar for Archaeology: AltaMira, Walnut Creek.

Czarnowski, J., S. Heinze, P. Bruhl, C. Staib, M. Robeck, G. Frank, and R. Fruhwirth, 1994, Pipeline projects in Germany using GPR: 5th International Conference on GPR, Expanded Abstracts, 1107–1113.

Daniels, D. J., 1996, Surface-penetrating radar: The Institute of Electrical Engineers.

Davis, J. L. and A. P. Annan, 1989, Ground-penetrating radar for high resolution mapping of soil and rock stratigraphy: Geophysical Prospecting, 3, 531–551.

Fisher, E., G. A. McMechan, and A. P., Annan, 1992, Acquisition and processing of wide-aperture ground-penetrating radar data: Geophysics, 57, 495-504.

Fisher, S.C., R. R. Stewart, and H. M. Jol, 1996, Ground penetrating radar (GPR) data enhancement using seismic techniques: Journal of Environmental Engineering Geophysics, 1, 89-96.

- Francke, J.C., 2014, GPR Principles and Applications, in J. G. Webster and H. Eren, eds., Measurement, Instrumentation, and Sensors Handbook: CRC Press, 1-17.
- Graf, F. L., 1989, Use of ground-penetrating radar to pinpoint natural gas pipeline leaks: 59th Annual International Meeting, SEG, Expanded Abstracts, p. 226–228.
- Jaw, S. W., and M. Hashim, 2013, Locational accuracy of Underground Utility Mapping using Ground Penetrating Radar: Journal of Tunneling and Underground Space Technology, 35, 20-29.
- Jol H. M., 2008, Ground Penetrating Radar Theory and Applications: Elsevier.
- Hugenschmidt J., A. Kalogeropoulos, F. Soldovieri, and G. Prisco, 2010, Processing strategies for high-resolution GPR concrete inspections: NDT&E International, 334–342.
- Lambot, S., I. van den Bosch, B. Stockbroeckx, P. Druyts, M. Vanclooster, and E. Slob, 2005, Frequency dependence of the soil electromagnetic properties derived from ground-penetrating radar signal inversion: Subsurface Sensing Technologies and Applications, 6, 73-87.
- LaFle`che, P.T., J. P., Todoeschuck, O. G. Jensen, A. S. Judge, 1991, Analysis of ground-probing radar data: predictive deconvolution: Canadian Geotechnical Journal, 28, 134– 139.
- Lai W. L., T.Kind, and H. Wiggerhauser, 2011, Frequency-dependent dispersion of high-frequency ground penetrating radar wave in concrete: NDT & E International, 44, 267-273.

- Neal, A., and C. L., Roberts, 2000, Applications of ground-penetrating radar (GPR) to sedimentological, geomorphological and geoarchaeological studies in coastal environments, in K. Pye and J. R.L. Allen, eds., Coastal and Estuarine Environments: Sedimentology, Geomorphology and Geoarchaeology: Geological Society of London Special Publication, 175, 139– 171.
- Orlando L., 2007, Using GPR to Monitor Cracks in a Historical Building: 4th International Workshop on Advanced Ground Penetrating Radar, IEEE, Proceedings on IEEE, 45–48.
- Patriarca, C., F. Tosti, C. Velds, A. Benedetto, S. Lambot, and E. Slob, 2013, Frequency dependent electric properties of homogeneous multi-phase lossy media in the ground-penetrating radar frequency range: Journal of Applied Geophysics, 97, 81-88.
- Powers, H. M. and G. R. Olhoeft, 1996, Modeling the GPR response of leaking, buried pipes: SAGEEP Environmental Engineering Geophysical Society, SAGEEP, Expanded Abstracts, 525–534.
- Sensors & Software FAQ, 2016, Retrieved from <http://www.sensoft.ca/support/faq/>.
- Singh, K. K. K. and J. Francke, 2015, MineVue radar for delineation of abandoned mine galleries: Current Science, 107 (2), 181-183.
- Smith D. G. and H. M. Jol, 1995, Ground penetrating radar: antenna frequencies and maximum probable depths of penetration in Quaternary sediments: Journal of Applied Geophysics. 33, 93-100.
- Smith A. D., R. J. Ferguson, and R. R. Stewart, 2014, Georadar processing and imaging with Gabor deconvolution - Houston Coastal Center: GeoConvention, Expanded Abstract.

Stockbauer, F. S. and J. A. Kalinec, 1995, Real-time interpretation of EM-31 and GPR data for expedited site investigation: SAGEEP Environmental Engineering Geophysical Society, SAGEEP, Expanded Abstracts, 671–676.

Theimer, B.D., D. C. Nobes, and B. G. Warner, 1994, A study of the geoelectrical properties of peatlands and their influence on ground-penetrating radar surveying: Geophysical Prospecting, 42, 179– 209.

Tong, L. T., 1993, Application of ground penetrating radar to locate underground pipes: Terrestrial Atmospheric Oceanic Sciences, 4, 171-178.

Ulriksen, C. P. F., 1981, Application of impulse radar to civil engineering: Ph.D. thesis, Lund University of Technology.

Van Heteren, S., D. M. Fitzgerald, P.A. McKinlay, and I.V. Buynevich, 1998, Radar facies of paraglacial barrier systems: coastal New England, USA: Sedimentology, 45, 181–200.

Van Overmeeren, R.A., 1994, Georadar for hydrogeology: First Break, 12, 401–408.

Weather Almanac: Retrieved from www.wunderground.com

Zeng, X. and G.A McMechan, 1997, GPR characterization of buried tanks and pipes: Geophysics, 62, 797-806.

3 LOCATING AND CHARACTERIZING BURIAL USING 3D GROUND-PENETRATING RADAR (GPR) AND TERRESTRIAL LASER SCANNING (TLS) AT THE HISTORIC MUESCHKE CEMETERY, HOUSTON, TEXAS

Abstract

We use ground-penetrating radar (GPR), terrestrial laser scanning (TLS), cemetery records, and oral histories to locate and characterize unmarked burials at the Mueschke Cemetery in Houston, Texas. We employ the TLS survey for the reconnaissance of the various types of burials in the cemetery. Concrete burials were used after 1940 while wooden burials were common before 1940. Strong correlations of TLS shallow surface mounds and depressions with known burials provide substantial motivation to follow-up with a detailed investigation with GPR. To calibrate the GPR survey, we undertook excavation and lab experiments to measure relative dielectric constant (3-10), moisture content (14%-21%), and electrical conductivity (0.36-0.38 S/m) of the location's soil. Grain-size experiments indicated that the soil at the survey location is reasonable for GPR, which was subsequently reinforced by the high quality GPR images with a depth of penetration of about 2.5 m and a vertical resolution of 6 cm. Numerical modeling provided a signature of a concrete burial with a flat rectangular top while a wooden burial resembles a typical hyperbola shape. The burial characteristic from 2D GPR template surveys over concrete and wooden burials follow the numerical modeling findings. Three methods were used to estimate the

soil velocity: CMP, time-to-depth, and hyperbola fitting. These techniques yielded a soil velocity of about 0.055-0.067 m/ns. 3D GPR surveys produced anomalies that were consistent with headstones, cemetery records, and oral histories. Taking GPR depth slices overlain on the TLS elevation profile and cemetery records helped to ascertain the locations of the two suspected unmarked graves. The results demonstrate strong leads in locating the discovery of two unmarked burials including the oldest burial of James West through the geophysical characterization of different burial types using GPR and TLS methods.

3.1 Introduction

Ground-penetrating radar (GPR) has been widely used in archaeology and forensics to locate human burials and clandestine graves (Nobes, 2000; Davenport, 2001; Powell, 2004; Conyers, 2004; Schultz, 2007; Bode and Jol, 2005; Henning et al., 2008, Fiedler et al., 2009; Doolittle and Bellantoni, 2010; Damiata et al., 2013; Kadioglu, et al., 2013). GPR is often an ideal method because it is noninvasive, nondestructive, and can produce excellent images. Several GPR investigations of old cemeteries in Texas have resulted in significant contributions to archeologists, historians, and the local community. Henning, et al. (2009) discovered the abandoned Wyatt Chapel Cemetery that was used as a slave burial ground in Prairie View, Texas dating from just after the Civil War through GPR data and excavations. Johnson (2010) identified eight unmarked burial locations at the historical Watkins Cemetery in Sugar Land, Texas using GPR that provided significant historical records of African American graves. Angel Conejo-Martin et al. (2014) jointly used GPR and Lidar to characterize underground cavities in wine cellars in Atauta, Spain. Cavities

in the wet soil of Houston area is much more challenging than air cavities. However, we have not found formal studies on the integration of GPR and TLS to characterize and detect unmarked burials.

Documentation of burial practices through recollections of oral histories suggests some of the burials at the Mueschke Cemetery were only marked by flowers (such as lilies) because the family did not have the finances to buy headstones. There may be numerous other unrecorded and unmarked burials in the Mueschke Cemetery. Burials before 1940 were in wooden coffins, but burials after 1940 were in concrete vaults to avoid being washed away during floods (R. Stone 2013, pers. comm.). Field measurements (to be discussed later) show the burials are arranged in North to South rows which are spaced 1.5 m apart. This geometry provides additional guidance to locate unmarked burials. The oldest known, but as yet unlocated, burial is that of James R. West, who died in 1875. One of our goals is to find it (Aziz et al., 2013).

We present this case study to locate and characterize burials using 3D GPR and TLS surveys, assisted by historical records and oral histories for the Mueschke Cemetery (Figure 3.1). Through this study, we would like to answer the following questions: (1) Is GPR suitable in the generally clay-rich Houston area? (2) Can GPR locate a variety of burials (types, sizes, and depths)? (3) How do these buried targets appear in 3D? (4) Can we find previously unknown burials? Evans et al. (2014) argue that one of the important factors that limit the reliability of GPR in detecting burials is the soil condition of the survey site. We excavated soil just outside of the cemetery to determine the stratigraphy in the

immediate area and to collect soil samples. Soil samples were analyzed in the lab to determine the soil suitability for the GPR survey and to determine parameters for modeling. The parameters were used as inputs to the forward modeling of two burial types in the cemetery. We also excavated a pit, buried a concrete vaulted burial and a wooden coffin in it, and then surveyed with GPR to observe the burial shapes and detectability of the burial. The results from numerical modeling and template surveys provided us with expected signatures for the actual 3D GPR surveys over known and unmarked burials. The parameters were used as inputs to the forward modeling of two burial types in the cemetery. We also excavated a pit, buried a concrete vaulted burial and a wooden coffin in it, and then surveyed with GPR to observe the burial shapes and detectability of the burial. The results from numerical modeling and template surveys provided us with expected signatures for the actual 3D GPR surveys over known and unmarked burials.

Hansen et al. (2014) suggested the optimum frequency for detecting unmarked burials is between 200 to 400 MHz. In this work, we mostly used a 250 MHz GPR antenna system. We performed three velocity calibration techniques to assist with time-depth conversion. They included a common mid-point (CMP) survey, time-to-depth measurements, and hyperbola fitting. For calibration, we performed a 3D template survey over marked burials to identify anomalies at known burials. Burials after 1940 are particularly clear because of the reflections and diffractions from the soil-concrete interface and possibly from inside the vault.

We also used depth slices from the 3D GPR surveys as high amplitude indicators. We undertook a TLS survey to acquire the surface elevation tomography of the cemetery. Taking GPR depth slices overlain on the TLS elevation profile, and cemetery records helped to ascertain the location of these suspected unmarked graves. We performed six 3D GPR surveys to locate the unmarked burials. The results provided strong evidence of two unmarked burials including one that may belong to the oldest recorded burial of James West. We discuss the three critical surveys in this thesis.

3.2 Mueschke Cemetery

The Mueschke Cemetery is located approximately 21 miles north of downtown Houston, Texas (Figure 3.1). The burial ground is managed by the Mueschke Cemetery Association, comprised of descendants of those buried there. The site is fenced and covered with grass, trees, and some shrubs. The GPR suitability map (Figure 3.1) shows the majority of the study area is classified as having a moderate to high suitability index. The moderate index refers to the areas dominated by mineral soils with 18% to 35% clay and a high index with less than 18 % clay (USDA, 2009). High suitability soils with clay minerals less than 18 % or deep organic soils have a high potential for a successful GPR survey (Doolittle, et al., 2007). Historical documents and oral histories indicate that the cemetery is the resting place of veterans who served in the American Civil War, Spanish-American War, World War I, and World War II. There are at least 202 graves at the cemetery dating back to the 1870s (Flores, 2013).

A Mueschke Cemetery base map showing GPR surveys (Grids 1, 2, 3, Line A, and CMP, C) and our excavated pit location, T is shown in Figure 3.2.

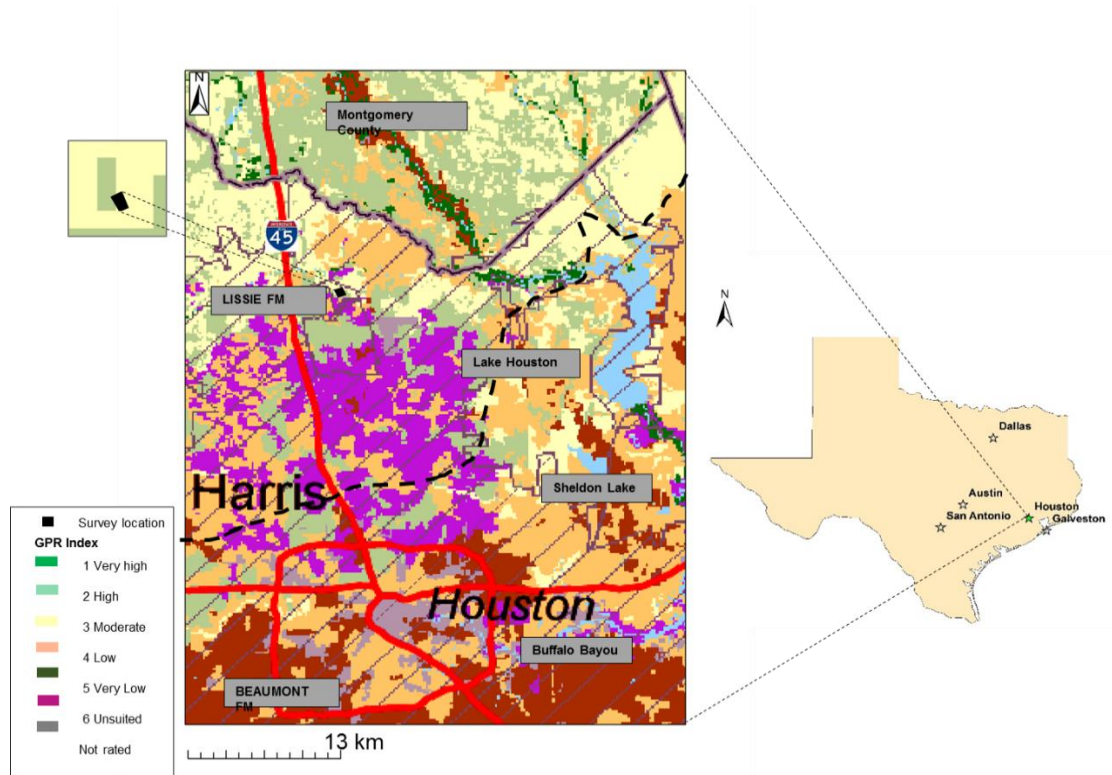


Figure 3.1. The survey location in northwest Houston and GPR suitability map and (USDA, 2009). The majority of the study area is classified as having a moderate to high suitability index. The black dash divides the Pleistocene Lissie (NW) and Beaumont Formation.

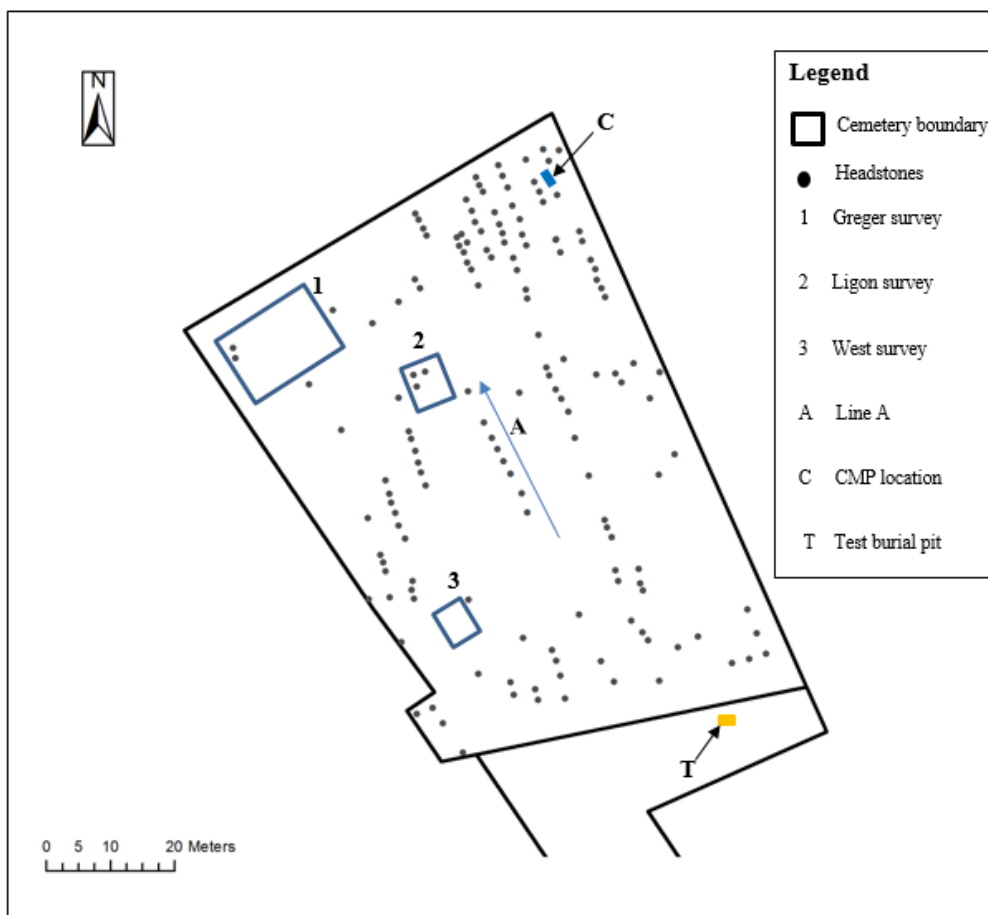


Figure 3.2. Mueschke Cemetery base map showing GPR surveys (Grids 1, 2, 3, Line A, and CMP, C) and our excavated test burial-pit location, T.

3.3 Geological description

The study area is located in an area of the Pleistocene Lissie Formation. The upper part of the Formation is mainly composed of reddish, orange, gray, and coarse-to-fine grain mixture of sand, silt, and clay. The surface is mainly flat and featureless except for some shallow depressions and pimple mounds (USGS, 2002). To study the stratigraphy, we excavated a burial-sized pit [1.8 m (length) x 1.2 (width) m x 1.5 m (depth)] just outside of the cemetery (Figure 3.3). Three major layers were identified based on the soil

features and colors: sandy loam (between the surface and at 0.7 m), sandy clay loam (between 0.7 and 1.1 m), and mostly clay (below 1.1 m). In the layer between 0.7 and 0.11 m, we observe the presence of orange materials which we interpreted as containing iron. The layers were interpreted to consist of Pleistocene Lissie formation (Figure 3.4a).

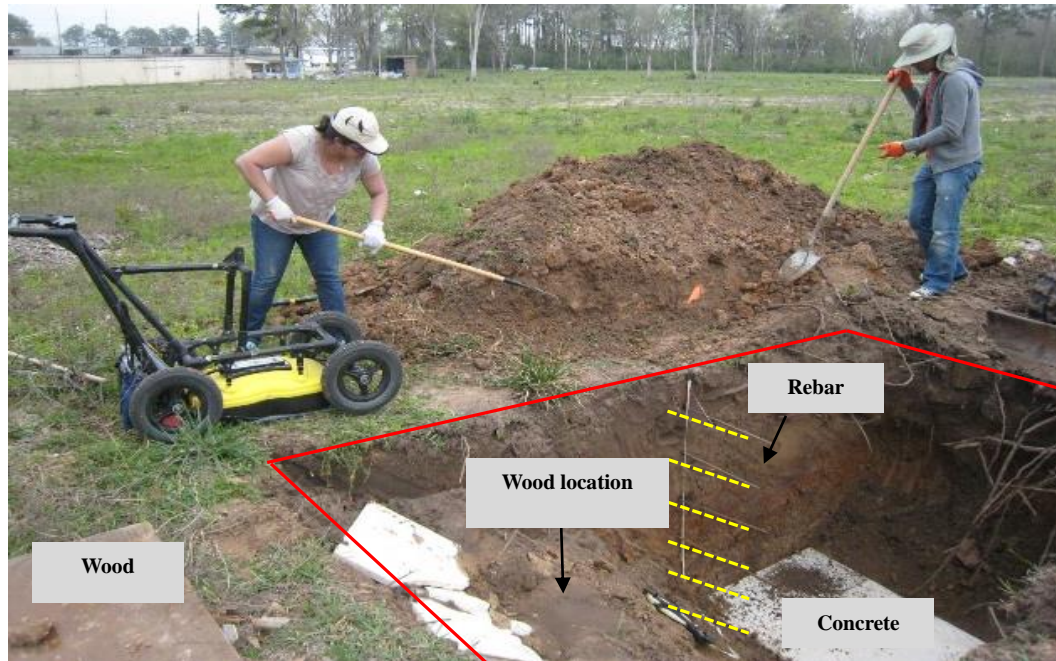


Figure 3.3. The red outline shows the parameter of the excavated pit (1.8 m x 1.2 m x 1.5 m). The yellow dotted lines mark the rebar's interval location. The rebar was used as a velocity calibration. A concrete was buried in the pit to simulate the concrete-vaulted burial. The wood in the photo was also buried to the left of the concrete.

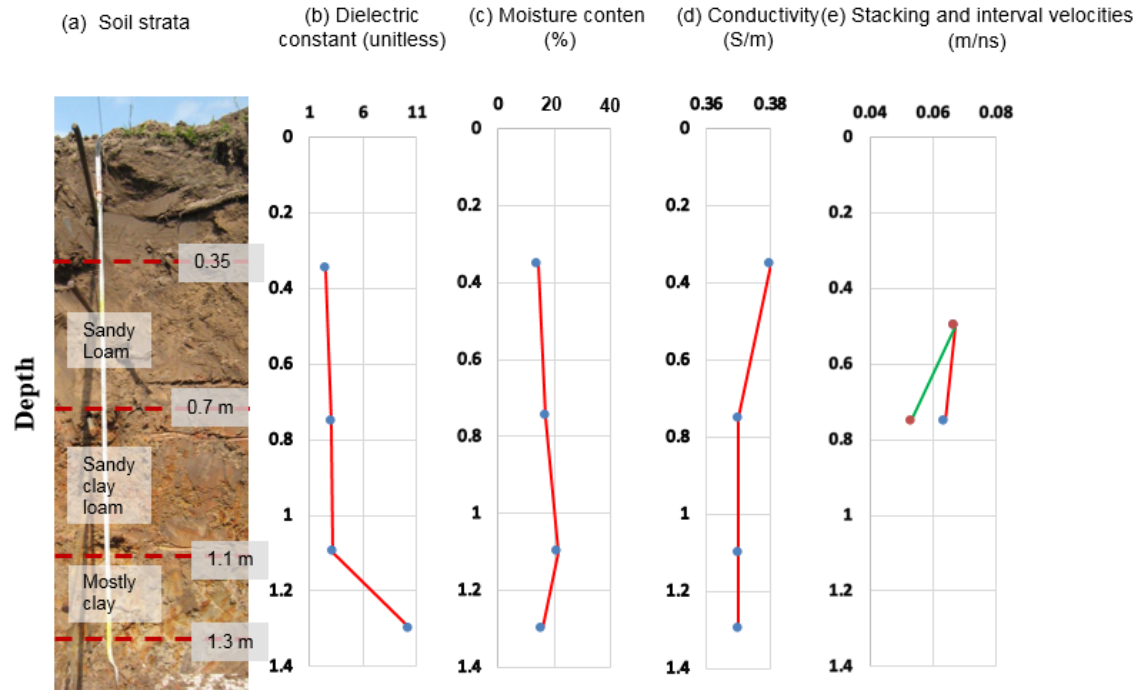


Figure 3.4. (a) Three major layers were identified based on the soil features: sandy loam (between the surface and at 0.7 m), sandy clay loam (between 0.7 and 1.1 m), and mostly clay (below 1.1 m). (b) Dielectric constant measurement of the four soil samples from Mueschke Cemetery. (c) Moisture content percentage measurement of the four soil samples. (d) Electrical conductivity measurement of the four soil samples. (e) Stacking velocity (Red line) and interval velocity (green line) versus depth.

3.4 Terrestrial laser scanning (TLS) survey

Oral histories also suggest some burials can be indicated by sunken depressions in the ground as a result of coffin collapses and backfilled soil naturally settles. We hypothesize the wooden burial is characterized by a depression but the concrete burial is identified by a surface mound (Figure 3.5).

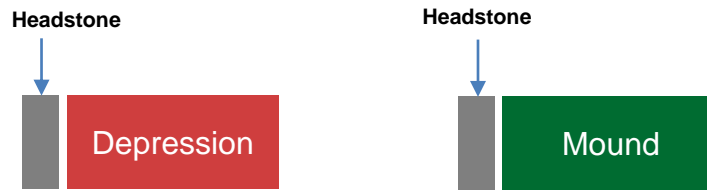


Figure 3.5. In plan-view: it is hypothesized that the wooden burial is characterized by a depression but the concrete burial is identified by a surface mound.

We use terrestrial laser scanning (TLS) as a reconnaissance method to try to detect surface depressions and mounds. We acquired TLS data at three locations using a survey-grade laser scanner, RIEGL VZ-400 to study the surface elevation profile (Figure 3.6). The three locations were chosen to cover the entire cemetery. The scanning from the three locations minimizes the shadow areas as they can only be observed from one location (D. Hauser, 2016, pers. comm.). The instrument can scan 360 degrees horizontally and 100 degrees vertically. It operates with a single and near-infrared laser. The instrument accuracy is 5 mm, and the measurement rate is 300 kHz (Hauser, 2013).

The data from the three scan locations were combined using a software called retro-reflectors. The software determines locations of the reflectors in each scan location, and then automatically registers all the three scans by using the geometry of the reflector positions in relation to each other. Then the GPS coordinates are applied to give the data global coordinates. The absolute vertical accuracy of the data is 1–2 cm which is as good as GPS data. The relative accuracy or the resolution is 5 mm with an error of a few millimeters horizontally and a few centimeters vertically after the data were stitched

together (D. Hauser, 2016, pers. comm.).

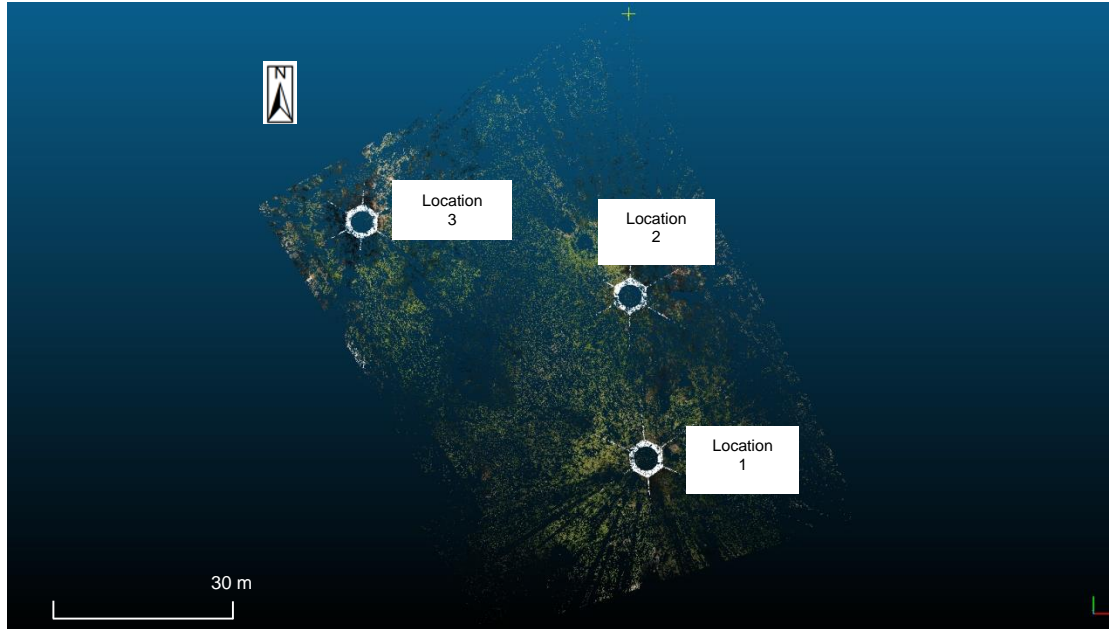


Figure 3.6. TLS picture taken at three locations (white hexagons) using a survey-grade laser scanner, RIEGL VZ-400 to study the surface elevation profile.

We extracted the Z coordinate (elevation) from a 15 million point cloud and filtered features above the ground to obtain the surface elevation profile. Then, we generated a raster image, followed by a geostatistical analysis (inverse distance weighting), and detrending. The details of the data processing can be found in the Appendix A-3. Figure 3.7 shows the surface elevation before detrending the data. By detrending the data, we obtain an image that enhances the surface depression and mounds as shown in Figure 3.8. The pixel size of the map is 22 cm by 22 cm. We can see some correlations of surface mounds on TLS image with known concrete burials (after 1940) as highlighted by red dashed circles. The high elevation can be due to the surface mounds from the unconsolidated soil over the concrete burials or the headstone residual. We also see surface mounds with no headstones on the map. We can also observe correlations of surface

depressions with known wooden burials (prior to 1940) as shown by the blue dashed circles. From the TLS map, 75 % of the TLS anomalies could be associated with known burials. It is a reasonable method that suggests where to focus on the investigation in more details with GPR. This leads to the specific investigation of these locations using GPR, which will be described in detail in the subsequent section.

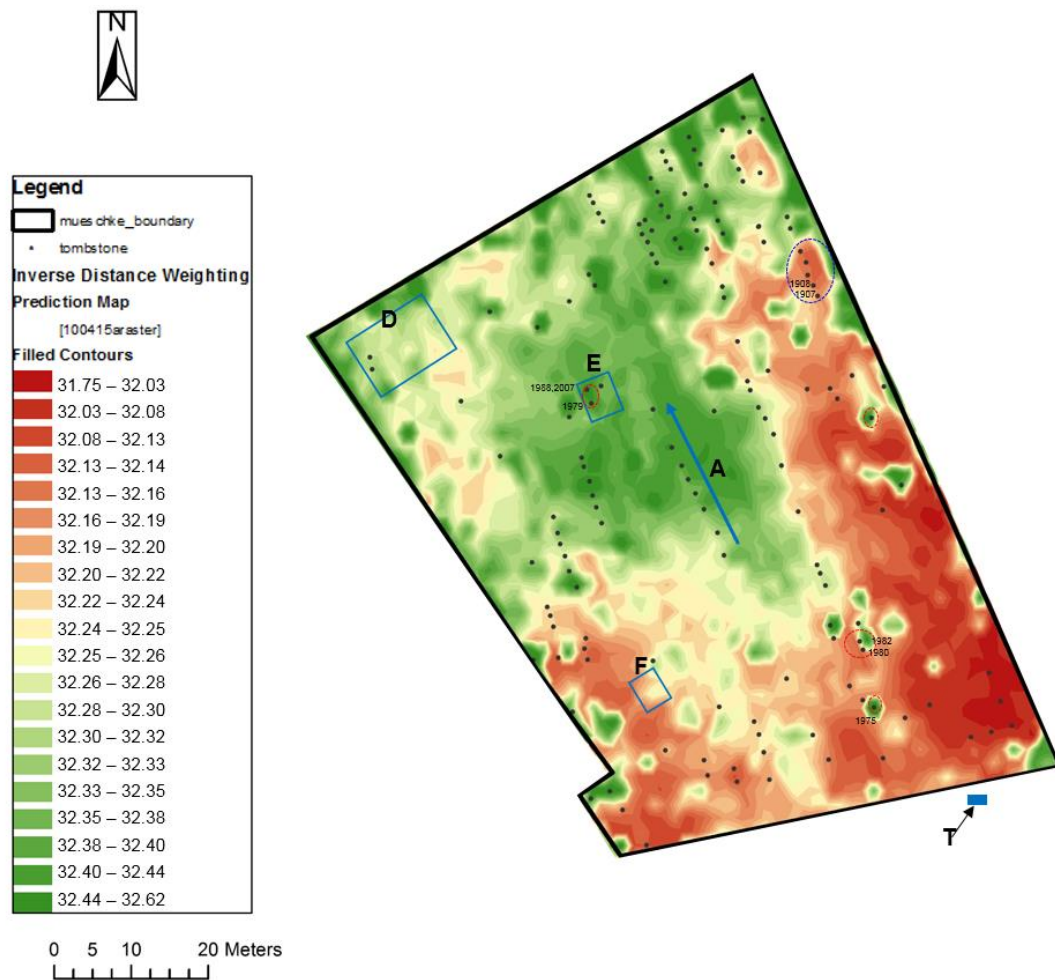


Figure 3.7. The surface elevation from terrestrial laser scanning (TLS) (after Inverse Distance Weighting) with headstones. The image shows the areas with depressions (red), some of which coincide with the known wooden burial locations as shown by blue dashed circles. The image also shows the areas with mounds (green), some of which coincide with the known concrete burial locations as shown by red dashed circles.

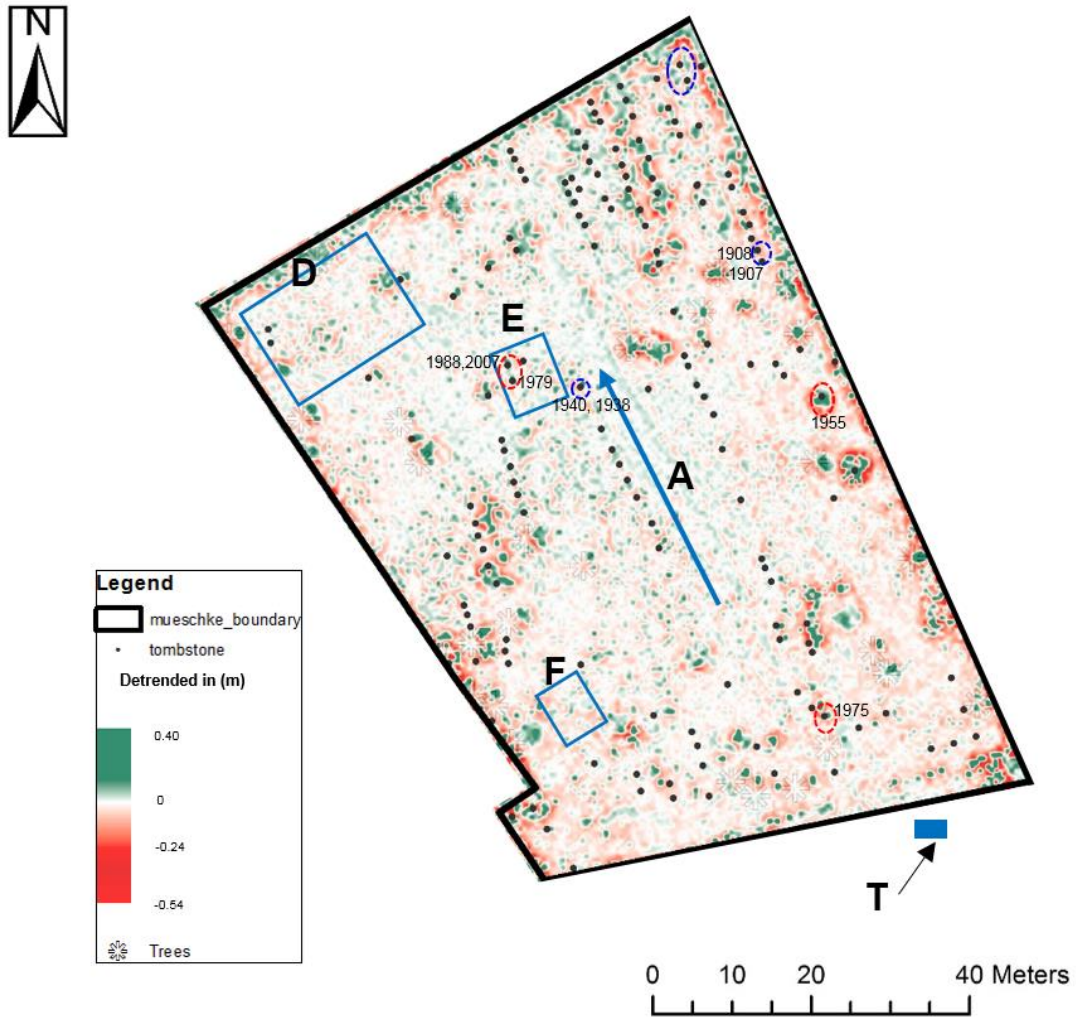


Figure 3.8. The surface elevation residual from terrestrial laser scanning (TLS) (after detrending) with headstones. There are some correlations of surface mounds on TLS image with known concrete burials (after 1940) as highlighted by red dashed circles. The image shows the areas with depressions (red), some of which coincide with the known burial locations as shown by blue dashed circles.

3.5 Soil physical properties

Soil samples were collected at four depth intervals (0.35 m, 0.75 m, 1.1 m, and 1.3 m) from the same pit for dielectric constant, moisture content, and conductivity measurements as described in section 3.3 (Figure 3.9). We used a laser diffraction particle size analyzer

to measure the percentage of grain size of the soil samples. The percentage of the grain size of the four soil samples is illustrated in Figure 3.10. Silts are dominant in all four samples. The highest percentage of clay is 12. This soil study on the clay percentage agrees with the more general area in the GPR soil suitability map which indicates the GPR appropriateness in the area.



Figure 3.9. Four soil samples (from depths of 0.35 m, 0.75 m, 1.1 m, and 1.3 m) from Mueschke Cemetery used for the dielectric constant, moisture content, and conductivity experiments.

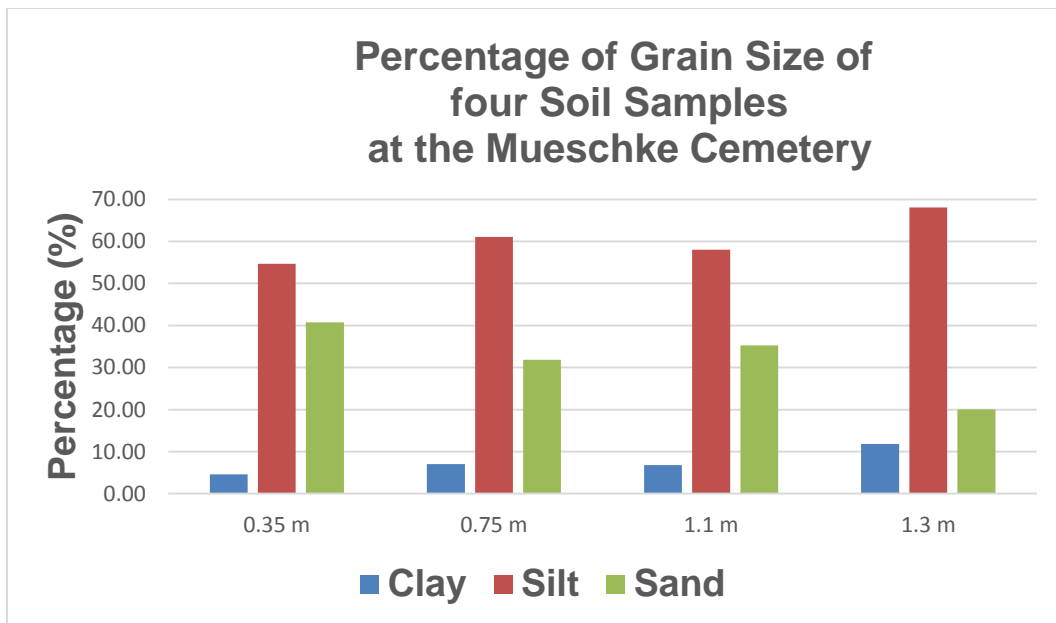


Figure 3.10. The percentage of the grain size of four soil samples at the indicated depths.

We measured the dielectric constant and the conductivity by placing a soil sample in a brass disk that acts as a sample holder. The sample holder, which is modeled as a π network, is then connected to a Radio Frequency (RF) Impedance Analyzer controlled by the LabView program. The measurements were taken at frequencies of 100 and 250 MHz.

The experimental result indicates that the bulk dielectric constant at 250 MHz is lower than that of 100 MHz (Figure 3.11). This trend is consistent with the data presented by Cihlar and Ulaby (1974).

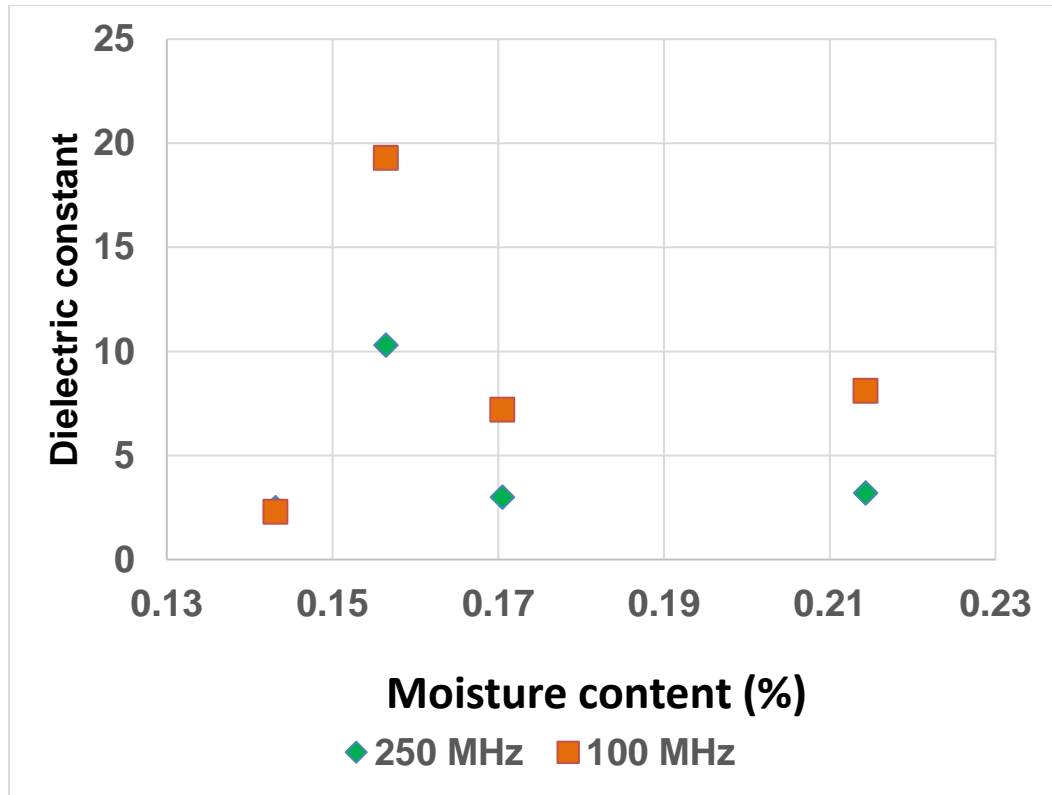


Figure 3.11. The dielectric constant of four soil samples (from depths of 0.35 m, 0.75 m, 1.1 m, and 1.3 m) measured at frequencies of 100 and 250 MHz as a function of moisture content.

We observed the dielectric constant measured at 250 MHz increases as the depth increases (from 2.5 to 10.31) (Figure 3.4b). This suggested an increase in the soil moisture content as depth increases except for the deepest sample at 1.3 m (Cihlar and Ulaby, 1974). The dielectric constant value is used to calculate the reflection coefficient and to model the burial using computer simulations.

Moisture content was measured through a laboratory experiment by measuring the weight of the sample before and after being heated (60 °C) in a vacuum oven for 12 hours. The

difference in initial weight and weight after heating is the moisture loss. To calculate moisture content (%) the formula below is used:

$$\text{Percentage of moisture content} = (\text{initial weight of sample} - \text{weight of sample after heating}) / \text{initial weight of sample} \times 100$$

We observed the moisture content increases as the depth increases up to 1.1 m and then decreases at greater depth (Figure 3.4c). The electrical conductivity of the four samples is highest for the shallowest sample at 0.35 m but then decreases and is consistent for the 3 deeper samples (Figure 3.4d). The electrical conductivity is comparable with the value reported by the Texas A & M AgriLife Research Soil Characterization Lab for the same description of soil type which is 0.3 S/m.

The behavior of moisture content versus depth curve is consistent with the water capacity of the textural class soil. For example, sandy loam minimum water-capacity is 1.25 inches/foot of depth while sandy clay loam is 1.50 inches/foot of depth and clay is 1.20 inches/foot depth. We observed a linear relationship between the moisture content and the dielectric constant from the samples at 0.3 m, 0.75 m and 1.1 m (Figure 3.4c). This is consistent with previous work by Cihlar and Ulaby (1974). However, the sample at 1.3 m shows did not obey the linear relationship rule.

3.6 GPR numerical modeling

We used 2D finite-difference time domain (FDTD) to simulate the full wavefield GPR responses. The synthetic models were built to help us to understand the effect of the attenuation of the received signal attributed to the soil type and moisture content, and to identify GPR signature of the different type of burials. We used MATGPR simulation to perform the forward model (Tzanis, 2006).

Figure 3.12a shows the numerical model of one concrete burial and two wooden burials with the soil parameter assigned based on the soil studies results. Figure 3.12b shows the simulation result of a GPR profile in dry clay soil for the model in Figure 3.12a. The reflection from the top of the concrete burial has a rectangular shape when compared to the wooden burials. The rectangular shape reflection is consistent with the hyperbolas observed in the survey template (Ligon survey). The reflectors observed underneath of the burial tops are the multiples from the simulation.

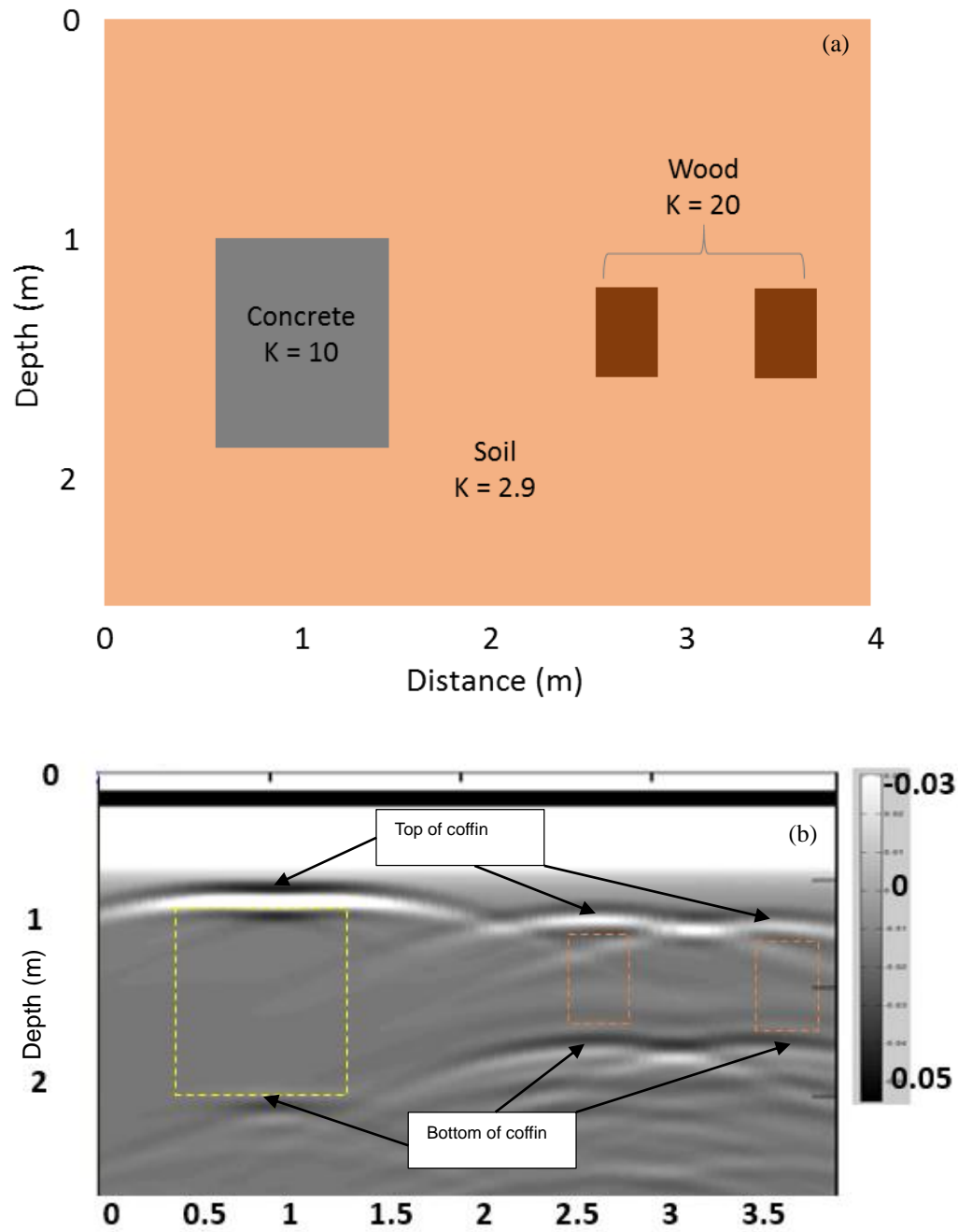


Figure 3.12. (a) Modeling of one concrete burial (yellow rectangle) and two wooden burials (orange rectangle) in soil. (b) The hyperbola from the concrete burial has a rectangular shape top while wooden burials have a regular hyperbola shape.

3.7 2D GPR templates

The GPR acquisition surveys started in October 2013 and ended in March 2014. Table 3.1 summarizes the date, survey name, the area covered, and the time spent at the Mueschke Cemetery.

Table 3.1 Summary of the GPR survey at the Mueschke Cemetery

Date	Survey	Area of grid	Time spent
10/20/2013	Reconnaissance survey	N/A	4 hours
11/08/2013	Ligon survey	5 m x 12 m	4 hours
11/08/2013	Taylor survey	3.5 x 9.5 m	2 hours
11/16/2013	Tautenhahn survey	5 m x 5 m	4 hours
11/29/2013	Wheeler survey	12 m x 14 m	3.5 hours
02/23/2014	West survey	7 m x 7 m	5 hours
03/08/2014	Poland survey and CMP	15 m x 1.5 m	4.5 hours
03/22/2014	Excavation and burying test burials	N/A	12 hours
03/29/2014	Test burial survey	5 m x 5 m	4 hours
04/16/2016	Placing the marker on the unmarked burial	N/A	4 hours

We collected a GPR line (Line A in Figure 3.2) over the top of burials dated from 1936 to 2009 to observe GPR signatures using the Noggin Plus SmartCart 250 MHz antenna (Figure 3.13). Green arrows indicate concrete burials while yellow arrows mark wooden burials. The diffractions of burials between 1963 and 1964 are distinct and have cone-like shape. This suggests that two types of vaults that are different shape were used between 1963 and 2009. This observation and interpretation were verified by an interview with Mrs. Rebecca Stone of the Mueschke Cemetery Association. Burials

between 1938 and 1943 were not easily identified in the GPR profile suggesting wooden coffins were used. The contrast in the soil around $x = 17$ m suggests a burial prospect because the body or the coffin may have chemically changed the surrounding soil. The break in the soil horizon also suggests a burial is present. A strong horizontal reflector is observed at 0.8 m, and it is interpreted as a boundary where loam changes to clay which correlates with the excavation result in Figure 3.4a.



Figure 3.13. A photograph showing a University of Houston team member (Mr. Marcus Zinecker, with Lone Star's Ms. Janet Flores) pushing the Noggin Plus SmartCart 250 MHz antenna. The photograph also shows headstones in the Mueschke Cemetery.

We observed that the burials between 1989 and 2009 had planar and strong diffractions from the sides (Figure 3.14). The planar reflections suggest the coffins were enclosed in flat top concrete vaults. The high amplitude reflections may be due to the void space between the soil and vault and/or the vault and the coffin. Coffins that did not collapse will have spaces between the lid and the bottom. Energy passing through void spaces will increase in velocity and produce a velocity pull up which can distort the reflections

underneath it (Conyers, 2004). We observed a velocity pull up underneath the top reflection of Buster Pennington's burial (RIP: 1964). Amos Pennington's (RIP: 2005) burial showed a distinct reflection from its top and bottom (one reflection is from the top of the coffin and the void space, and the other is from the void space and the bottom of the coffin). Two burials, Buster Pennington (RIP: 1964) and Clyde Pennington, (RIP: 1963), have similar diffraction shapes that are different from the other vaulted burials.

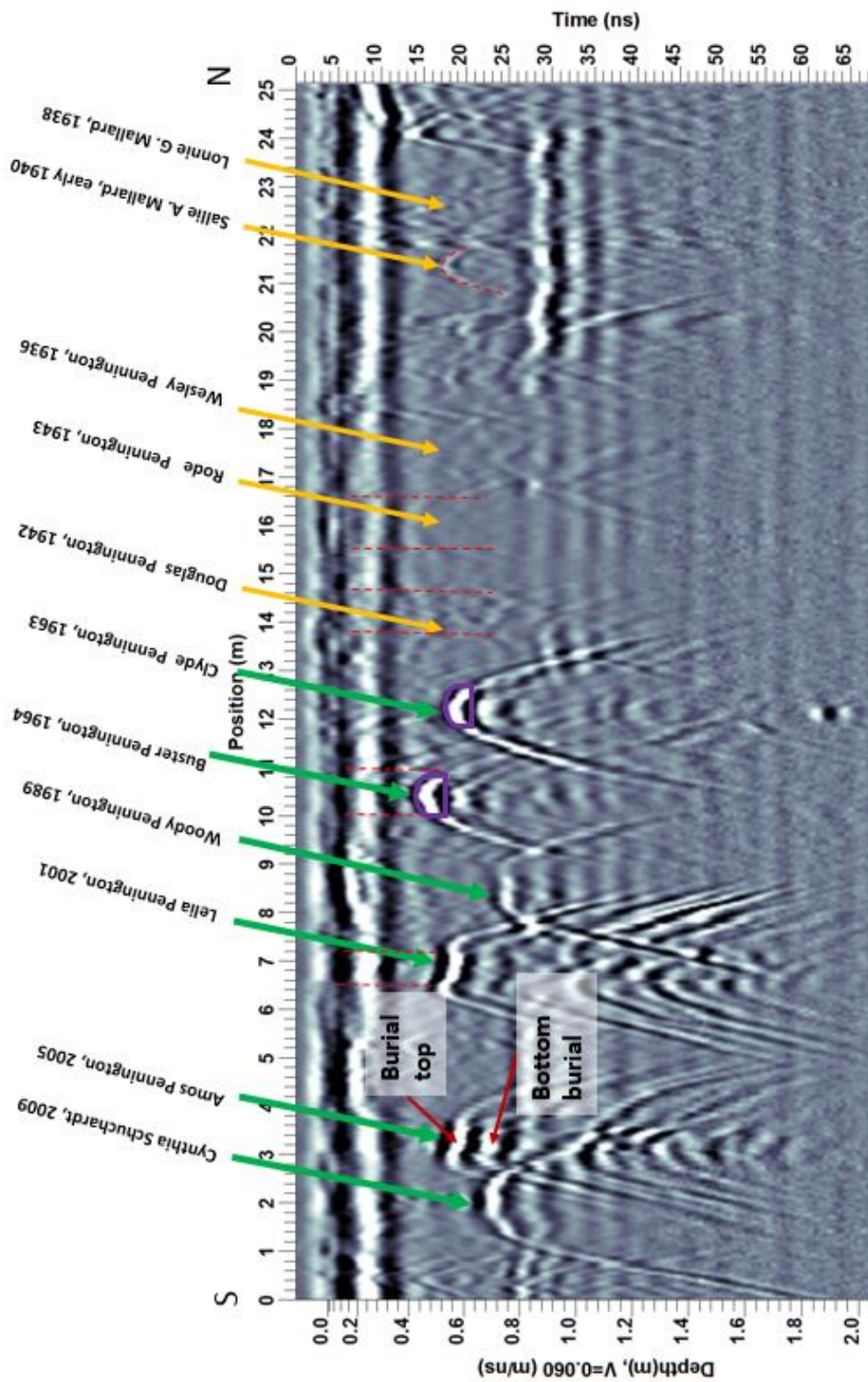


Figure 3.14. GPR profile of Line A shows burials between 1989 and 2009 are characterized by planar and strong diffractions similar to the numerical modeling results. Green arrows indicate concrete burials while yellow arrows mark wooden burials

We did not observe a diffraction for Douglas Pennington (RIP: 1942), Rode Pennington (RIP: 1943), Wesley Pennington (RIP: 1936), and Lonnie Mallard (RIP: 1938). Human remains and wooden coffins tend to decompose and weather greatly in a humid area (Conyers, 2004). It is challenging to detect coffins that have collapsed and human remains that have decomposed in historic cemeteries. One indicator can be the settling of the surface soils above the coffin as it collapses. We observed fuzzy areas around Rode and Wesley Pennington's burials which implied that the burials are different from the surrounding soil. The other indicator of human burial presence is if the incision from the vertical shaft cut to dig the grave was visible on the GPR radargram. A vertical shaft is cut through a homogenized soil, and then the soil is later used as backfill. We also observed the discontinuity of the reflector above the diffractions, which suggested disturbed soil for the vertical shaft. We can use this observation to locate the suspected burials which have no or weak diffractions. We observed this discontinuity pattern in Douglas and Rode Pennington's burials as seen by the red dashed lines.

According to the Mueschke Cemetery Association personnel, burials were required to be encased in concrete after 1940 to avoid collapse and to be washed away during flooding. Most of the burial tops are at depths between 0.5 m to 0.7 m. This is consistent with the depth of burials found in some other studies (Neiman; 1980; Westwood-Turowski and King; 1991; Doepkens; 1991; King et al., 1993)). The GPR profile showed very distinct diffractions and most have the rectangular shape top just like as is seen in the forward modeling, Figure 3.12b. The burials before 1940 are shown by the yellow arrows, and the

GPR response was weak. This result is important for detecting potential burials.

We also simulated a recent burial by burying concrete blocks and slabs measuring 1.5 m x 0.9 m x 0.4 m that contained an interior void space. We also buried a 1.2 m x 0.4 m x 0.02 m wood plank to represent a wooden coffin burial. The top of both burials is at 0.96 m from the surface. Figure 3.15 shows an unmigrated radargram of a survey line over the two burials. There is a reflection which is suspected coming from the void in the concrete burial as shown by the yellow dashed rectangle. The reflection from the concrete burial did not show a horizontal shape of the top of the enclosure. According to Bevan (1991), the observed patterns may be due to the difference in the velocity of the buried soil and the subsoil scattered on the surface. The wooden burial is suggested by a small reflection marked by the blue dashed rectangle. There is a clear delineation (marked with red arrows on each end of the radargram) at about 1 m to divide between the disturbed/fresh soil that was used to bury the concrete burial and the compacted soil. The green hyperbolas are interpreted as tree roots.

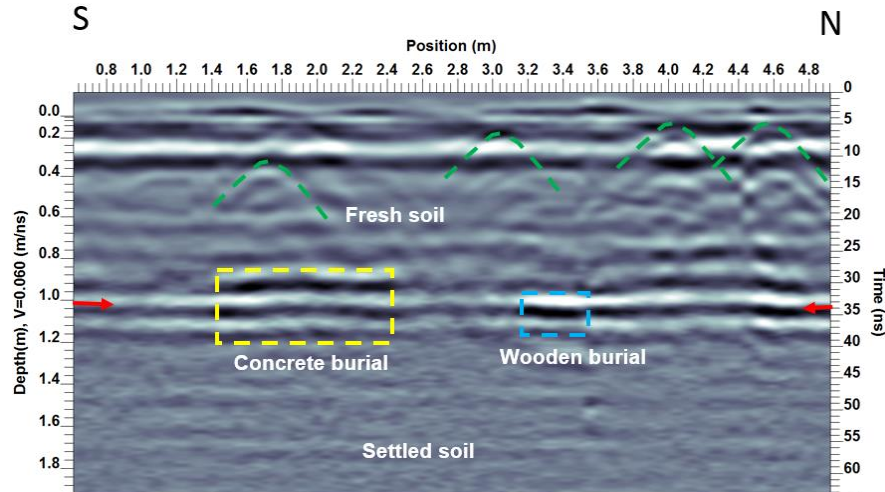


Figure 3.15. (a) GPR section showing a 2D profile of the concrete and wooden burials in the excavated pit. Yellow and blue dashed rectangles outline the concrete burial and the wooden burial, respectively. Red arrows indicate the transition area between the disturbed/fresh soil that was used to bury the concrete and the compacted soil.

3.8 Velocity estimation

A velocity is required to convert two-way travel times to depth. An accurate method of velocity calibration is to bury rebar at known depths and perform a GPR profile over them (Conyers, 2004; Schultz, 2007). This calibration was undertaken using the 250 MHz antenna over six buried rebar with a dimension of 1.25 m long and 1 cm diameter at an interval of 0.25 m running from a depth of 1.50 m to the surface. Velocities from rebar at 0.5 m and 0.75 m yield 0.067 m/ns and 0.064 m/ns respectively (Figure 3.16). The interval velocity calculated using the Dix equation yields 0.053 m/ns between 0.5 m and 0.75 m depth interval.

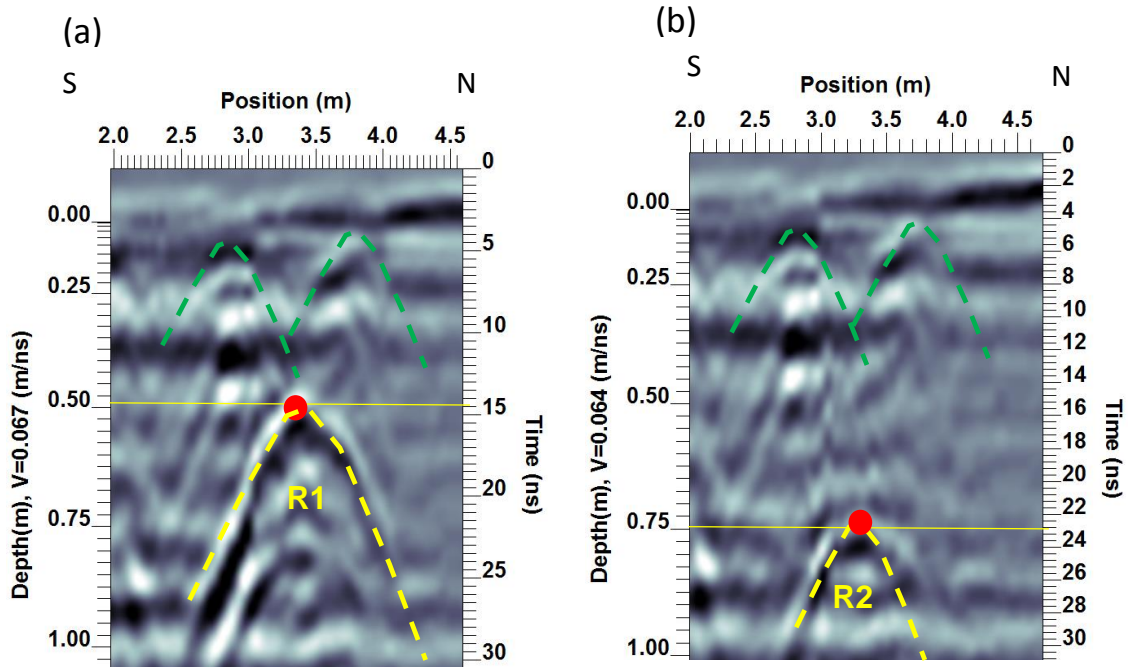


Figure 3.16. (a) Hyperbola matching over the diffraction of rebar (R1) buried at a depth of 0.50 m yields 0.067 m/ns. (b) The velocity obtained from the hyperbola matching over the diffraction of rebar (R2) is 0.064 m/ns. The green hyperbolas mark tree roots in the area.

To verify the velocity estimated from the excavation, we also performed common-midpoint (CMP) using PulseEKKO PRO 100 MHz system in the northeast of the cemetery as shown in Figure 3.2. The transmitter and the receiver antennas are moved across known burials (target) at a fixed offset (20 cm). The semblance analysis (Figure 3.17) shows a velocity range between 0.055 to 0.067m/ns which correspond to the velocity of a mixture of sand and clay. The velocity obtained from the CMP agrees with velocities measured from the calibration with the rebar.

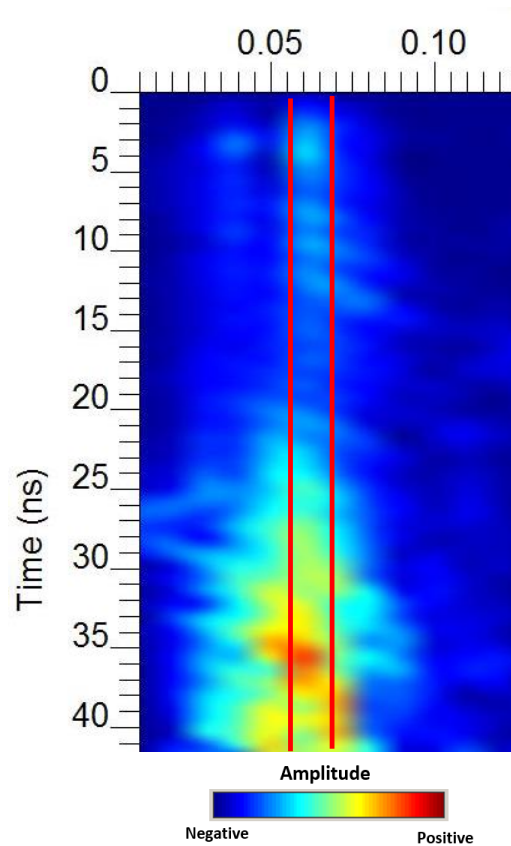


Figure 3.17. Velocity semblance from a CMP survey using 100 MHz antenna at the cemetery results in a range of velocity between 0.055 to 0.067 m/ns.

We also estimated the GPR velocity using hyperbola matching method and from the literature. The hyperbola matching technique from the radargram of concrete and wooden burials survey profile gave a velocity of 0.083 m/ns. The velocity is higher from the CMP, and this may be attributed to: (1) the two measurements were undertaken at two different times and separate places, hence the soil properties are not the same, (2) the CMP was performed when the soil was more saturated from the recent rain (~ 1 inch). The velocity decreased by 26 %, and this value is comparable to the value reported by Algeo (2012). In

their study, they observed a decrease of 13 % in the velocity after 0.45 inches of rain.

3.9 3D-GPR templates surveys

Between the winter of 2013 and summer 2014, six 3D-grids were acquired using Sensors & Software's Noggin Plus SmartCart 250 MHz antenna with an inline and crossline spacing of 25 cm. The weather conditions were dry during the GPR reflection surveys. We employed the technique of using a template survey to observe the GPR signatures of known burials. The Ligon survey was used as a template because there are three known concrete burials which were expected to give a strong diffraction in the radargram.

The acquired GPR data were excellent, and the penetration depth was approximately 2.5 m. The Ligon survey data were processed using dewow, background removal and spherical and exponential gain, and 2D-migration. The processed data show three diagnostic burial reflections, labeled A, B, and C in Figure 3.18, which indicate the top of the concrete coffins. Figure 3.18 shows the 2D reflection profile of the Ligon survey representing one transect to the east of two headstones, marking three known concrete burials (Nelson, RIP: 1979 (A), Ernest, RIP: 1988 (B) and Elsie, RIP: 2007(C)). Ernest and Elsie's headstone was a companion headstone. This profile was perpendicular to the long axis of the grave. The burial reflection tops are recorded at different depths due to the varying burial time. Deeper burial is related to earlier burial.

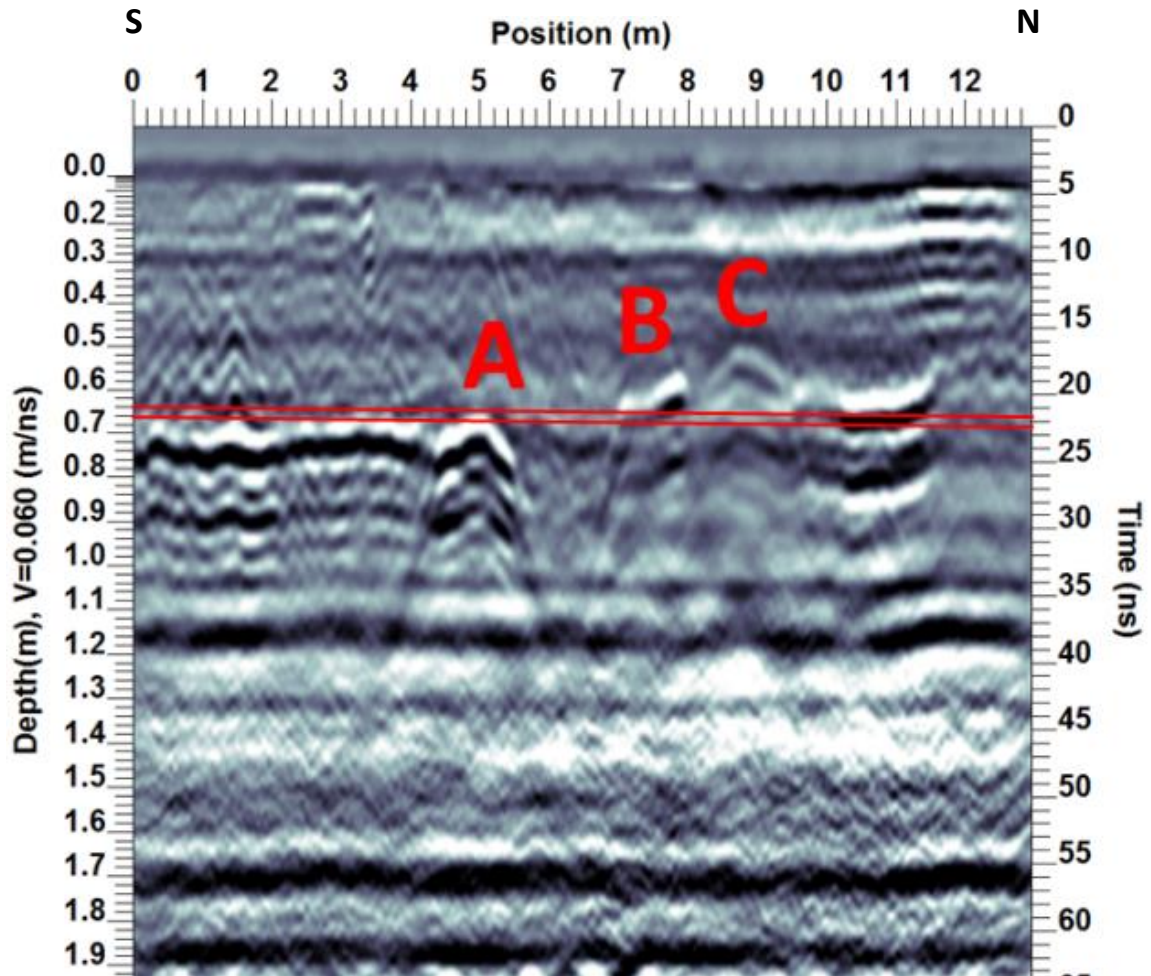


Figure 3.18. Migrated GPR section showing burials of Nelson (RIP: 1979) (A), Ernest (RIP: 1988) (B), and Elsie (RIP: 2007) (C) Ligon marked by the strong reflections.

We analyzed the depth slice data to identify the bright flat spot. Figure 3.19a shows the amplitude depth slice at 0.57 m corresponding to burial B and C which are marked by the rectangular box on the slice. Figure 3.19b indicates burial A and B at 0.65 m.

In Figure 3.19b, the high amplitude area on the top right corner of the slice is interpreted as the zone where the sand transitions to a higher clay content. The continuity of the clay layer can be observed in the GPR cross sections as seen in Figure 3.20 and Figure 3.21. A horizontal continuous interface is detected at a depth of 0.75 m suggesting a change of lithology. The result from the excavation shows a change from sandy clay loam to mostly clay at a depth of 1.1 m (Figure 3.4a). We used this template to identify unmarked burials in other surveys.

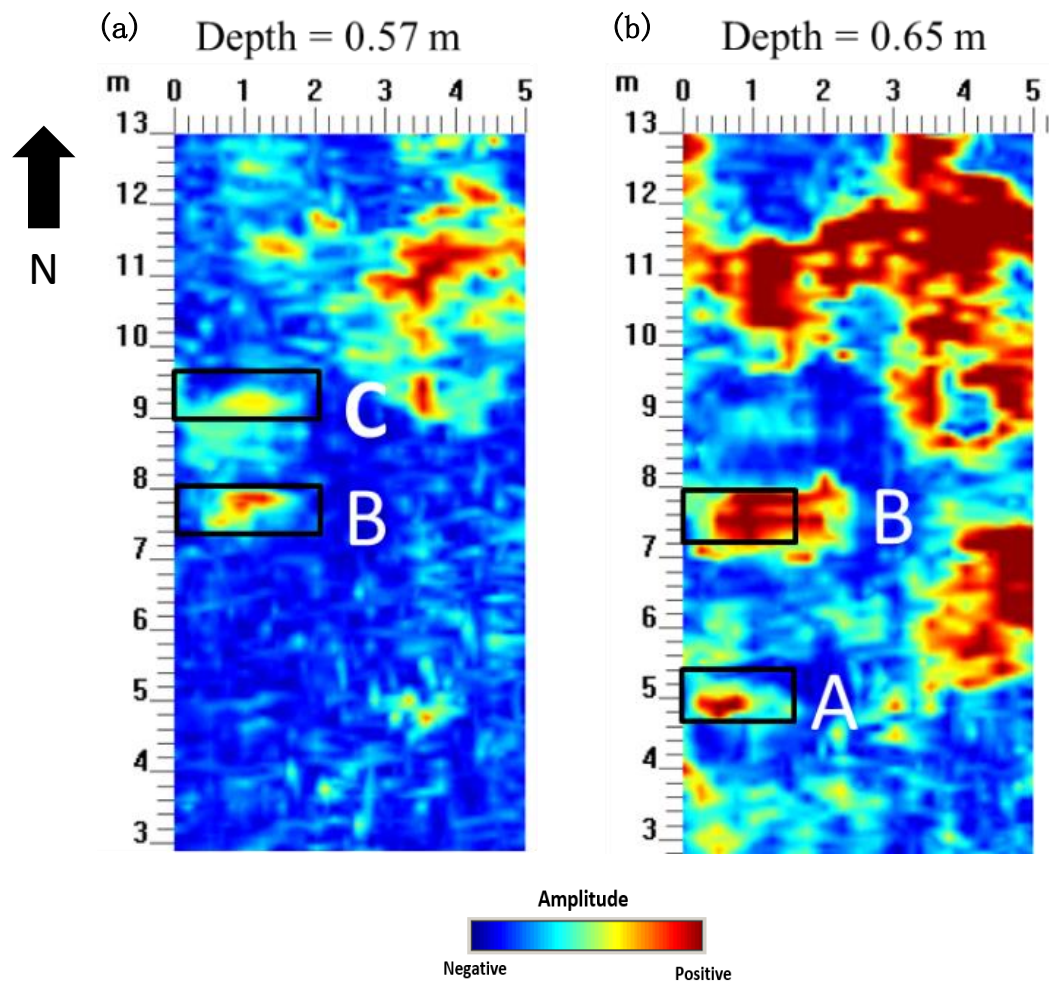


Figure 3.19. GPR depth slice at 0.57 m indicates the top of burial B and C seen by the high amplitude areas in the rectangular box. The high amplitude anomaly in the top right corner is interpreted as clay. (b) GPR depth slice at 0.65 m indicates the top of burial A and below the top of burial B seen by the high amplitude areas in the rectangular box.

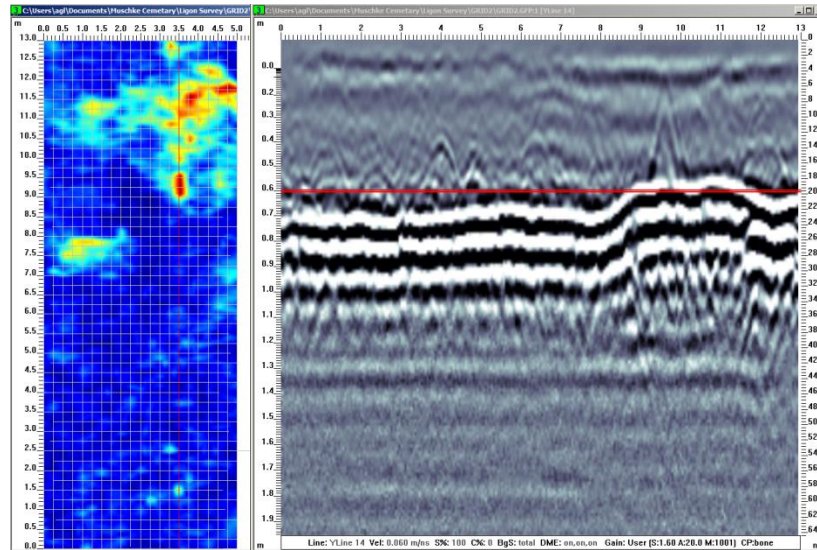


Figure 3.20. GPR depth slice at 0.6 m shows the high amplitude anomaly in the top right corner is interpreted as clay. The corresponding GPR section indicates continuity of the reflector and this verifies the high amplitude anomaly is interpreted as clay layer.

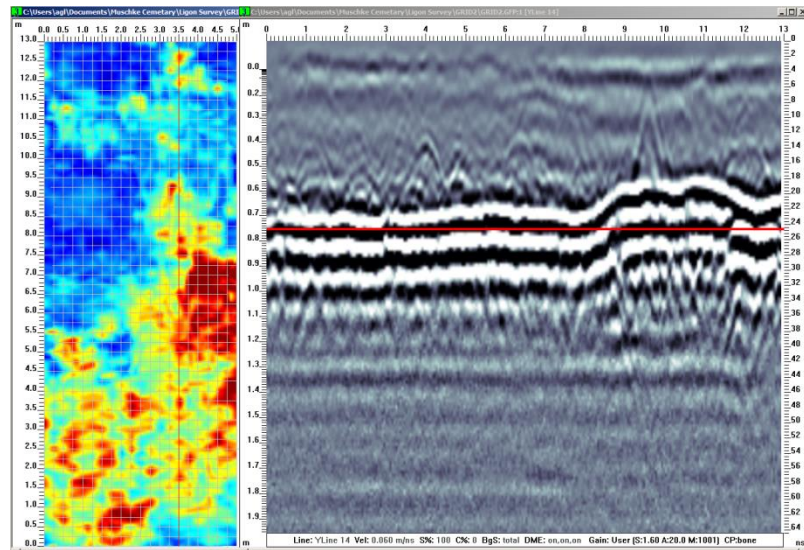


Figure 3.21. GPR depth slice at 0.75 m shows the high amplitude anomaly in the bottom half of the survey grid is interpreted as clay. The corresponding GPR section indicates continuity of the reflector and this verifies the high-amplitude anomaly is interpreted as clay layer.

We overlaid the GPR depth slice on the detrended TLS elevation profile to look for surface mounds or depressions over the burials. Figure 3.21 marks two areas of surface depressions that correspond to the burial A and B, in Figure 3.19b.

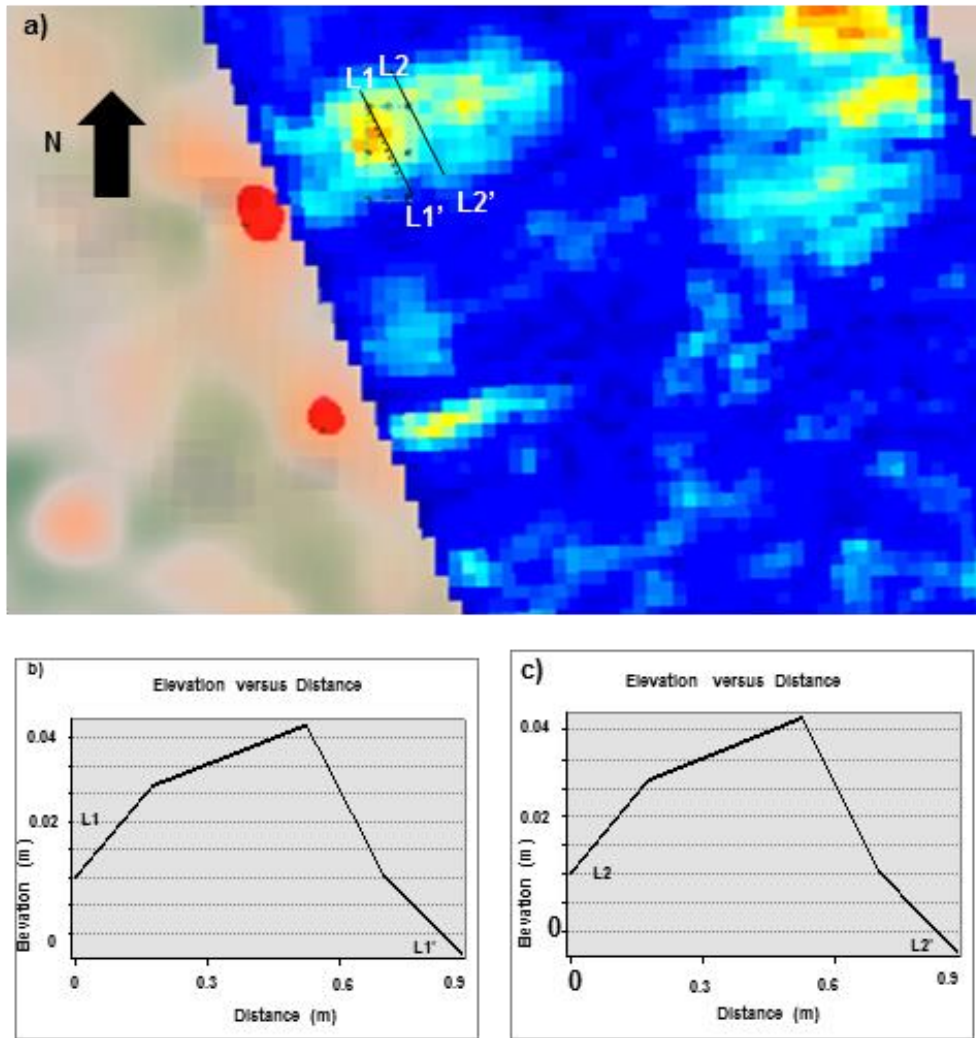


Figure 3.22. (a) GPR depth slice map overlain on the detrended TLS elevation profile to look for the surface mounds or depression of the burials. Two black lines are the investigation section. (b) The graph of L1-L1' shows a mound over the known concrete burial correspond to the burial C in Figure 3.19a. (c) The graph of L2-L2' shows a mound over the known concrete curial correspond to the burial B in Figure 3.18a.

3.10 Survey results

The data processing was undertaken using Sensors & Software processing package EKKOView Deluxe. The main steps in the standard data processing are time-zero correction, dewow, gain, background removal, and migration (Ulriksen, 1982; La Fleeche et al., 1991; Fisher et al., 1992; Fisher et al., 1996). We also produced depth slices to observe the reflected energy.

Figure 3.23 shows a 2D profile from the Greger survey where we are searching for the unmarked burial of James Culven Poland (Born: 1914; RIP: 1926). It was estimated that James Culven Poland was buried approximately 12 meters from two headstones located on the east side of the survey grid. Figure 3.24 displays a depth slice from the Greger survey. We observed a high amplitude area, labeled A, corresponding to the suspected a burial at 0.42 m depth.

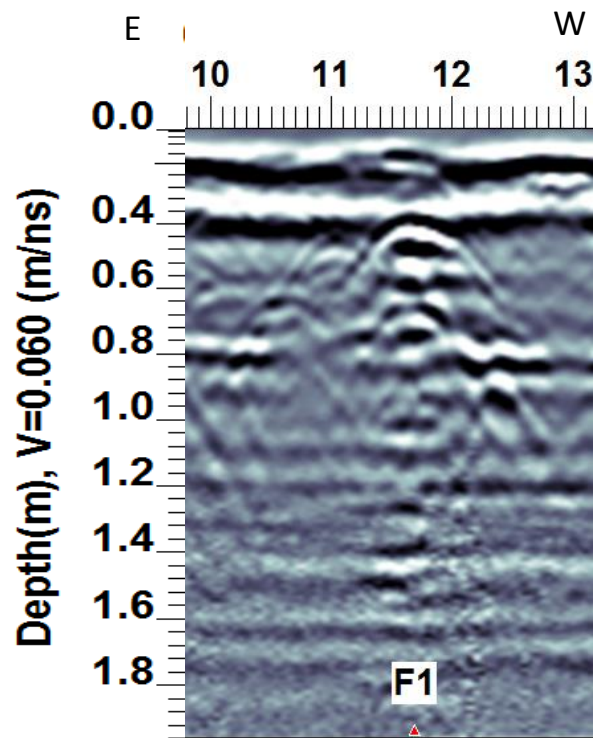


Figure 3.23. GPR section showing a 2D profile of the Greger survey where we are searching for the unmarked burial of James Culven Poland. A strong GPR reflection is observed between 11 m and 12 m. A fiducial marker F1 was made during the survey to mark the suspected location of the burial.

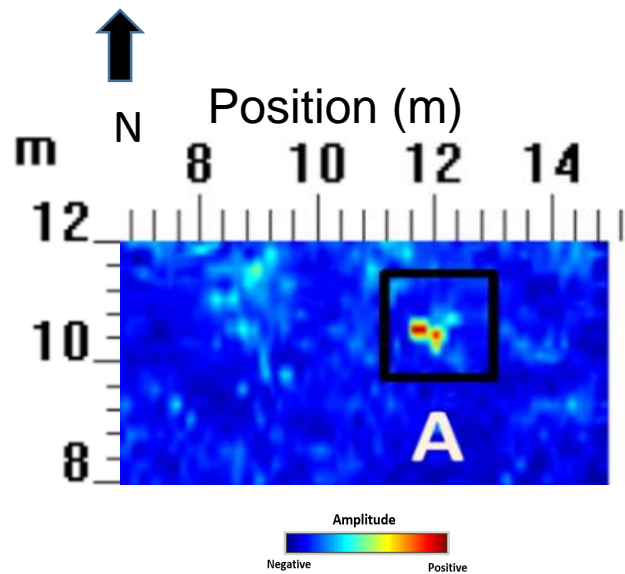


Figure 3.24. Depth slice shows the high amplitude area A corresponding to the suspected wooden burial at 0.42 m deep.

We overlaid GPR depth slice map on the TLS elevation profile to look for surface depressions of the unmarked burials (Figure 3.25). The image shows an area of surface depression, A, which corresponds to the burial A in Figure 3.23 and Figure 3.24. The Mueschke Association had placed a marker at the location suggested by the geophysical evidence found from this investigation (Figure 3.26).

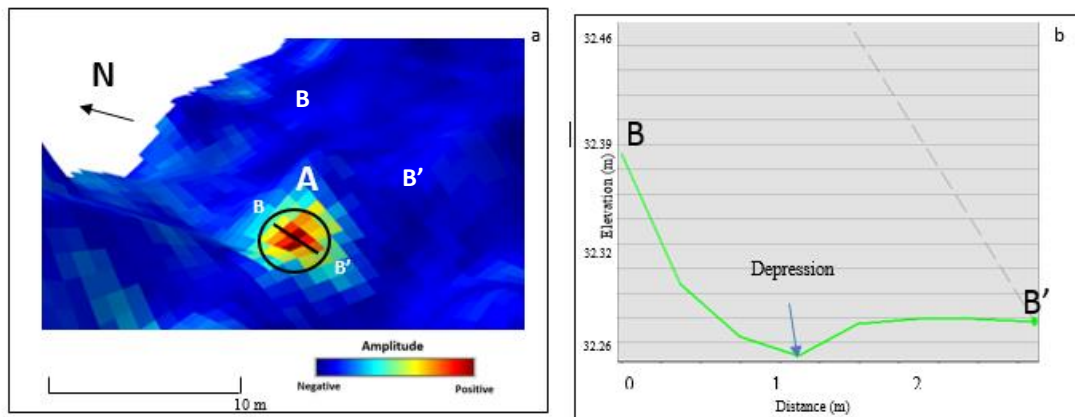


Figure 3.25. (a) GPR depth slice map overlain on the exaggerated TLS elevation profile to look for surface depressions of the unmarked burials. The image shows an area of surface depression, A, which corresponds to the burial A in Figure 3.20 and Figure 3.21 Figure (b) Line B-B' shows the surface depression corresponds to the high amplitude area of A.



Figure 3.26. A marker was placed at the location based on the result from the geophysical investigation.

Finally, the West Survey's goal was to locate the unmarked grave of James R. West. This grave is recognized as the oldest burial in the cemetery, dated 1875 in the Mueschke Cemetery records. The estimated location of the James R. West's grave is about 1.5 m south of the adjacent burial (Eliza West) (Figure 3.27).

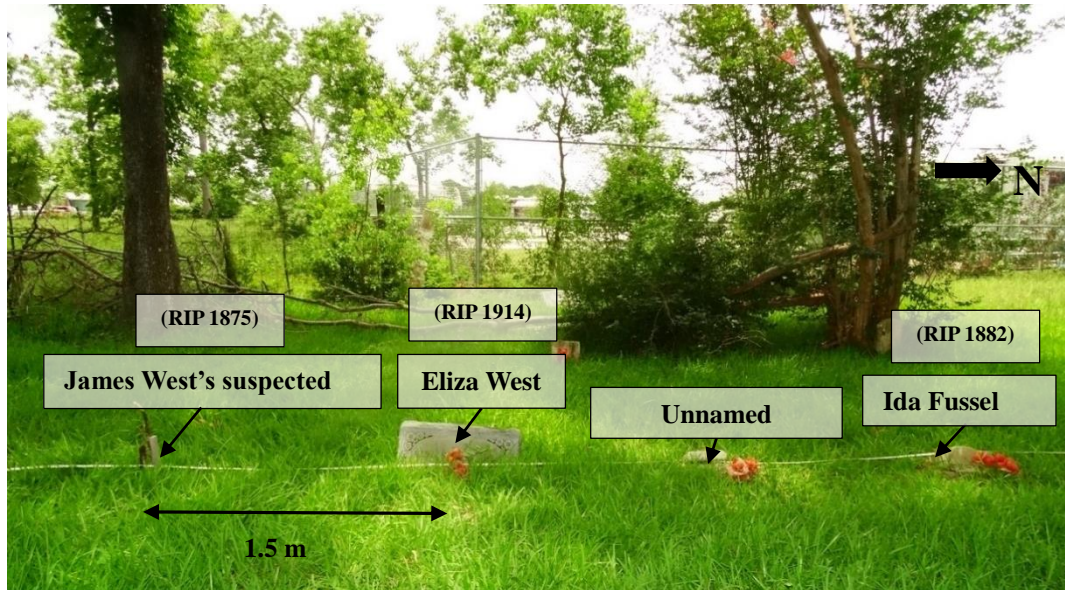


Figure 3.27. A photograph showing the estimated location of James West's burial which 1.5 m south of Eliza West's burial place.

Figure 3.28 and Figure 3.29 show the unmigrated GPR profiles from two adjacent lines with two diffractions from known burials, labeled E for Eliza West and F for an unnamed headstone. A third diffraction, labeled D, is suspected to be the burial of James West from the archaeological record. Figure 3.30 shows the migrated GPR profile to indicate the suspected location of the burial of James West.

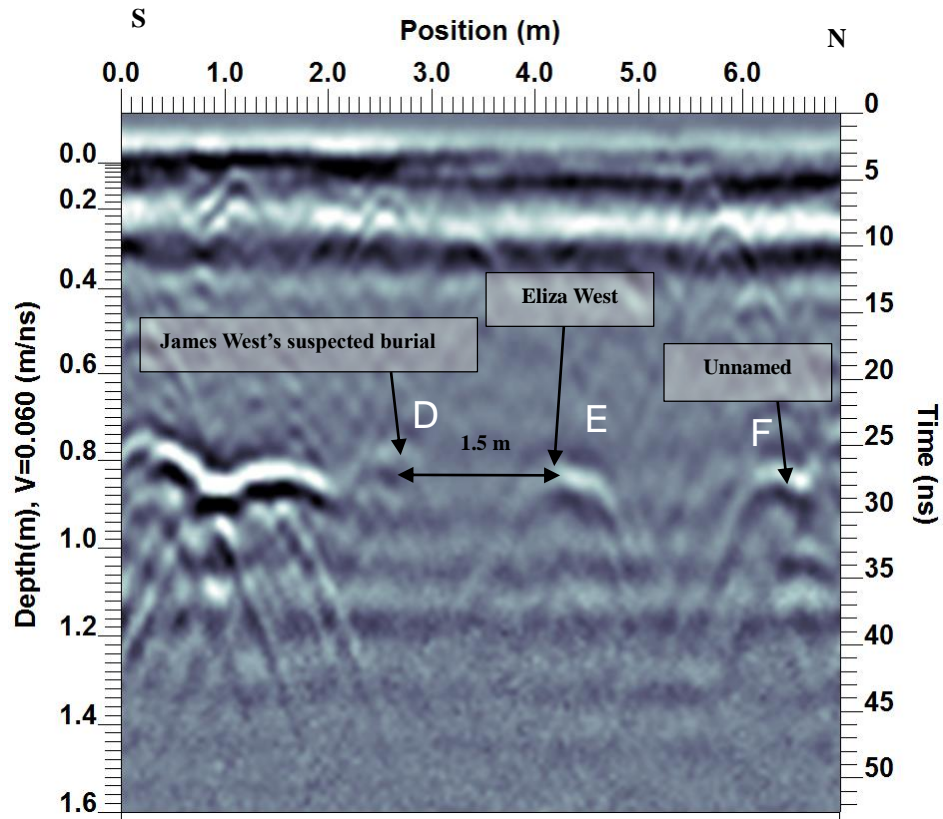


Figure 3.28. Unmigrated GPR section is showing GPR reflections of known burials, labeled E for Eliza West and F for an unnamed headstone. D is suspected to be the burial of James West. The location of D matches the location from the archaeological record.

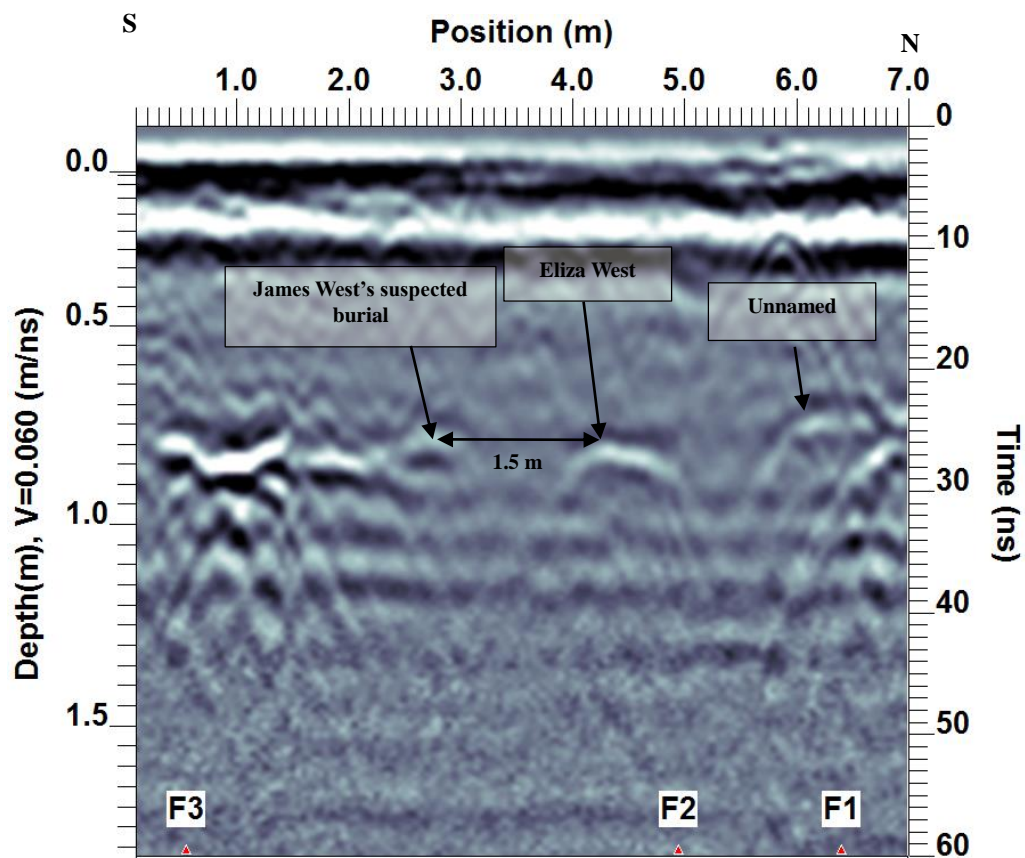


Figure 3.29. Unmigrated GPR section is showing GPR reflections of known burials, labeled E for Eliza West and F for an unnamed headstone. D is suspected to be the burial of James West. The location of D matches the location from the archaeological record.

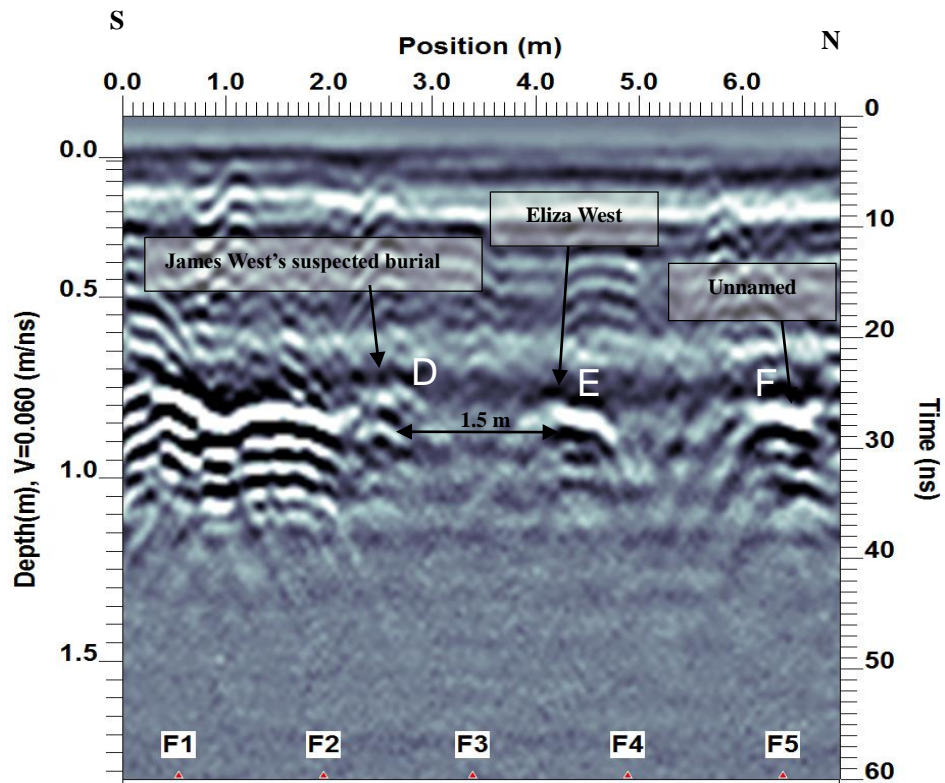


Figure 3.30. Migrated GPR section is showing GPR reflections of known burials, labeled E for Eliza West and F for an unnamed headstone. D is suspected to be the burial of James West. The location of D matches the location from the archaeological record.



Figure 3.31. Photograph showing the location of nearby trees that are in the GPR survey line.

We investigated a GPR depth slice at 0.85 m to determine if we could see the top of the suspected burial of James West (D), burial of Eliza West (E) and the unnamed headstone (F). Eliza West burial is a wooden burial (RIP: 1914) and it has a dimension of 0.6 m by 1.5 m in the depth slice and this suggests a burial. The top of James West's burial is harder to identify on the depth slice because of the presence of the high amplitude anomaly adjacent to it (Figure 3.32). The GPR depth slice map overlain on the exaggerated TLS

elevation profile shows areas of surface depression labeled D and E that correspond to the burials D and E in Figure 3.33. Area D shows the suspected burial of James West lies on a slope.

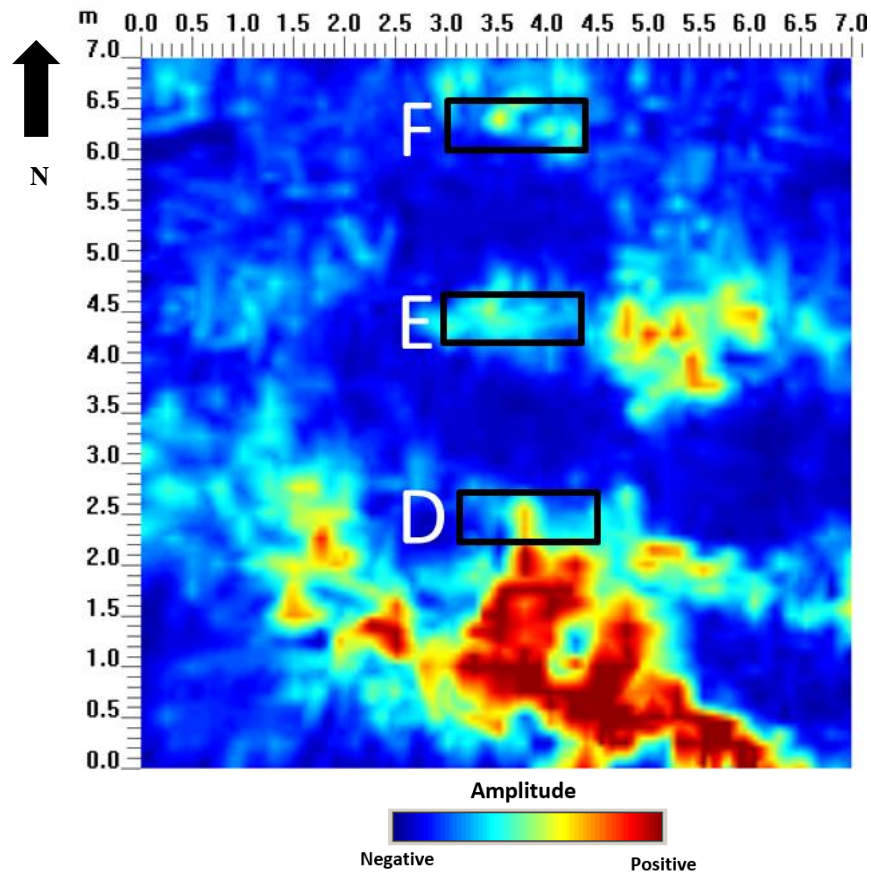


Figure 3.32. GPR depth slice at 0.85 m indicates the top of the suspected burial of James West (D). E and F belong to burials of Eliza West and the unnamed headstone. The anomaly located at D is harder to identify on the depth slice because of the presence of the high amplitude anomaly. The high amplitude anomaly is suspected to be a tree root system from nearby trees. D is the corresponding location on the TLS elevation map with a surface depression.

The anomaly observed at a depth of 0.8 in Figure 3.28, Figure 3.29, and Figure 3.30 is consistent with the depth where we observe the clay boundary. The observation of the depth slice shows that it exhibits a strong event and it has a lateral extent. The anomaly is also in a close proximity of a tree as shown in Figure 3.31. These two observations suggest two probable interpretations of the strong anomaly which can be either a tree root system or the clay boundary.

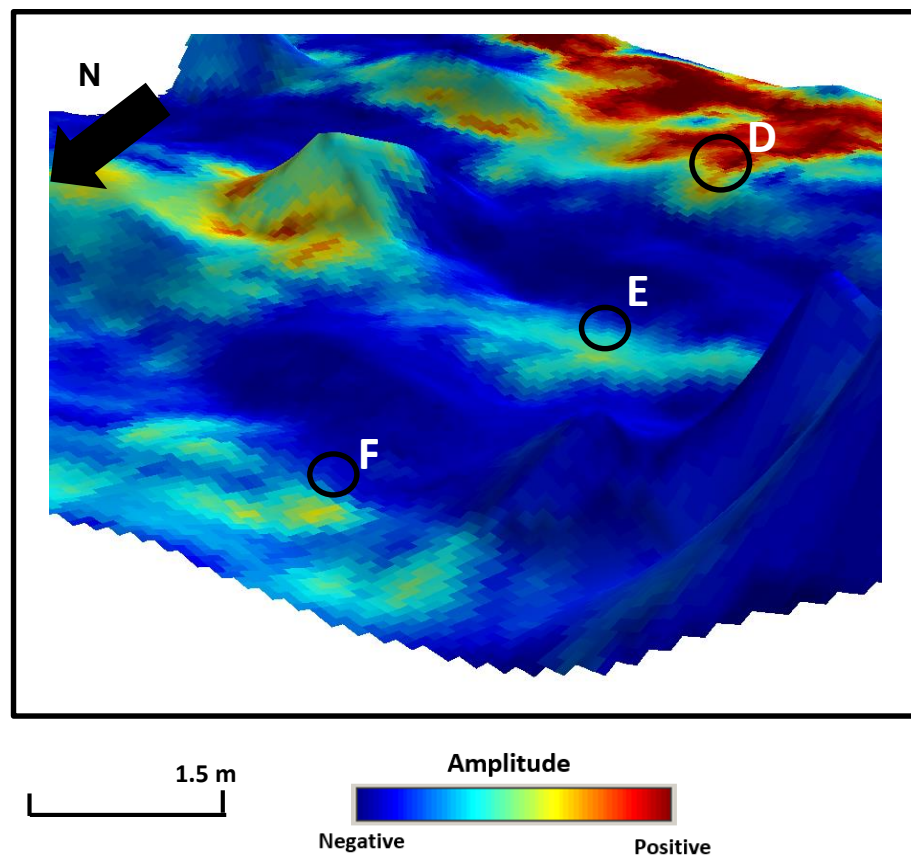


Figure 3.33. GPR depth map overlain on the exaggerated TLS elevation profile shows areas of surface depression D and E corresponding to the burials D and E in Figure 4.23. Area D shows the suspected burial of James West lies on a slope.

3.11 Conclusions

We have collected soil samples, GPR, and TLS measurements to characterize burials at the Mueschke Cemetery, Houston. These geophysical measurements along with the cemetery records and oral histories provided strong evidence that led to two probable locations of unmarked burials including the oldest known burial of James West. The discovery and the geophysical evidence suggest GPR applicability for detecting burials in Mueschke Cemetery area. The results from this work will be used by the Mueschke Cemetery Association as a part of the application process to secure a Texas Historic Marker along with Historic Texas Cemetery Designation. Understanding the soil grain size, physical parameters, and stratigraphy supports the suitability of using GPR in the area, the burial characterization on the GPR radargram, and the interpretation. Numerical modeling provides initial findings on the burial characterization that includes the shape and its size. The effectiveness of 2D and 3D GPR template surveys to characterize burial over known burials suggest they can be possibly adopted as a systematic approach to finding historical unmarked burials. Multiple methods employed to obtain an accurate GPR velocity as a depth conversion is recommended. The choice of using 250 MHz antenna is sufficient to probe the burial depth and to produce excellent burial GPR images in Houston soil condition. The discovery of the two unmarked burials assisted by the joint application of the GPR amplitude depth slice images and TLS surface data recommends that they can serve as direct burial indicators. These results also highlight the power of the integration of GPR and TLS technique in characterizing the concrete and wooden coffin unmarked burials for the historical preservation effort. The burial can be detected by both TLS and

GPR. TLS survey takes shorter time than the GPR method. However, GPR gives more data to confirm the burial. The geophysical approach presented can also be applied to other near-surface problems where GPR profiles and TLS surface tomography can be integrated, for example, in stratigraphy, hazard assessment, and fracture characterization. Further investigations of TLS dips which do not correlate with known burials by GPR surveys will reveal if the anomalies are not false negative. Also, studies about the GPR response of bones will provide more detailed evidence to detect wooden burials.

Acknowledgements

We would like to thank Mr. Brian Kyser of Lone Star College-North Harris for initiating this geo-archaeological work. Our gratefulness to Dr. Robert Wiley, Mr. Marcus Zinecker and Ms. Yesenia Rivera for the assistance to acquire the GPR data. Also, Mrs. Rebecca Stone of the Mueschke Cemetery Association whose grandparents are buried at Mueschke Cemetery for permission to perform the excavation near the cemetery and the oral histories. Our gratitude to Greg Johnson, Ms. Marie Chong and Mr. Chris Martin of Sensors & Software for the software license and constructive technical feedback. Thank you to Mr. Ady Geda and Ms. Joan-Marie Blanco, who helped during the excavation. We appreciate the work of Dr. Nikolay Dyaur of the Allied Geophysical Lab (AGL) for preparing the soil samples and Dr. Yinxi Zhang of the Well Logging Lab at the Department of Electrical Engineering of the University of Houston for conducting the dielectric constant and conductivity experiment. Our gratitude to Mr. Greg Sill and the Geochemistry

Lab of the University of Houston for the soil moisture experiment. We also want to acknowledge Mr. Darren Hauser of the National Center for Airborne Laser Mapping for the TLS survey. We are grateful to Mr. Li Chang and Ms. Vaughn Robla for the CMP survey. Our gratefulness to Dr. Julia Wellner, Ms. Yuribia Munoz, and Ms. Helena Manuel of Wellner Sedimentology Lab at The University of Houston. Our appreciation to Mr. Ismail Abir, Ms. Aubrey Hepler and Mr. William Savage for the TLS processing guidance. We want to thank Ms. Larkin Spires for the fruitful discussion and suggestions.

References

- Algeo, J. T., 2012, The effectiveness of using GPR to monitor changes in soil water content in clayey floodplain soils due to rain events before stream modifications: GSA Annual Meeting.
- Annan, P., 2009, Electromagnetic principles of ground penetrating radar, *in* H. M. Jol, eds., Ground penetrating radar: theory and applications: Elsevier, 1-40.
- Angel Conejo-Martín, M., T. Ramón Herrero-Tejedor, J. Lapazaran, E. Perez-Martin, J. Otero, J.F. Prieto, J. Velasco Angel, 2014, Characterization of Cavities Using the GPR, LIDAR and GNSS Techniques: Pure and Applied Geophysics, November 2015, 172, 3123-3137.
- Aziz, A. A., and R. R. Stewart, 2013, Probing the past: Subsurface imaging to identify burials at the Mueschke Cemetery, Houston: GSH Journal, 4, 28.
- Bevan, B. W., 1991, The search for graves: Geophysics, 56, 1310-1319.

- Bode, J. A. and H. M. Jol, 2005. In search of a missing child: a geophysical investigation of a cemetery: 39th Annual Meeting of the North-Central Section, GSA, Abstracts with Programs, 37, p. 100.
- Cihlar, J., and F. T. Ulaby, 1974, Dielectric properties of soils as a function of moisture content: RSL Tech. Rep, 177-47.
- Conyers, L. B., 2004, Ground-penetrating radar for archaeology. Walnut Creek, CA: AltaMira Press.
- Damiata, B. N., J. M. Steinberg, D. J. Bolender, and G. Zoenga, 2013, Imaging skeletal remains with ground-penetrating radar: comparative results over two graves from Viking Age and Medieval churchyards on the Stóra-Seyla farm, northern Iceland: *Journal of Archeological Science*, 40, 268-278.
- Davenport, C. G., 2001, Remote sensing applications in forensic investigations: *Historical Archaeology*, 35, 87-100.
- Doepkens, W. P., 1991, Excavations at Mareen Duvall's Middle Plantation of South River Hundred: Gateway Press, Baltimore.
- Doolittle, J. A., F. E. Minzenmayer, S. W. Waltman, E. C. Benham, J. W. Tuttle, and S. Peaslee, 2007, Ground-penetrating radar soil suitability map of the conterminous United States: *Geoderma*, 141, 416- 421.
- Doolittle, J.A., and N. F. Bellantoni, 2010, The search for graves with ground-penetrating radar in Connecticut: *Journal of Archaeological Science*, 37, 941-949.

- Evans, R.D., R. Morrow, and J. Nash, 2014, The use of ground penetrating radar to investigate a churchyard burial plot: IEEE Proceedings of the 15th International Conference on Ground Penetrating Radar (GPR 2014).
- Fiedler, S., B. Illich, J. Berger, and M. Graw, 2009, The effectiveness of ground penetrating radar surveys in the location of unmarked burial sites in modern cemeteries: *Journal of Applied Geophysics*, 68, 380-385.
- Fisher, E., G. A. McMechan, and A. P., Annan, 1992, Acquisition and processing of wide-aperture ground-penetrating radar data: *Geophysics*, 57, 495-504.
- Fisher, S. C., R. R. Stewart, and H. M. Jol, 1996. Ground penetrating radar (GPR) data enhancement using seismic techniques: *Journal Environmental and Engineering Geophysics*, 2, 89-96.
- Flores, J., 2013, The Survey of Mueschke Cemetery: A Community Preservation Project: Honors Scholar Capstone, The Honors College at Lone Star College-North Harris.
- Hansen, J. D., J. K. Pringle, and J. Goodwin, 2014, GPR and bulk ground resistivity surveys in graveyards: locating unmarked burials, in contrasting soil types: *Forensic Science International*, 237, e14-e29.
- Hauser, D. L., 2013, Three-Dimensional Accuracy Analysis of a Mapping-Grade Mobile Laser Scanning System: Master's Thesis, University of Houston.
- Henning, A. T., G. Burns., R. Hoffman, and B. Jacoby, 2008, *Journal of History and Culture; Using Science to Uncover History: A Geophysical Investigation of Wyatt Chapel Cemetery*; page 51.

- Henning, A. T., D. S. Sawyer, D. Wallace, and A. Kahera., 2009, Geophysical Survey of an Abandoned Cemetery in Prairie View, Texas: Unmarked Burials from Slave Era Discovered on College Campus, AGU, Expanded Abstracts.
- Johnson, C., 2010, Renovating Old Watkins Cemetery: Retrieved from <http://www.watkinscemetery.com/PROJECT.html>.
- Kadioglu, S., M. Kadioglu, and Y. K. Kadioglu, 2013, Identifying of buried archaeological remains with ground penetrating radar, polarized microscope and confocal Raman spectroscopy methods in ancient city of Nysa, Aydin, Turkey: Journal of Archaeological Science, 40, 3569-3583.
- King, J. A., B. W. Bevan, and R. J. Hurry, 1993, The Reliability of Geophysical Surveys at Historic Period Cemeteries: An Example from the Plains Cemetery, Mechanicsville, Maryland: Historical Archaeology, 27, 4–16.
- LaFle`che, P.T., J. P., Todoeschuck, O. G. Jensen, A. S. Judge, 1991, Analysis of ground-probing radar data: predictive deconvolution: Canadian Geotechnical Journal, 28, 134– 139.
- Neiman, F.D., 1980, Field archeology if the Clifts Plantation Site, Westmoreland County, Virginia, Robert E. Lee memorial Association, Stratford, VA.
- Nobes, D. C., 2000, The search for “Yvonne”: a case example of the delineation of a grave using near-surface geophysical methods: Journal of Forensic Sciences, 45, 715-721.
- Powell, K., 2004, Detecting buried human remains using near-surface geophysical instruments: Exploration Geophysics, 35, 88-92.

Schultz, J.J., 2007, Using ground-penetrating radar to locate clandestine graves of homicide victims: forming forensic archaeology partnerships with law enforcement: *Homicide Studies*, **11**, 15-29.

Texas A & M AgriLife Research Soil Characterization Lab, 2010, Soil Characterization Database.

Tzanis A., 2006, Matgpr: A freeware matlab package for the analysis of common-offset GPR data: *Geophysical Research Abstracts*, **8**, No. 09448.

Ulriksen, C. P. F., 1981, Application of impulse radar to civil engineering: Ph.D. thesis, Lund University of Technology.

USDA, 2009, Ground Penetrating Radar Suitability Map, 1:600,000: Retrieved from http://www.nrcs.usda.gov/Internet/FSE_DOCUMENTS/nrcs142p2_052162.pdf.

USGS, 2002, Texas Geology, Retrieved from URL: <http://tx.usgs.gov/texasgeology/history.html>.

Westwood-Turowski, A., and J. A. King, 1991, Excavations at the Patuxent Point Cemetery, a Mid- 17th-Century Family Graveyard in Maryland: Memorandum on file, Jefferson Patterson Park and Museum, St. Leonard.

4 3D GROUND-PENETRATING RADAR (GPR) CHARACTERIZATION OF SANDY MOUTH-BARS IN AN OUTCROP RESERVOIR ANALOGS: CRETACEOUS FERRON SANDSTONE, SOUTHEASTERN UTAH, USA.

Abstract

A 3D ground-penetrating radar (GPR) survey was conducted to visualize architectural elements of friction-dominated distributary mouth bars in proximal delta-front deposits in the Cretaceous Ferron Sandstone at the top of the Notom Delta in southeastern Utah, U.S.A. Sensors and Software's Noggin SmartCart 250 MHz was used over a 25 m x 15 m grid resulting in 12.5 cm vertical resolution. We employed an orthogonal acquisition geometry and a spatial sampling of 0.5 m for the inline (dip direction) and 1.5 m for the crossline (strike direction). Standard processing flows, including time-zero correction, dewow, gain, background subtraction and 2D migration, were used to increase the signal-to-noise ratio. Formation velocity estimates from hyperbola matching yielded 0.131 m/ns, which is comparable to the velocity of about 0.125 m/ns. The calculated average dielectric constant (directly related to volumetric water content) is 5.2 and matches unsaturated sandstone. The depth of GPR penetration is limited to approximately 3 m, likely due to the compaction/carbonate cementation in the rock and interbedded layers of finer-grained material contributing to higher attenuation of the GPR signal. Calculation of the medium porosity using an adapted Wyllie Time Average equation yields 7.8 % porosity which is consistent with the average porosity of (5-10%) obtained from the literature. GPR images revealed the geometry of architectural

elements, such as small-scale bedding (0.6 m) and the extent (9 m) of major bounding surfaces. Three major radar facies were observed in this study including a terminal distributary channel (1.25 m thick) filled with distributary mouth bars, a progradational mouth bar with a dip angle of approximately 20°, and a laterally continuous basal planar bed deposited in an inertia-dominated river. The GPR radargrams were not only capable of imaging the 3-D architecture of individual unit bars, but also identified two significant proximal delta-front facies: upper friction-dominated, dune-scale cross beds and bar-scale large foresets, interpreted as inertia-dominated basal planar beds. Interpretations of 2-D and 3-D radar profiles describe the heterogeneity of the terminal distributary channel and suggest that a complicated depositional environment that exhibits a various degree of spatial variability. The 3D GPR imaging of the internal structure of the terminal distributary mouth bar has allowed the quantification of its geometry and the identification of three major radar facies. Accurate 3D models of the internal structures of reservoir analogs are important elements in the fluid flow simulation used during the petroleum production stage.

4.1 Introduction

Deltas are formed when river-borne sediments meet a standing body of water. The sandy components of a delta include distributary mouth bars, distributary channels, delta plains, and crevasse splays (Coleman and Prior, 1982; Morse, 1994). In a marine environment, sandstone reservoir rocks are deposited in deltaic, near shore and deep marine settings. Distributary mouth bars and terminal distributary channels are known to form the most

prolific sandstone reservoirs (e.g., Bhattacharya, 2006). Characteristically, distributary mouth-bar sandstones average about 16.2 % in porosity and 0.19 mm in grain size (fine-grained) (Moore et al., 2012). To illustrate, a large mouth bar oil field, Statfjord Field in the U.K. and Norway produces from 300 m-thick net pay. The Safaniya Khafji Field produces over 32 BBOE from stacked deltaic sandstones reservoirs (Morse, 1994). Another example is the Prudhoe Bay Field, which is a complex fluvio-deltaic system that contains thick fluvial deposits overlying more heterolithic mouth-bar and delta front sandstones (Tye et al., 1999).

Bounding surfaces of deltaic architectural elements reflect mouth bar growth and abandonments, as well as recording changes in the flow regime as the delta builds (Gani and Bhattacharya, 2007; Tatum and Francke, 2012; Ahmed et al., 2014; Li and Bhattacharya, 2014). By mapping the detailed internal architecture in three dimensions, the lateral extent of the bounding surfaces and the growth history of architectural elements can be identified. Regular seismic data is excellent in sampling the whole reservoir geometry with vertical resolution typically on the order of hundreds of meters, but it generally lacks the sub-meter resolution required to visualize the internal geobody heterogeneity (Howell et al., 2014). In sparse well data environments, interpolation between available wells may yield an inaccurate representation of the lateral variation of the reservoir architecture.

GPR is an emerging technology for 3D imaging of outcrop analogs to characterize the complicated architecture of subsurface reservoirs (Flint and Bryant, 1993; Beres et al., 1995; McMechan et al., 1997; Corbeanu et al., 2001; Szerbiak et al., 2001; Szerbiak et al.,

2001; Khan et al., 2007; Mukherjee et al., 2012; Bhattacharya et al., 2013). Outcrop geophysical properties are assumed to be representative of those (velocity, porosity, etc.) in the subsurface (Jarrard et al., 2004). GPR provides high-resolution images of shallow subsurface outcrop analogs with wavelengths in the range of centimeters (Asprion and Aigner, 1997). Also, GPR is efficient in mapping lithofacies because it offers real-time output and requires minimal processing (Bridge, 2003).

GPR is useful to study stratigraphies at a variety of scales because the sedimentary characteristics of strata can be interpreted from the radar reflections (Bridge, 2003). Radar reflections in sediments are controlled by the electrical conductivity which is a function of the water content. Water contents in the sediment are affected by the bounding surfaces, cross beddings, changes in grain size, and lamination. The changes in the water content are influenced by the permeability and porosity changes of the cross-bedded layers and the bottom-set layers (Pryor, 1973; Beard and Weyl, 1973; Jordan and Pryor, 1992). The Cretaceous Ferron Sandstone is ideal for GPR application due to little clay or silt presence and its importance as an analog to subsurface fluvio-deltaic reservoirs (Barton, 1994; Knox and Barton, 1999). Clay-rich materials are highly attenuating and limit the GPR depth of penetration.

The objectives of the study are to (1) investigate the GPR potential to resolve 3D internal architecture of friction-dominated, radial distributary mouth bars, (2) identify radar facies and relate them to architectural and sedimentological stratigraphic interpretation, (3) determine the internal geometry, (4) interpret these various proximal delta front mouth bar

facies from the GPR images and then compare our interpretation with the finding by Li (2014) in 2D-vertical sections, and (5) extract geophysical information, such as the radar velocity, depth of penetration, vertical resolution, and porosity.

4.2 Geological setting and stratigraphy

The Cretaceous Ferron Sandstone Member of the Mancos Shale Formation is one of a series of fluvio-deltaic clastic wedges, which prograded into the Western Cordilleran foreland basin formed during the Sevier Orogeny (Peterson and Ryder, 1975; Ryer and Anderson, 2004; Zhu et al., 2012). The Ferron Sandstone Member is a river-dominated, storm and fair weather wave--influenced deltaic system. It crops out in three different fluvial-deltaic complexes; including the Last Chance, Notom, and Vernal, which prograded into the western margin of the Cretaceous Interior Seaway (Hale and Van De Graaff, 1964; Hale, 1972; Hill, 1982). In this study, we focus on the Notom Delta. The Ferron Sandstone has long been considered as an analog for fluvio-deltaic hydrocarbon reservoirs (McMechan et al., 1997; Szerbiak et al., 2001; Chidsey et al, 2004, and references therein) such as in the Gulf of Mexico, Alaskan North Slope, North Sea, and Rocky Mountain Basin (Bhattacharya and Tye, 2004). The Ferron sandstone is also the source of an active gas play in Utah, as well as important for its coal resources. Ferron coalbed methane is reported to have 10 TCF of gas reserves (Gloyn and Sommer, 1993). Previous sequence stratigraphic studies divided the Notom delta wedge of the Ferron Sandstone Member into 6 depositional sequences, 18 parasequence sets and 43 parasequences (Li et al., 2011; Zhu et al., 2012) (Figure 4.1). The parasequences are considered as primary reservoir building

blocks because marine and delta-plain shales act as laterally extensive permeability barriers. Some communication may be established between parasequence because of erosion of the shale. The upper two sequences are characterized by a well-developed regional scale fluvial compound incised-valley system (Li et al., 2010; Li and Bhattacharya, 2013, Ullah et al., 2015, Wu et al., 2015). In this work, we focus on the distal exposures of Parasequence 6 of sequence 2 (Figure 5.1), which is characterized by progradational, distributary mouth bars fed by an incised-valley (Ahmed et al., 2014). Parasequence 6 is about 20 m thick and contains prodelta, distal delta front, proximal delta front, terminal distributary channel deposit, and shoreface deposits (Ahmed et al., 2014; Li et al., 2014) (Figure 4.2). Due to the limited GPR penetration depth which is approximately 3 m, the focus of this study is on the proximal delta front and terminal distributary channel deposits.

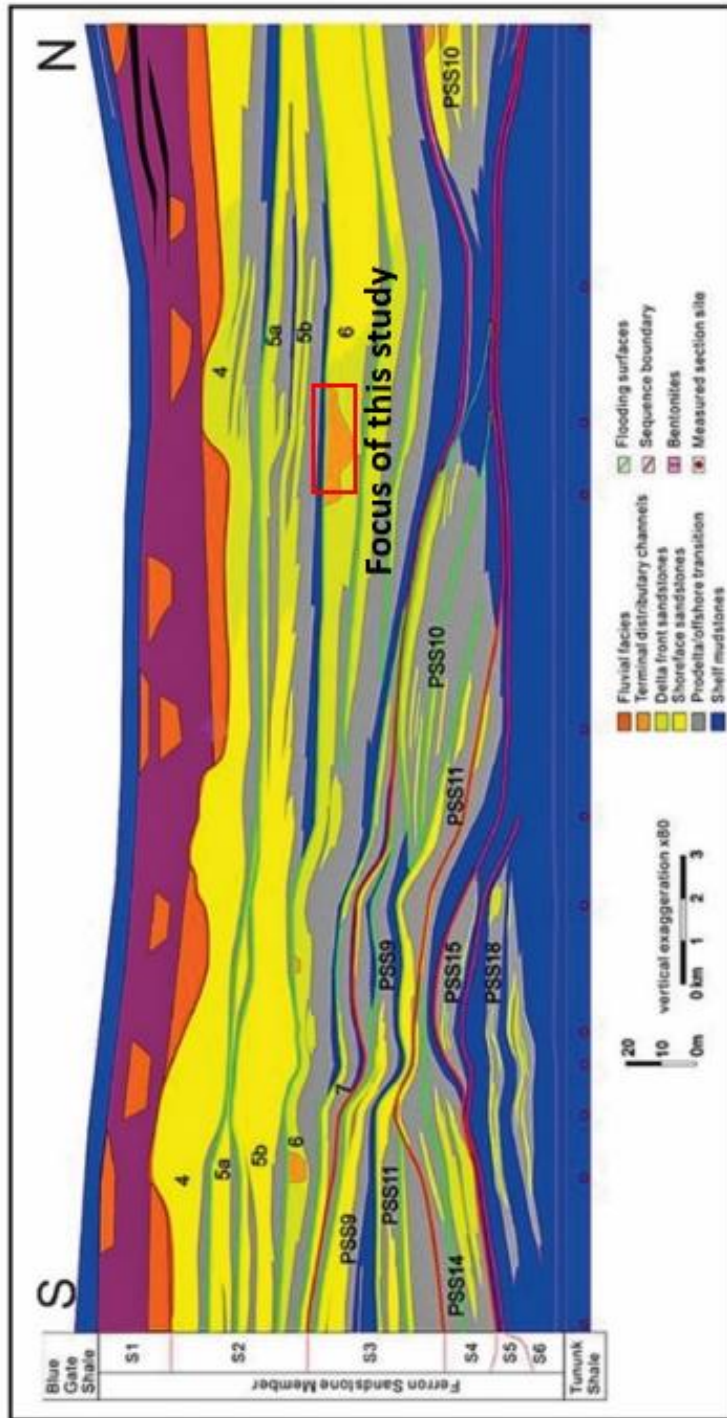


Figure 4.1. Oblique depositional strike sequence stratigraphic framework of the Notom delta by Li et al., (2010) shows the distributary mouth bar located in parasequence 6 of sequence 2 which is the focus of this study (marked by a red rectangle).

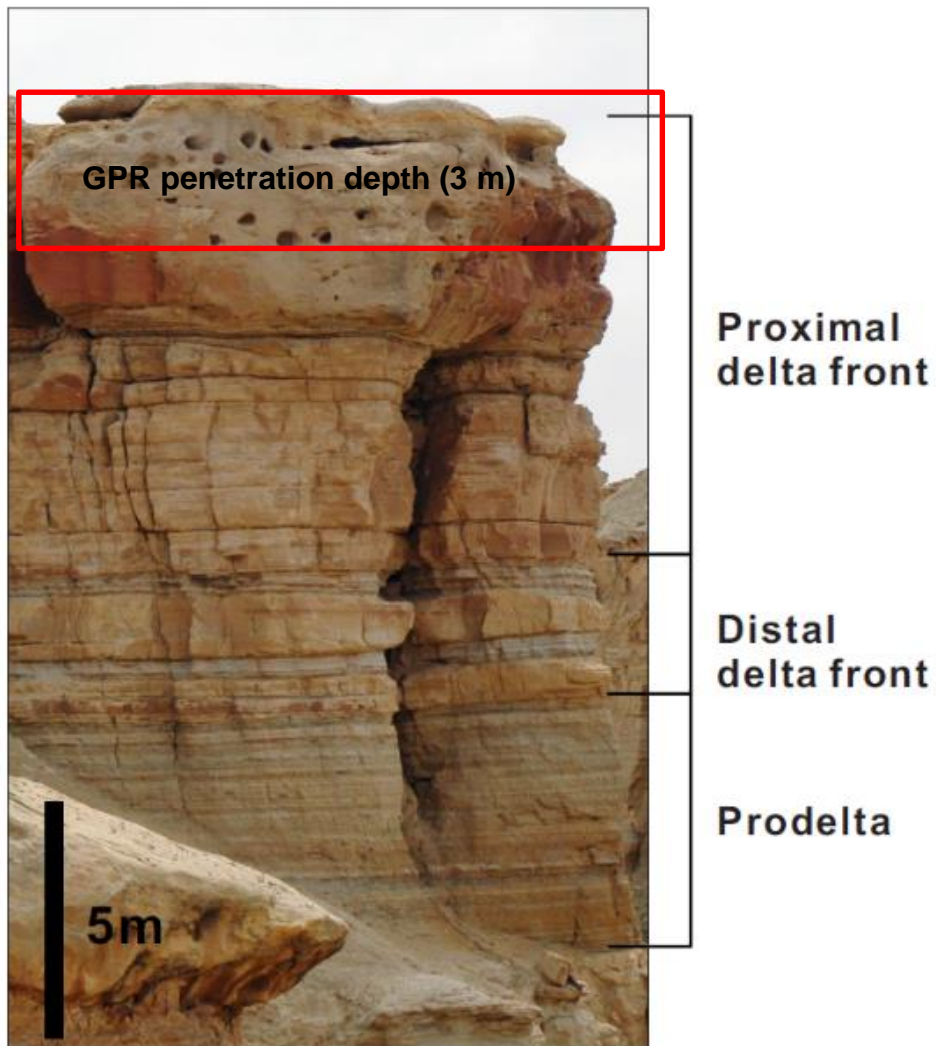


Figure 4.2. A. photograph of vertical section of the river-dominated Parasequence 6 (Li and Bhattacharya, 2013).

The survey location includes extensive plan-view exposures of proximal delta-front sandstone facies, including mouth bars and terminal distributary channels. Previous studies (e.g., Ahmed et al., 2014; Li et al., 2014) documented river-dominated distributary mouth bars and terminal distributary channels as essential building blocks of the Ferron deltaic

parasequences (Figure 4.3).

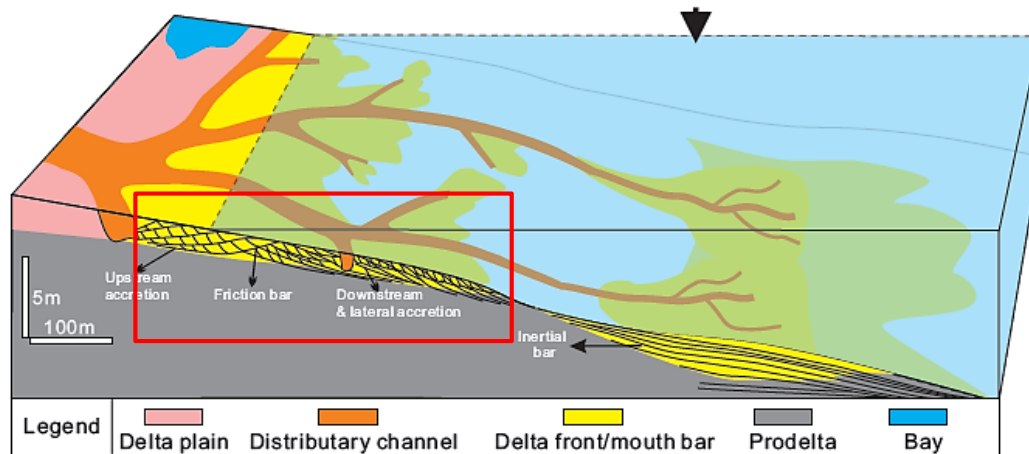


Figure 4.3. The distributary mouth bar (red box) model depicted by Li (2013).

Previous facies architectural studies of these sandstones in vertical cliff exposures showed that the upper part of Parasequence 6 consists of a series of medium- to large-scale cross bedded fine- to medium-grained sandstones, with associated low-relief scours interpreted as friction-dominated mouth bars that filled terminal distributary channels, between 2 to 3 meters deep (Ahmed et al., 2014, Li et al., 2014). Li et al. (2014) identified three lithofacies in the proximal delta-front deposits in Parasequence 6 (1) basal planar beds at the bottom, (2) low-angle cross beds in the middle and (3) dune scale and bar-scale angle-of-repose cross stratified sandstones with low-relief scours at the top. Planar beds are about 1 m thick, show small-scale undulations and can span a few hundred meters. These occurred in the lower half of the parasequence and were interpreted as detached, inertia-dominated bars

(Wright, 1977; Li et al., 2014). Low-angle cross beds are usually about 1.5 m thick and a few tens of meters wide and were interpreted as the transitional facies from inertia-dominated facies below and friction-dominated facies above (Li et al., 2014). Upper facies show decimeter to meter-thick angle-of-repose cross beds (Figure 4.4a and Figure 4.4b). In plan view, these form extensive rib-and-furrow structures (representing exhumed trough cross beds) (Figure 4.4c). The ribs are interpreted to approximate the width of the bar-form and range from a few meters up to 15 meters wide. Ribs are concave downstream. In cross section, cross-strata show a sigmoidal structure in which a low-angle relatively planar foreset passes down-dip into angle-of-repose, concave-up foresets with tangential bottom sets. These were interpreted to be deposited as radial mouth bars, dominated by bedload transport and decelerating flows in a friction-dominated environment (Wright, 1977; Turner and Tester, 2006; Li et al., 2014).

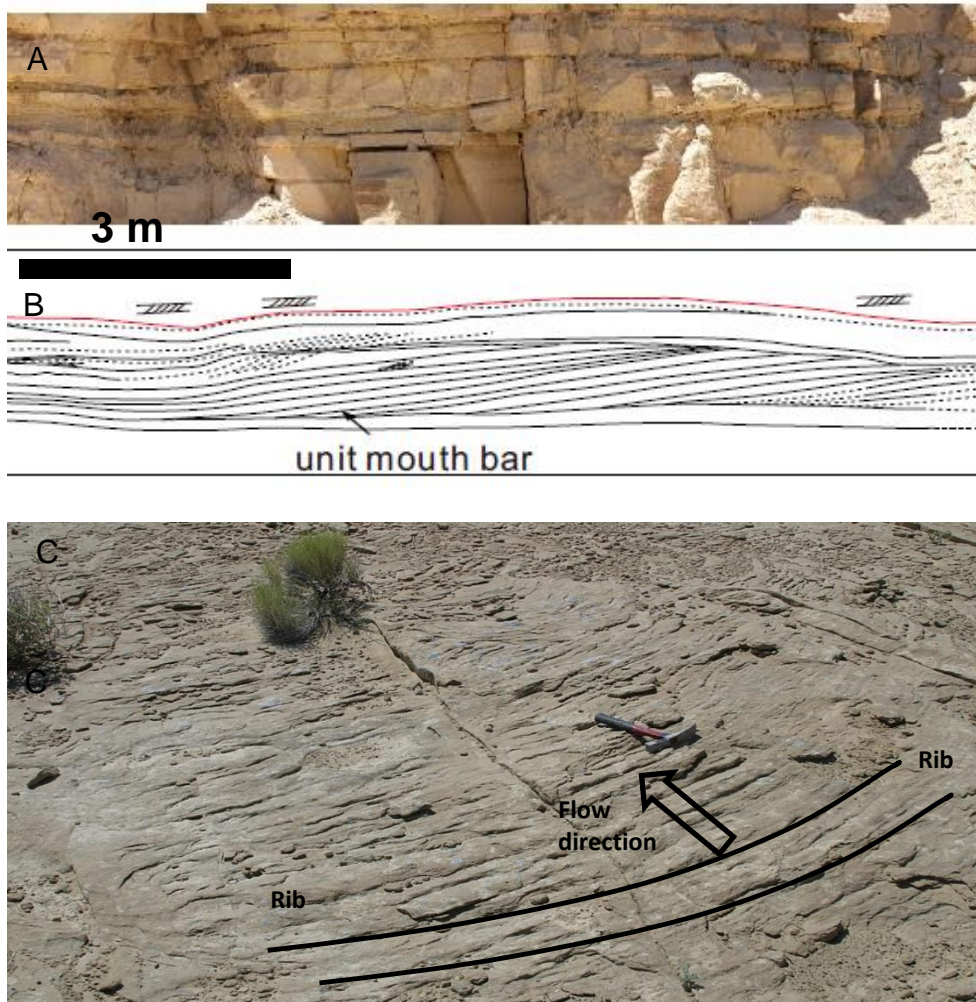


Figure 4.4. (A) Photograph of the cross section of unit bars. (B) A plan-view exposure of large-scale foresets (classic rib-and-furrow pattern) interpreted as unit mouth bars (Li et al., 2014). The width range of the individual rib is up to a few tens of meters and the flow direction is perpendicular to the rib-elongation direction (Ahmed et al, 2014).

4.3 Study area

The study area is located east of Coalmine Wash, 10 kilometers north east of Factory Butte and 25 kilometers northwest of Hanksville in southeastern Utah (Figure 4.5). Lack of vegetation, a flat surface, and extensive outcrops along Coalmine Wash provides an ideal place to acquire GPR data. The elevation of the study area is 1509 m. The survey area is selected because of the spectacular plan-view outcrop exposures of river-dominated delta front deposits. There is no Quaternary cover on top of the survey area that inhibits the GPR imaging. This survey is in a very arid location on top of sandstone directly adjacent to a 100 m cliff. The area and cliff are devoid of vegetation which suggests that there is very little free water in the near surface. The view of the cliff shows the near surface to be solely sandstone.

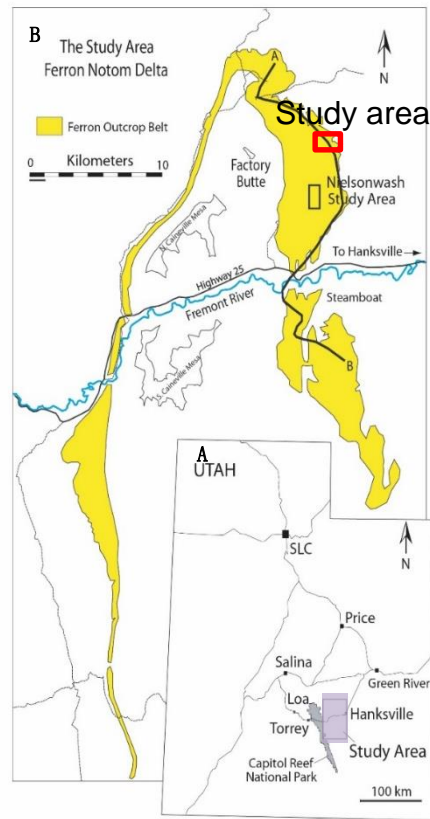


Figure 4.5. Base map A shows the regional area of study and red box in the base map B shows the location of the study area located in the Coalmine Wash area (modified from Ullah et al., 2015).

4.4 GPR data acquisition

The data were collected adjacent to cliff outcrops of delta front sandstones as shown in Figure 4.6. The grid was selected specifically to image a single set of downstream accreting mouth bar deposits. A 3D common-offset GPR reflection dataset was acquired using Sensors & Software's Noggin Plus Smart Cart 250 MHz System (Figure 4.7). A total of 82 GPR lines were acquired in the inline (dip direction) and the crossline (strike direction). The weather was dry, clear, with no rain and an average of wind of 7 knots

and temperature of 38° C when the survey was acquired. Data acquisition was undertaken in a parallel forward-reverse procedure to provide efficient acquisition. This survey orientation provided well-sampled inline data. A 25 m (inline) by 15 m (crossline) survey grid with a line spacing of 1.5 m and 0.5 m respectively was designed on the outcrop. The details of the survey parameters are shown in Table 4.1. We used a measuring tape to guide the Smart Cart to increase the efficiency of the data acquisition. The grid was oriented such that the inline is parallel to the northeast accretion direction (i.e. parallel to the channel flow). The size of the grid was chosen to completely sample one of the larger rib and furrow sets in an area that has a relatively smooth surface and minimal vegetational cover.

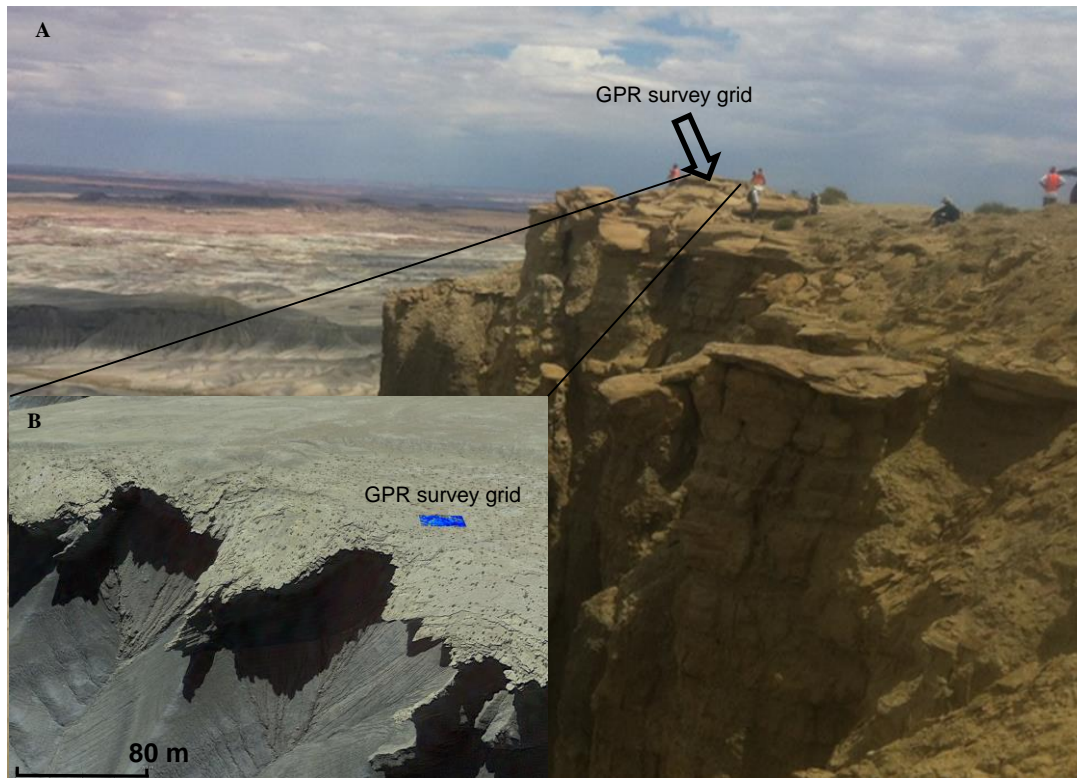


Figure 4.6. (A) Photograph of the survey area with the arrow pointing to the GPR survey location. The elevation of the study area is 1509 m. (B) The Google Earth image of the GPR survey location with the GPR grid. The Google Earth view is pointing toward the south.

Table 4.1. GPR survey parameters to acquire 3D data to image a single set of forward-accreting mouth-bar deposits.

Parameter	Value
Center frequency	250 MHz
Line spacing	0.5 m (inline) 1.5 m (crossline)
Step size	0.1 m
Vertical stacking	64
Sample rate	0.40 ns
Antenna separation	0.27 m

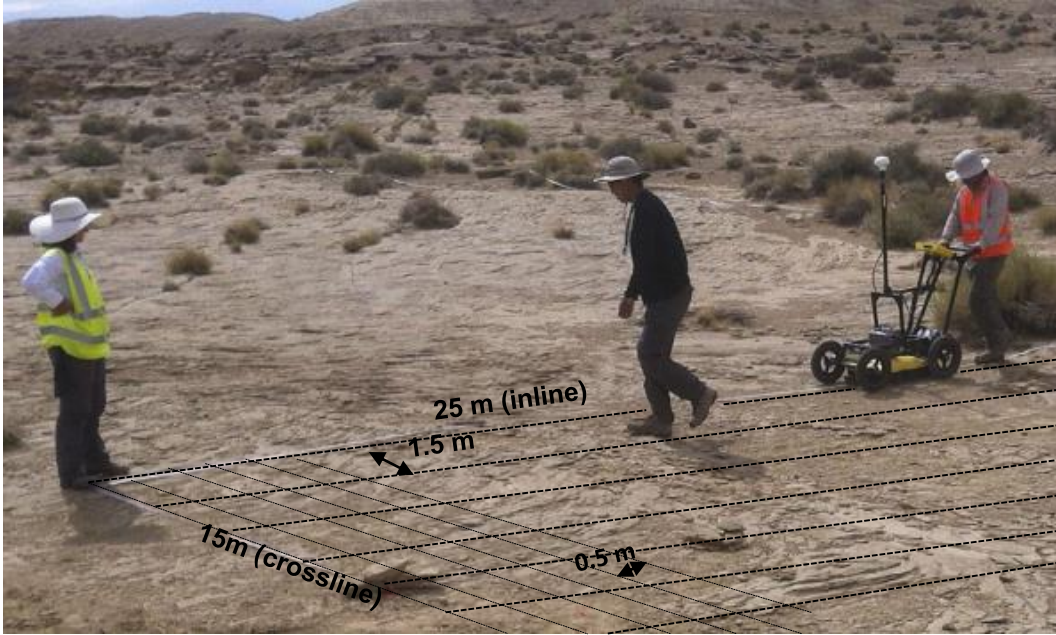


Figure 4.7. A photograph of the 3D GPR survey acquisition using Sensors and Software's Noggin Plus SmartCart 250 MHz antenna. A rectangular 3D GPR survey of 25 m (inline) by 15 m (crossline) was undertaken on the top of the outcrop. Virtual black dash lines were drawn on the photograph to show the inline and crossline survey lines (Not to scale).

4.5 Data processing and analysis

In this section, we outline the processing flow and analyze GPR-reflection images to evaluate the vertical resolution and the penetration depth. GPR data processing was undertaken using Sensors & Software processing package EKKOView Deluxe. The main steps are: time-zero correction (to position traces to a common time-zero position), dewow (temporal filter to remove very-low frequency signals), spherical and exponential compensation gain (to compensate the radar signal attenuation and probe deeper section), background removal (to enhance shallow section by removing the air and ground waves), and 2D-migration (Figure 4.8). The use of background removal enhances the ability to

see dipping reflections and is useful to analyze shallow events (Moldoveanue et al., 2003). Background subtraction must be used with care as it can remove horizontal events that are part of the geological structure.

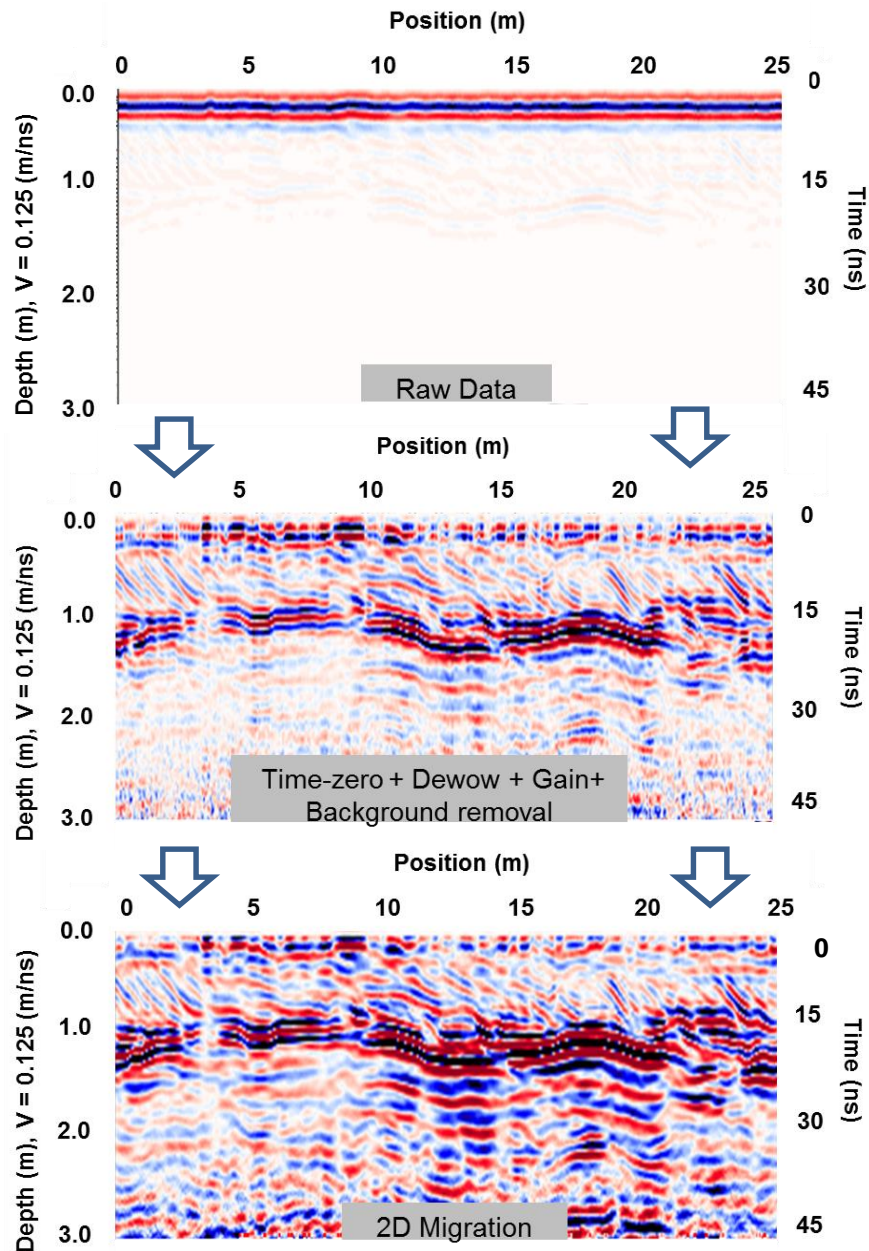


Figure 4.8. Detailed GPR data processing flow diagram.

The 250 MHz GPR data set gives a vertical resolution (~ 0.125 m) with an approximate penetration depth of about 3 m. The depth of penetration is enough to interpret the top of the proximal delta front. For time to depth conversion, we estimated the GPR velocity using hyperbola matching method and from the literature. The hyperbola matching technique gave a velocity of 0.131 m/ns (Figure 4.9) while the literature reported a velocity of typical dry sandstone as 0.125 m/ns (Lee et al., 2007). We used a constant velocity of 0.125 m/ns in the 2D-migration the depth conversion because the velocity in the literature is an average velocity of many points while the hyperbola matching gives an average velocity of a single point. The value is not much difference and it will make little different in the imaging.

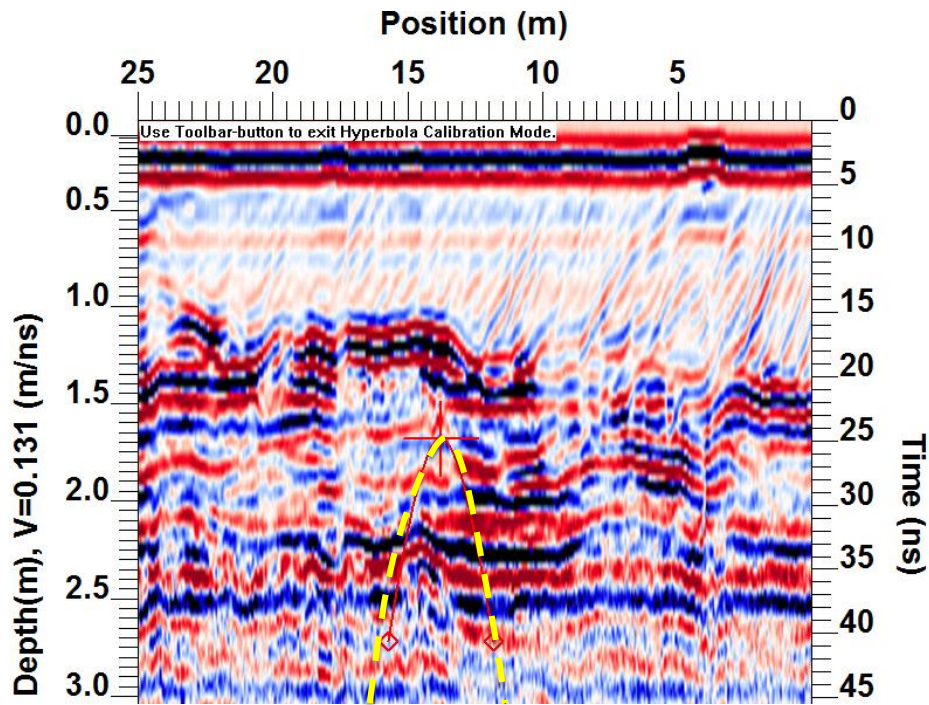


Figure 4.9. Velocity estimation using hyperbola matching method overlaid over a distinct hyperbola yields 0.131 m/ns.

From the measured radar velocity, we estimate the formation porosity by using the Wyllie Time-Average Equation (4.1) (Aitken, 2008):

$$\frac{1}{V_A} = \frac{\emptyset}{V_F} + \frac{1-\emptyset}{V_M} , \quad (4.1)$$

where \emptyset is the porosity, V_A is the measured radar velocity (0.131 m/ns), V_F is the fluid velocity (air = 0.3 m/ns) within the pore space, and V_M is the rock matrix velocity (0.125 m/ns). The calculation yields 7.83 %, which is in the range of the reported average porosity of the Ferron Sandstone (5-10 %) (Jarrard et al., 2004). The calculated porosity can be used to calculate the radar velocity of saturated sandstone. We used 0.033 m/ns to represent the fluid velocity, V_F (Aitken, 2008). The velocity of water-saturated sandstone is 0.103 m/ns which is in the range of wet sandstone (0.09-0.13 m/ns) reported in the literature (Bakker et al., 2007). The calculated average dielectric constant (directly related to volumetric water content) is 5.2 and this matches the dielectric constant of unsaturated sandstone.

4.6 2D-GPR interpretation

Three examples from the 2D- GPR profiles are presented in the following sections to demonstrate how GPR can be used to image the 3D architecture of individual unit bars and to differentiate between different lithofacies in proximal mouth-bar deposits: upper friction-dominated dune-scale cross beds and bar-scale large foresets from lower inertia-dominated basal planar beds, and terminal distributary channels. Six types of reflection

patterns were identified in the GPR survey: wavy, sub-parallel, undulating, prograding, horizontal, continuous, and concave up.

4.6.1 Observation

The GPR data seen in the subsequent images appears to show a strong reflection but the display is a relative display. The absolute amplitude is likely to be small because the rock is dry, porous, and relatively uniform. The survey is close to a cliff so that it has free surfaces on two sides and the ground surface. Given the extremely arid climate there is little possibility of free water in the volume explored. Therefore the variations in impedance in the near surface are very small and likely depend on variations in porosity, grain size and bound water in any clay-based fractions that are present. Petrophysical calculation conducted by Szerbiak et al. 2006 shows the ratio of sand to clay is 27/1. This is a very clean sandstone. The first example shows a 25 m long deep oriented (East-West) GPR profile (Figure 4.10). The figure shows steeply dipping prograding sediments resting on sequence of relatively flat beds. The photograph seen in Figure 4.4 of the surface shows a uniform sandstone with ribs or ridges in a north-south direction. These ribs and their associated furrows can be seen in the GPR cross section as variations in the surface elevation and as the bedding planes down to a depth of 1.25 m. In the image, the rib height is relatively small. This should confirm that the impedance contrasts seen in the GPR data are small and of the size to be expected from variations in grain size or fractions of clay bound water rather than variations in lithology.

From the very bottom of the image up to 1.4 m depth, radar reflections transition from sub-parallel to somewhat wavy reflections. There is an upward increase in reflection thickness and continuity. Undulating continuous thick reflections between 1.0 - 1.4 m depth extend laterally across the GPR profile and show strong reflections compared to the reflections below. Subtle vertical displacements in these laterally continuous reflections are more prominent in the distal part of the image. At depths between 0.4 m and 1.0 m, we observed 3 – 9 m long dipping reflections that change laterally with a varying dip angle. The upper part of this reflection package shows top lap against an overlying low-amplitude, nearly horizontal reflection. The lower part of these oblique reflections downlap onto the underlying high amplitude, continuous reflections that show local depressions or trough-like features.

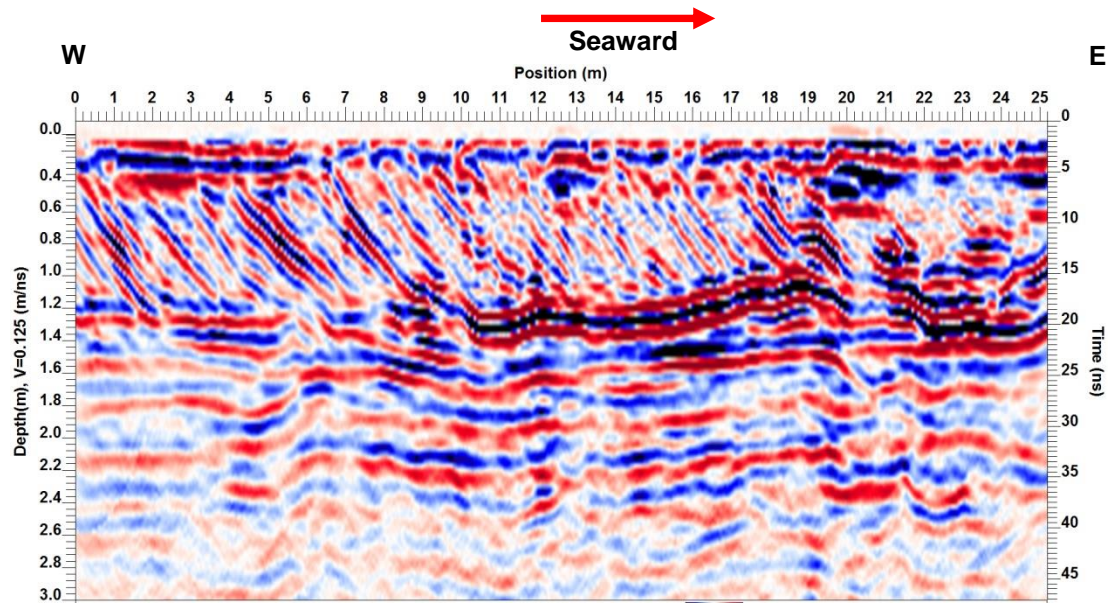


Figure 4.10. GPR image shows the upper dune-scale cross beds interpreted to be deposited in a friction-dominated environment. These are estimated to be deposited subaqueously, in a water depth no more than a few meters.

4.6.2 Interpretation

The apparent vertical lines in the top 40 cm seem to be associated with the weaknesses at bedding plane boundaries. This suggests they are fractures and interesting as analogs to seismic scale fractures. The steeply dipping reflections are interpreted as a downstream accreting mouth bar. Changes in dip record subtle changes in flow velocity and sediment transport as the bar builds. The foreset reflections show a height (thickness) of about 1.2 m, but the exposure of ribs at the surface indicates that there has been some erosion, so bar height was likely somewhat larger. The flatter units at the base of the dipping reflections represent bar topsets and bottomsets.

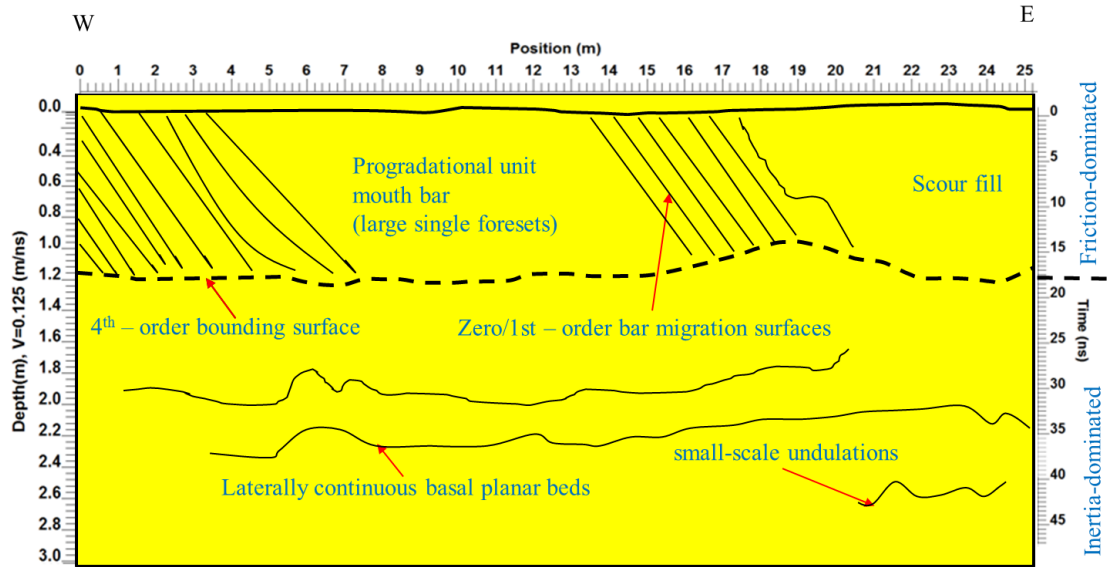


Figure 4.11. GPR image shows the underlying units are the bottomset facies. The bar is estimated deposited subaqueously, in water depth no more than a few meters.

4.6.3 Observation

The second example in Figure 4.12 shows a dip oriented (inline) 2D GPR profile, which shows a significant progradational unit mouth bar oriented in a NW-SE direction. The reflection amplitude starts fading at 2.4 m depth characterized by grainy images indicating signal attenuation. At 1.3 m depth, we observed high-amplitude, nearly-horizontal and moderately continuous, and sub-parallel reflections. The upper part of these reflections top lap at the progradational mouth bar top portion, and the lower part terminates in parallel downlap above high-amplitude, continuous, nearly-horizontal reflections that mark the underlying bounding surface. The dip is interpreted to be in the general downstream direction with a dip angle of 20° (Figure 4.12). The measured dip is a true dip that tells the progradation direction of the delta lobe. Laterally, starting from 17 m position

towards the east, we observed high-amplitude dipping oblique tangential reflectors. At about 22 m and 25 m position, the radar reflections are chaotic. Between 0.4 m and 1.2 m thick, we observed a package of high-amplitude dipping prograding reflection patterns that are oblique parallel until about 17 m. Small-scale undulations and laterally continuous basal planar beds are observed in the deeper parts of the GPR data (Figure 4.13).

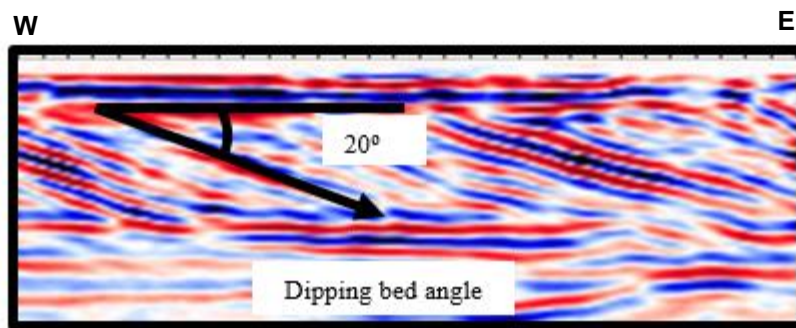


Figure 4.12. The dip is interpreted to be in the general downstream direction with a dip angle of 20°.

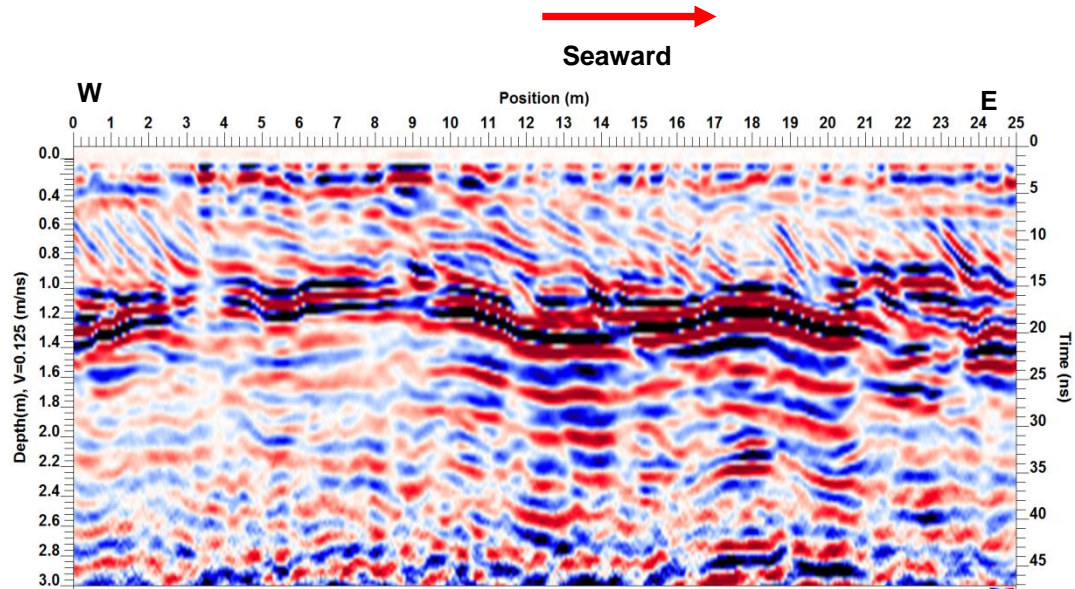


Figure 4.13. GPR image shows the progradational unit mouth bar with a dip angle of 20° deposited by friction-dominated river flow. The laterally continuous basal planar bed at the bottom of the figure is interpreted to be deposited in an inertia-dominated river mouth during a flood event.

4.6.4 Interpretation

The progradational mouth bar is characterized by large single foresets interpreted as friction-dominated. The oblique, high-amplitude, and continuous reflections suggests a progradational unit mouth bar with large single foresets. Convex upward GPR reflections found between 18 m to 19 m in a lateral position on the radargram are interpreted to be unit bars. The lateral planar beds are interpreted to be deposited in an inertia- dominated river mouth during a flood event, similar to those described by Martinsen et al. (1990).

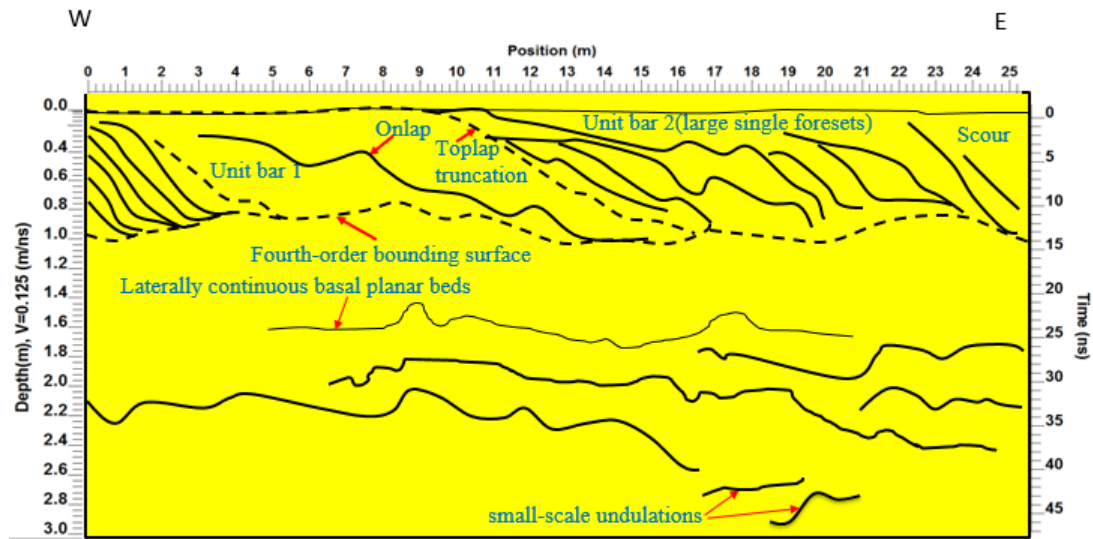


Figure 4.14. GPR image shows the progradational unit mouth bar with a dip angle of 20 degrees deposited by friction-dominated river flow. The laterally continuous basal-planar bed at the bottom of the figure is interpreted to be deposited in an inertia-dominated

4.6.5 Observation

The last example shows a strike-view across the bar. The GPR profile shows a prominent concave up lensoid-shaped reflection that extends across the survey (Figure. 4.16). The reflection truncates high-amplitude, horizontal and continuous reflections underneath it. Above the truncation surface are inclined, high-amplitude, steep dip (12° – 15°), and continuous reflections. The lower-bounding surface reflection is described as high-amplitude, and continuous. Signal attenuation was observed at 2.4 m where reflections start to fade.

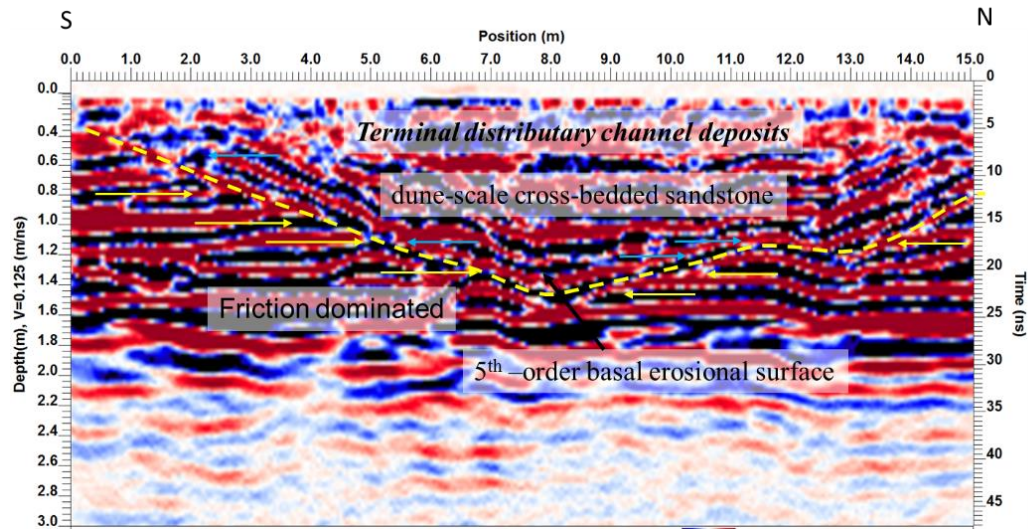


Figure 4.15. GPR image in strike-direction. It displays a terminal distributary channel deposit with a depth of 1.5 m.

4.6.6 Interpretation

The concave-up reflection is interpreted as a terminal distributary channel with a relief of 1.5 m. The channel is characterized by a basal erosional surface and occurs at the upper part of the coarsening upward succession. The channel is filled with the large-scale foresets (dipping reflections), that represent the unit mouth bar deposits.

4.7 3D GPR interpretation

4.7.1 Observation

We observed GPR reflection patterns on the west and the north sides of the 3D volume (Figure 4.16). Progradational reflection patterns that are dipping towards the east are

clearly imaged on the north side of the 3D volume. The dimension of the set thickness can be estimated from the 3D cube. A continuous and high-amplitude reflection horizon along the north side of the volume was observed at a depth of about 1.25 m. This reflection was also observed on the west side of the volume. The 3D volume shows the reflection pattern traced though the whole 3D volume. On the west side of the 3D volume, we observed a continuous and prominent concave up lensoid-shaped reflection.

4.7.2 Interpretation

From the 3D GPR volume, we interpreted the large single foreset on the north side of the volume to be a progradational unit mouth bar that prograding east. This is consistent with the result by Li et al. (2010) that the Ferron delta prograded east and north-east. At the intersection of the north and the west side of the volume, we estimated a 1.25 m thick terminal distributary channel fill. The decrease in the cross-set thickness from west to east suggests a gradual thinning downstream. The preserved thickness of the channel fill (~ 1.25 m) suggests a channel depth of about 1.6 m. The lower range of channel depth from the preserved thickness may indicate that the upper part of the channel fill is top truncated. The individual reflections in the GPR section most probably represent 2nd-order bounding surfaces (Miall, 1985).

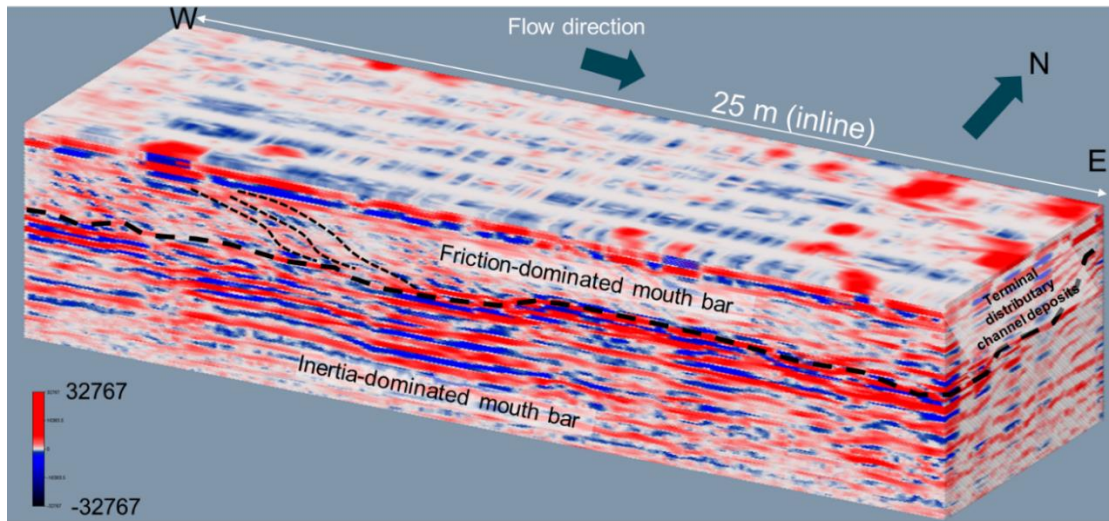


Figure 4.16. GPR image in strike-direction. It displays a terminal distributary channel deposit with a depth of 1.25 m.

Figure 4.17 displays a vertically stretched 3D GPR image of a channel in strike direction. The strike direction cuts the 3D volume and reveals the details of the channel shape and base. The upper portion of the 3D volume is characterized by high amplitude reflections, which indicated significant stratigraphic variation. Lateral migration surfaces were observed and channel-margin reflections indicate the dip angle of the channel. The sub-parallel and horizontal reflections are interpreted as laterally continuous basal planar beds. High-amplitude radar surfaces were observed in the strike and dip directions.

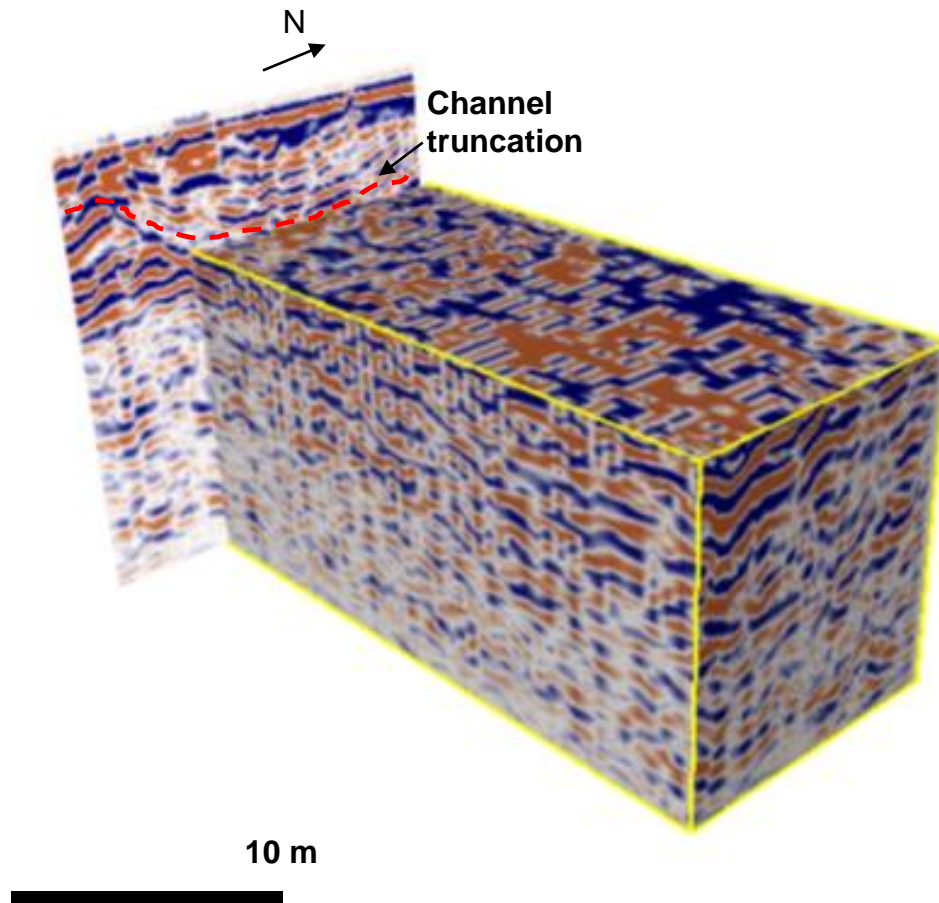


Figure 4.17. 3D-GPR volume showing the strike direction cuts the 3D volume and reveals the details of the channel shape and base displays a terminal distributary channel deposit with a depth of 1.25 m.

Figure 4.18 shows the continuity of the GPR lines in the dip (W-E) and strike direction (S-N). The shape of the high amplitude reflector at 1.25 m as observed in the dip oriented profile m is not flat and continuous. The water table is often flat and follows the trend of the surface and this is not observed in this area of study. The bottom of the channel is also characterized by a basal erosional surface.

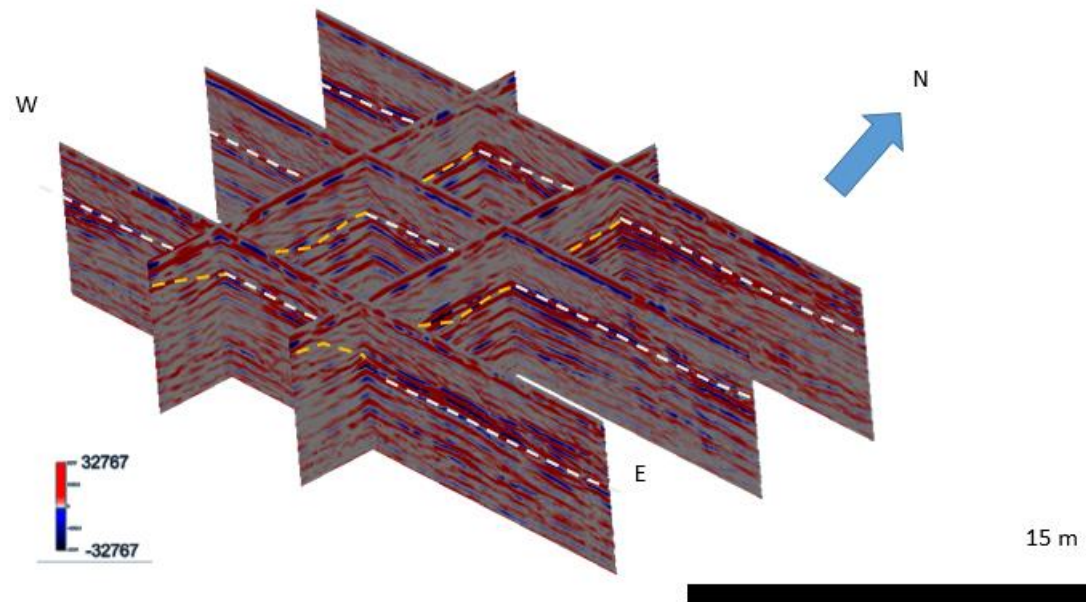


Figure 4.18. Fence diagram of the 3D GPR volume showing the continuity of the bottom of the channel in the strike direction and the erosional boundary.

We compared the vertical section to the depth slice to demonstrate the main features in 3D.

A horizontal depth slice through 3D-GPR volume at a depth of 0.4 m shows the foreset ribs, consistent with the sedimentological interpretation (Figure 4.19).

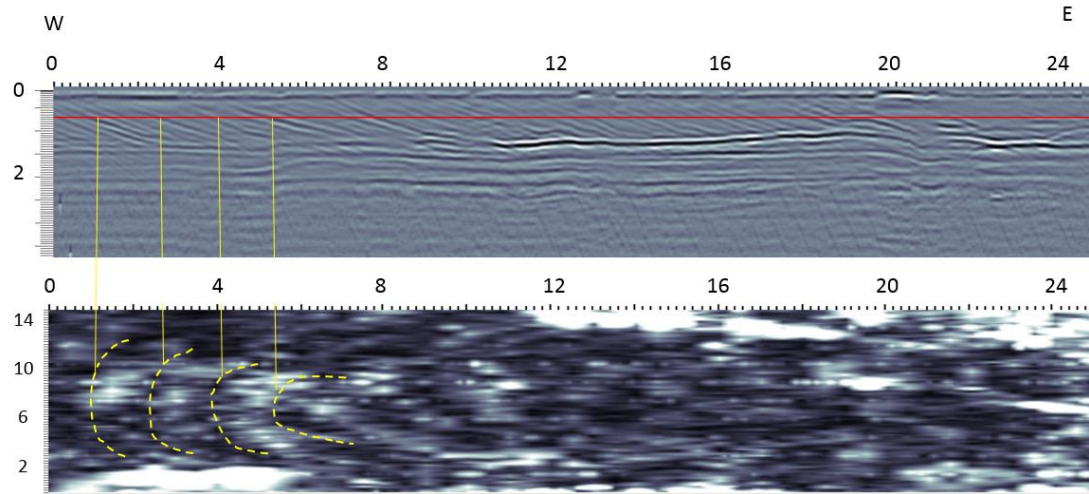


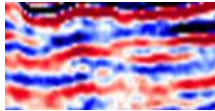
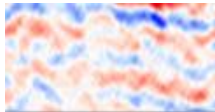


Figure 4.19. Amplitude depth slice at 0.4 m of the 3D-GPR data. The radius of curvature of the ribs are observed with an interpreted width of 9 m.

4.8 Discussion

Radar facies were observed based on the reflection amplitude and the configuration. Similar radar facies were reported by Akinpelu (2010). The facies description and the associated architectural elements are summarized in Table 4.2.

Table 4.2.Facies description and the associated architectural elements

Radar Facies		Architectural Elements	Facies Description
High-amplitude concave up reflections cut into underlying horizontal reflections		Channel cut into the underlying flat	Terminal distributary channel filled with distributary mouth bars
High-amplitude prograding reflections with dip angle between 18 to 20°		Progradational unit mouth bar	Progradational unit mouth bar with a dip angle between 18 to 20° deposited by friction-dominated river flow.
High-amplitude, horizontal, and continuous reflections		Basal planar bed	The laterally continuous basal planar bed deposited in an inertia-dominated river
Low-amplitude wavy, chaotic, sub-parallel, and undulating reflections		Basal planar bed	The laterally continuous basal planar bed deposited in an inertia-dominated river

A simple schematic depositional model based on the GPR interpretation is constructed. The model demonstrates three significant depositional sequences that include eastward-migrating distributary mouth bars with a dip angle of between 20° to 30°. Below the mouth bars are the low-angle, undulating basal planar beds.

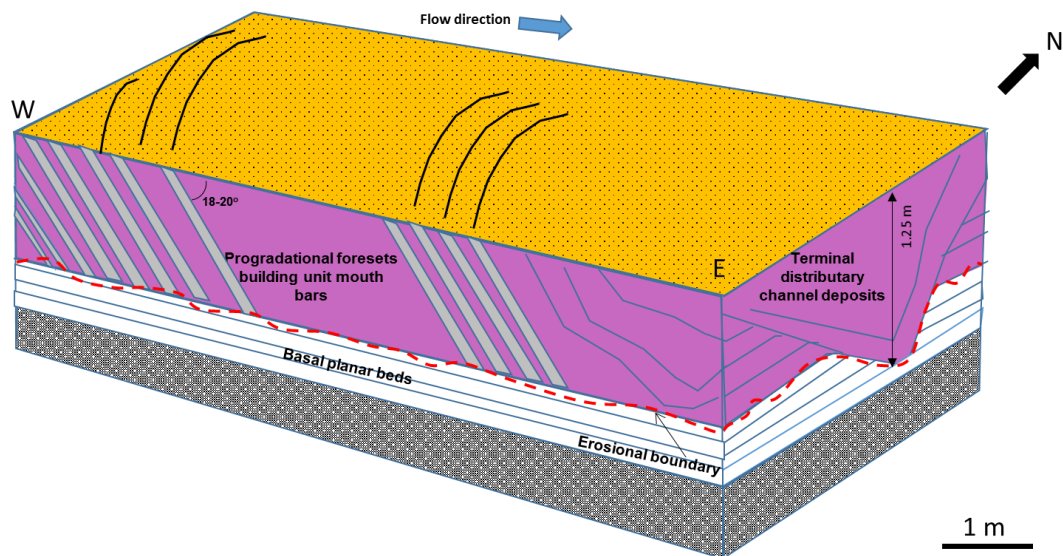


Figure 4.20. Schematic diagram of a depositional model showing 3D reconstruction of the distributary mouth bars and terminal distributary channels derived from GPR vertical and amplitude depth section.

4.9 Conclusions

We have used 3D GPR to image the internal structure of shallow terminal distributary mouth bars and distributary channel in the Cretaceous Ferron Sandstone. The thickness of the individual cross-sets ranges between 8 and 12 cm (measured from the 2D GPR section). The decrease in the cross-set thickness from west to east suggests a gradual thinning downstream. Interpretation of 2D- and 3D-radar profiles described the heterogeneity of the terminal distributary channel and suggested a complicated depositional environment that exhibits various degrees of spatial variability. Three major

radar facies were observed in this study including terminal distributary channel filled with distributary mouth bars, progradational unit mouth bar with a dip angle of approximately 20°, and laterally continuous basal planar bed deposited in an inertia-dominated river. The 3D-GPR image showed a terminal distributary channel fill with a thickness of 1.25 m. The preserved thickness of the channel fill (~ 1.25 m) also gives a channel depth of about 1.6 m, which conforms to the depth calculation from cross-set thickness. The GPR radargrams were not only capable of imaging the 3D architecture of individual unit bars, but also identified two significant proximal delta-front facies: upper friction-dominated dune-scale cross beds and bar-scale large foresets from lower inertia-dominated basal planar beds. Useful information like the cross bedding direction shown on GPR images can help to predict the maximum directional permeability. Unlike a 2D outcrop, GPR reveals true accretion directions. This helps to define mouth bar growth pattern (downstream, upstream or lateral). Horizontal depth slices obtained from the 3D GPR data help to define the 3D element of the distributary mouth bars. Depositional sequences identified from radar facies were used in reconstructing the 3D geometry of the mouth bars. The 3D-depositional model suggests the direction of the terminal distributary channel. GPR-data analysis can facilitate or improve mapping outcrop heterogeneity and help define 3D geometry of sand bodies. The reported radar facies provide a reference for other future studies to compare radar reflection pattern with architectural elements in similar outcrops.

Acknowledgements

We would like to thank the Allied Geophysical Lab team, especially Long Huang, for acquiring the GPR data and supporting the investigation. We are thankful to Proma Bhattacharya for fruitful discussions.

References

- Ahmed, S., J. P. Bhattacharya, D.E. Garza, Y. Li, 2014, Facies Architecture and Stratigraphic Evolution of a River-Dominated Delta Front, Turonian Ferron Sandstone, Utah: *Journal of Sedimentological Research*, 84, 97-121.
- Aitken, J. A, 2008, Exploring Maya ruins in Belize, Central America using ground-penetrating radar (GPR): M.S. thesis, University of Calgary.
- Akinpelu, O, 2010, Ground Penetrating Radar Imaging of Ancient Clastic Deposits: A Tool for three-dimensional Outcrop Studies: Ph.D. Thesis, University of Toronto.
- Asprion, U., and T. Aigner, 1997, Aquifer architecture analysis using ground-penetrating radar: Triassic and quaternary examples: *Environmental Geology*, 31, 66–75
- Bakker, M. A. J., D. Maljers, and H. J. T, Weerts, 2007, Ground-penetrating radar profiling on embanked floodplains: *Netherlands Journal of Geosciences*, 86, 55–61.
- Barton, M. D., 1994, Outcrop characterization of architecture and permeability structure in fluvial-deltaic sandstones, Cretaceous Ferron Sandstone, Utah: Ph.D. dissertation,

University of Texas at Austin.

Beard, D. C., and P. K. Weyl, 1973, Influence of Texture on Porosity and Permeability of Unconsolidated Sand: AAPG Bulletin, 57, 349-369.

Beres, M., A. Green, P. Huggenburger, and H. Horstmeyer, 1995, Mapping the architecture of glaciofluvial sediments with three dimensional georadar: Geology, 23, 1087–1090.

Bhattacharya, J. P., and R. S. Tye, 2004, Searching for modern Ferron analogs and application to subsurface interpretation in Regional to Wellbore Analog for Fluvial–Deltaic Reservoir Modelling: The Ferron Sandstone of Utah *in* T.C. Chidsey, R. D. Adams, and T. H. Morris, eds., Studies in Geology: American Association of Petroleum Geologists, 50: 39–57.

Bhattacharya, J.P., 2006, Deltas, *in* R. G. Walker and H. Posamentier, eds., Facies Models revisited: SEPM Special Publication, 84, 237-292.

Bhattacharya, P., J. P. Bhattacharya, and S. D. Khan, 2013, 3-D facies architecture, grain size variability and paleohydrology study of point bar deposits by integrating file data with airborne LiDAR and GPR in Ferron sandstone, Hanksville, Utah: Presented at AAPG.

Bridge, J.S., 2003, Rivers and Floodplains: Blackwells.

Chidsey, T. C., R. D. Adams, and T. H. Morris, 2004, Regional to Wellbore Analog for Fluvial–Deltaic Reservoir Modelling: The Ferron Sandstone of Utah: American Association of Petroleum Geologists.

Coleman, J., and D. B. Prior, 1982, Deltaic environments, *in* P. A. Scholle and D. Spearing,

eds., Sandstone depositional environments: AAPG Memoir, 31,139-178.

Corbeanu, R.M., K. Soegaard, R. B. Szerbiak, J. B. Thurmond, G. A. McMechan, D. Wang, S. H. Snelgrove, C.B. Forster, and A. Menitove, 2001, Detailed internal architecture of fluvial channel sandstone determined from outcrop and 3-D ground penetrating radar: Example from mid-Cretaceous Ferron Sandstone, east-central Utah: American Association of Petroleum Geologists Bulletin, 85, 1583–1608.

Mukherjee, D., S. D. Khan, and C. Sullivan, 2012, Upper Albian rudist buildups of the Edwards Formation in central Texas: A GPR-assisted reservoir analog study: Journal of Sedimentary Geology, 247-248, 71-81.

Flint, S. S., and D. Bryant, 1993, The geological modeling of hydrocarbon reservoirs and outcrop analogs: Blackwell.

Gani, M.R., and J. P. Bhattacharya, 2007, Basic Building Blocks and Process Variability of a Cretaceous Delta: Internal Facies Architecture Reveals a More Dynamic Interaction of River, Wave, and Tidal Processes Than Is Indicated by External Shape: Journal of Sedimentary Research, 77, 284-302.

Gloyn, R. W., and S. N. Sommer, 1993. Exploration for coalbed methane gains momentum in Uinta Basin. Utah Geological Survey: Oil & Gas Journal, Exploration, 73-76.

Hale, L. A., 1972, Depositional history of the Ferron Formation, central Utah, in J. L. Baer and E. Callaghan, eds., Plateau-basin and range transition zone: Utah Geological Association Publication, 2,115–138.

Hale, L. A., and R. F. Van DeGraff, 1964, Cretaceous stratigraphy and facies patterns - northeastern Utah and adjacent areas: Intermountain Association of Petroleum Geologists, 13th Annual Field Conference Guidebook, 115–138.

- Hill, R.B., 1982, Depositional environments of the Upper Cretaceous Ferron Sandstone south of Notom, Wayne County, Utah: Brigham Young University Geology Studies, 29, 59-83.
- Howell, J. A., A.W. Martinius, and T. R. Good, 2014, The application of outcrop analogues in geological modeling: A Review, present status and future outlook, *in* A. W. Martinius, J. A. Howell, and T. R. Good, eds., Sediment body geometry and heterogeneity: Analogue studies for modeling the subsurface: The Geological Society, 387,1-25.
- Jarrard, R. D., C. H. Sondergeld, M. A. Chan, and S. N. Erickson, 2004, Petrophysics of the Cretaceous Ferron Sandstone, Central Utah: AAPG Studies in Geology 50, 227-249.
- Jordan, D. W., and W. A. Pryor, 1992, Hierarchical levels of heterogeneity in a Mississippi River meander belt and application to reservoir systems: AAPG Bulletin, 76, 1601-1624.
- Khan, S. D., E. Heggy, and J. Fernandez, 2007, Mapping exposed and buried lava flows using synthetic aperture radar and ground-penetrating radar in Craters of the Moon lava field: Geophysics, 72, 161–174.
- Knox, P. R., and M. D. Barton, 1999, Predicting interwell heterogeneity in fluvial-deltaic reservoirs - effects of progressive architecture variation through a depositional cycle from outcrop and subsurface observations, *in* R. Schatzinger and J. Jordan, eds., Reservoir characterization-recent advances: AAPG Memoir 71, 57-72.
- Lee, K., M. Tomasso, W. A. Ambrose, and R. Bouroullec, 2007, Integration of GPR with stratigraphic and lidar data to investigate behind-the-outcrop 3D geometry of a tidal

channel reservoir analog, upper Ferron Sandstone, Utah: *The Leading Edge*, 26, 994-998.

Li, W., J. P. Bhattacharya, and C. Campbell, 2010, Temporal evolution of fluvial style within a compound incised valley, the Ferron Notom Delta, Henry Mountains Region, Utah: *Journal of Sedimentary Research*, 80, 529–549.

Li, W., J. P. Bhattacharya, Y. Zhu, D. Garza, and E. Blankenship, 2011, Evaluating delta asymmetry using 3d facies architecture and ichnological analysis, Ferron Notom Delta, Capital Reef Utah, USA: *Sedimentology*, 58, 478–507.

Li, Y., 2013, Facies Architectural Study of Incised Valleys, Distributary Channels, and Mouth Bars in the Cretaceous Ferron Notom Delta, Southern Central Utah, USA: Ph.D. Thesis, University of Houston.

Li, Y., and J. P. Bhattacharya, 2013, Facies Architectural Study of a Stepped, Forced Regressive Compound Incised Valley System in the Ferron Notom Delta, Southern Utah: *Journal of Sedimentary Research*, 83, 206-225

Li, Y., and J. P. Bhattacharya, 2014, Facies Architecture of asymmetrical branching distributary channels: Cretaceous Ferron Sandstone, Utah, USA: *Sedimentology*, 61, 1452-1483.

Li, Y., J. P. Bhattacharya, S. Ahmed, and D. Garza, 2014, Facies-Architecture Study of A Stepped, Forced Regressive Compound Incised Valley In the Ferron Notom Delta, Southern Central Utah, USA: AAPG.

Li, Y., Bhattacharya, J.P., Garza, D., Ahmed, S., *in revision*, Facies architecture and paleogeography of a symmetrical, wave-influenced valley-fed delta in the

Cretaceous Ferron Sandstone, Utah, USA. *submitted to Sedimentary Geology.*

Martinsen, O.J., 1990, Fluvial, inertia-dominated deltaic deposition in the Namurian (Carboniferous) of northern England. *Sedimentology* 37, 1099–1113.

McMechan, G. A., G. C. Gaynor, and R. B. Szerbiak, 1997, Use of ground-penetrating radar for 3-D stratigraphic characterization of clastic reservoir analogs: Geophysics, 62, 786–796.

Miall, A.D., 1985, Architectural element analysis: a new method of facies analysis applied to fluvial deposits. *Earth Science Review*, 22, 261–308.

Moldoveanu, M., R. R. Stewart, J. Aitken, and E. Gallant, 2003, 3D ground penetrating radar over ice at Bowness Park, Calgary: CREWES Research Report, 15.

Moore, J., A. Taylor, C. Johnson, B. D. Ritts, and R. Archer, 2012, Facies Analysis, Reservoir Characterization, and LIDAR Modeling of an Eocene Lacustrine Delta, Green River Formation, Southwest Uinta Basin, Utah, *in* O.W. Baganz, Y. Bartov, K. M. Bohacs, and D. Nummedal, eds., Lacustrine sandstone reservoirs and hydrocarbon systems: AAPG Memoir, 95, 183-208.

Morse, D. G., 1994, Siliciclastic reservoir rocks, *in* L.B. Magoon, and W. G. Dow, eds., The petroleum system; from source to trap: The American Association Petroleum Geologists Memoir, 60, 121-139.

Peterson, F., and R. T. Ryder, 1975, Cretaceous rocks in the Henry Mountains Region, Utah and their relation to neighboring regions, *in* J.E. Fassett, and S. A. Wengerd, eds., Canyonlands Country: Four Corners Geological Society, 8th Field Conference, Guidebook, 167–189.

- Pryor, W. A., 1973, Permeability-porosity patterns and variations in some Holocene sand bodies: AAPG Bulletin, 57, 162-189.
- Ryer, T.A., and P. B. Anderson, 2004, Facies of the Ferron Sandstone, East-Central Utah in Regional to Wellbore Analog for Fluvial– Deltaic Reservoir Modelling: The Ferron Sandstone of Utah, *in* T.C. Chidsey, R. D. Adams, and T. H. Morris, eds., Studies in Geology: American Association of Petroleum Geologists, 50, 59–78.
- Szerbiak, R. B., G. A. McMechan, R. M. Corbeanu, C. Forster, and S. H. Snelgrove, 2001, 3-D characterization of a clastic reservoir analog: From 3-D GPR to a 3-D fluid permeability model: Geophysics, 66, 1026–1037.
- K, R. S., G. A. McMechan, C. Forster, S. H. Snelgrove, 2006, Electrical and petrophysical modeling of Ferron Sandstone data: Geophysics, 70, P. G197–G210,
- Tatum, D.I., and J. Francke, 2012, Constructing hydrocarbon reservoir analogues of Aeolian systems using ground penetrating radar: Journal of Applied Geophysics, 81, 21-28
- Turner, B.R., and G. N. Tester, 2006, The Table Rocks sandstone: a fluvial, friction-dominated lobate mouth bar sandbody in the Westphalian B Coal Measures, NE England: Sedimentary Geology, 190, 97-119.
- Tye, R. S., J. P. Bhattacharya, J. A. Loring, S. T., Sindelar, D. G. , Knock, D. D., Puls, .., and R. A. Levinson, 1999, Geology and stratigraphy of fluvio-deltaic deposits in the Ivishak Formation: applications for development of Prudhoe Bay Field, Alaska: AAPG bulletin, 83, 1588-1623.
- Ullah, M. S., J. P. Bhattacharya, and W. R. Dupre, 2015, Confluence Scours Versus Incised Valleys: Examples From the Cretaceous Ferron Notom Delta, Southeastern Utah,

U.S.A: Journal of Sedimentary Research, 85, 445-458.

Wright, L.D., 1977, Sediment transport and deposition at river mouths: A synthesis: Geological society of America Bulletin, 88, 857-868.

Wu, C., J. P. Bhattacharya, and M.S. Ullah, 2015, Paleohydrology and 3D Facies Architecture of Ancient Point Bars, Ferron Sandstone, Notom Delta, South-Central Utah, USA: Journal of Sedimentary Research, 85, 399-418.

Zhu Y., J.P. Bhattacharya, W. Li, T. J., Lapen, B. R. Jicha, and B. S. Singer, 2012, Milankovitch-scale sequence stratigraphy and stepped forced regressions of the Turonian Ferron Notom deltaic complex, south-central Utah, U.S.A.: Journal of Sedimentary Research, 82, 723-746.

5 3D GPR INVESTIGATION AT BARRINGER (METEOR) CRATER, ARIZONA

Abstract

Ground penetrating radar (GPR) has been used as an effective tool for variety of near surface geophysical investigations including lunar surface modeling (e.g., Stewart, 2003; Khan et al., 2007; Rowell, et al., 2010, Roy and Stewart, 2012; Turolski, 2012). In this work, we explore GPR's usefulness to estimate the alluvium thickness and to directly characterize the ejecta elements of a well-known meteorite impact crater at Barringer (Meteor) Crater, Arizona. A 250-MHz GPR system was used to investigate the GPR signature of the first 5 m depth in the area where small iron meteorites and small broken fragments of iron oxide or iron shale may reside. One 100-m by 4.5 m GPR grid (northeast-southwest direction) was carried out in southeast flank of the Meteor Crater. Two other grids of 4.5 by 10 m were acquired in northwest-southeast direction. Hyperbola matching from the acquired field data yields a velocity of 0.102 m/ns. This value is comparable to previously published work (Grant and Schultz, 1991). The results obtained show a good penetration depth of 4.5 m despite the acquisition challenges with the brecciated surface. Variations in the signal intensity observed in the GPR images may be due to variability in antenna and ground coupling. Almost horizontal and high-amplitude reflectors were observed approximately at 0.7 m depth which we interpret as the base of the recent alluvium layer. This layer is interpreted as a probable change from the alluvium film to the underlying ejected materials. The alluvium thickness (0.7 m) is consistent with the drill-hole database. Several diffraction hyperbolas related to point reflectors (most

likely some fragments or blocks embedded in the ejecta blanket) have been observed at about 2 m depth in grid 8 and grid 9 (northwest-southeast) in the cross sections and the depth slices. This 3D GPR result indicates that a shallow high-resolution imaging of the complex near-surface at the Meteor Crater is possible. The results demonstrate 3D GPR images can be used to directly describe the geological information of Meteor Crater within a depth of 5 m.

5.1 Introduction

Ground-penetrating radar (GPR) studies can provide insights into the subsurface electrical properties, layer thickness, and rock distribution in the near surface. Because of the non-invasiveness, quick, and relatively cheap, GPR has been used in various methods including investigating the planetary analogs. Previous investigations of the Mars analog sites (e.g., Maxwell, 2002, Khan et al., 2007) have shown the significant capability of GPR to provide data about the subsurface that can be used to constrain the geologic setting. Impact cratering is a major event in surface modification and craters and their ejecta are the most dominant elements of the lunar and Martian surfaces (Russell et al., 2013).

Russell et al. 2013 reported the dielectric constant of alluvium is between 4 and 5.3 and the corresponding radar velocity is 0.13 m/ns – 0.15 m/ns. Grant et al. (1991) found the alluvium radar velocity is 0.11 m/ns and the ejecta radar velocity to be 0.145 m/ns. In this chapter, we explore GPR's applicability to image the near surface area at the flank of the

Meteor Crater up to 5 m. The study is aimed to estimate the alluvium thickness and to directly characterize and observe the distribution of the ejecta elements of a well-known meteorite impact crater at Barringer (Meteor) Crater, Arizona.

5.2 Survey location and geological setting

Barringer Meteor Crater is located near Winslow, Arizona and is known as the world's best preserved meteorite impact on the Earth's surface (Figure 5.1) (Roy and Stewart, 2012). The site is a result of a collision between an asteroid traveling at 26,000 mph and the Earth about 50,000 years ago (Fredericks, 2012). The crater diameter is approximately 1.2 km (Kring, 2007) and its depth is about 180 m deep (Roy and Stewart, 2012). The reported water table is approximately 60 to 64 m from the bottom of the crater (Pilon and Grieve, 1991). The meteorites found in areas at the crater impact represent one of the scarcest materials and they provide the original material from where the entire Earth was formed. Meteorites are relatively expensive and are sought after by collectors (Figure 5.2).

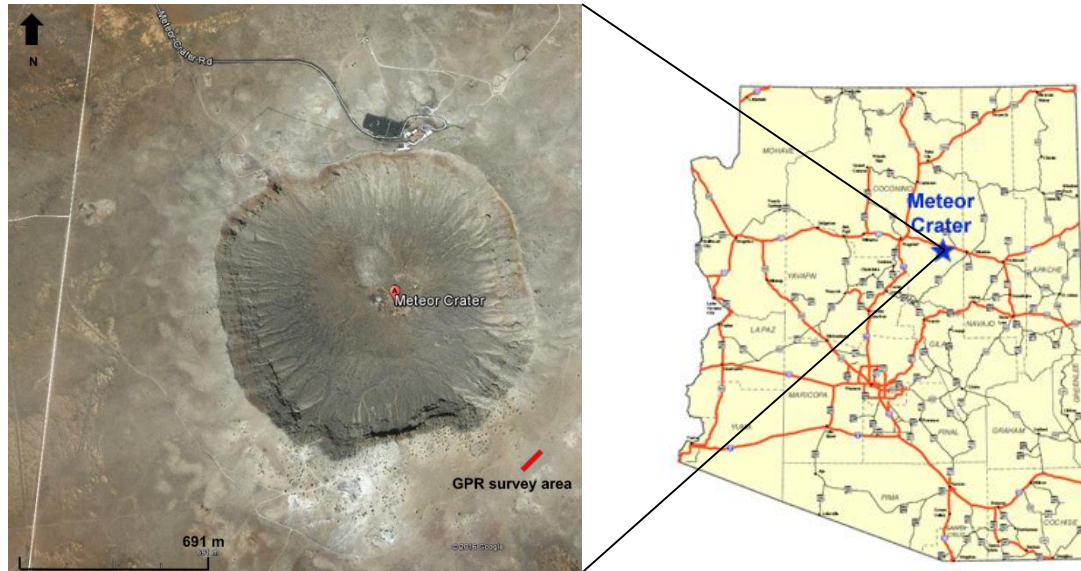


Figure 5.1. Google Earth photograph shows the Meteor Crater image. The location of the survey is marked by the red rectangular grid.



Figure 5.2. An example of the Canyon Diablo (Meteor Crater) meteorite (Photo: Robert R. Stewart)

The geologic map of the distribution of materials at the Meteor Crater is shown in Figure 5.3. The GPR grid indicated by the red rectangle shows that the study area is mainly composed of recent Alluvium. The geologic cross section is shown in Figure 5.4. The main geological formation of the area are Moenkopi Formation is the top layer. It is characterized by pale to reddish brown and very fine-grain sandstone. The underlying layer is Kaibab formation which is characterized by fossiliferous marine sandy dolomite, dolomitic limestone, and minor calcareous sandstone.

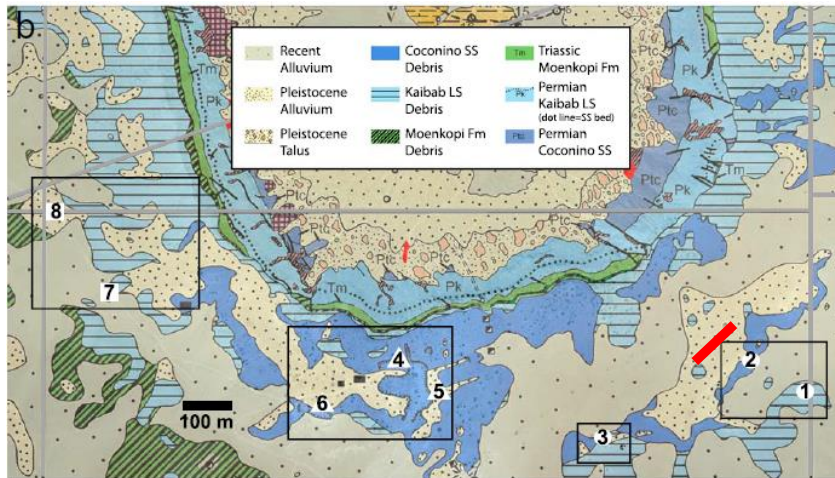


Figure 5.3. The geologic map of the distribution of materials at the Meteor Crater. Red rectangular grid marks the GPR survey area (Russell, 2013).

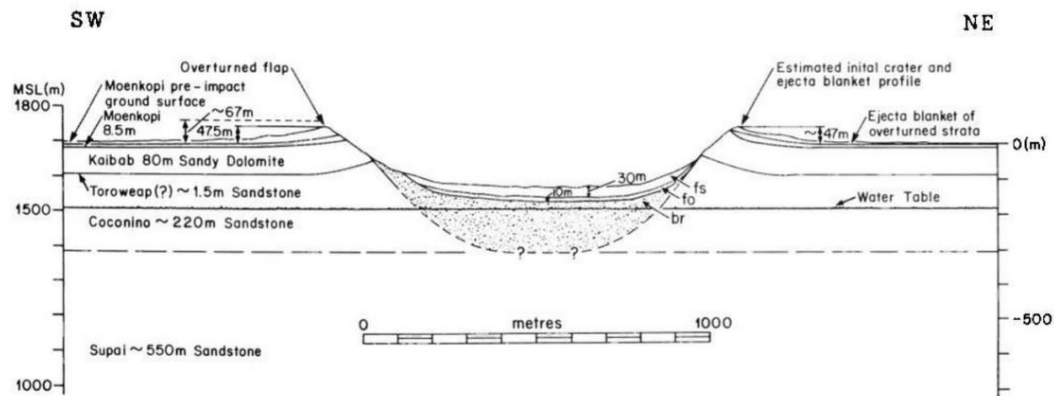


Figure 5.4. The geologic cross section of Meteor Crater (Pilon and Grieve, 1991).

5.3 Data acquisition

The survey area is characterized by rough terrain that causes the data acquisition to move slowly and is shown in Figure 5.5. The choice of the survey location was limited due to the strict regulation in conducting a survey at a specific area. GPR data were collected using Sensors & Software's 250 MHz Noggin SmartCart System. Three GPR grids were carried out in the southeast flank of the Meteor Crater as shown in Figure 5.6.

Grid 3 is in the northeast-southwest direction and grid 8, and grid 9 are in the northwest-southeast direction. The dimension of grid 3 is 100 m long and 4.5 wide. The size of grid 8 and grid 9 are 10 m long and 4.5 m wide. The line spacing is 0.5 m and the trace interval is 0.05 m.



Figure 5.5. A photograph shows the survey area with the Noggin Smart Cart 250 MHz in sight (Photo: Susan L. Green).

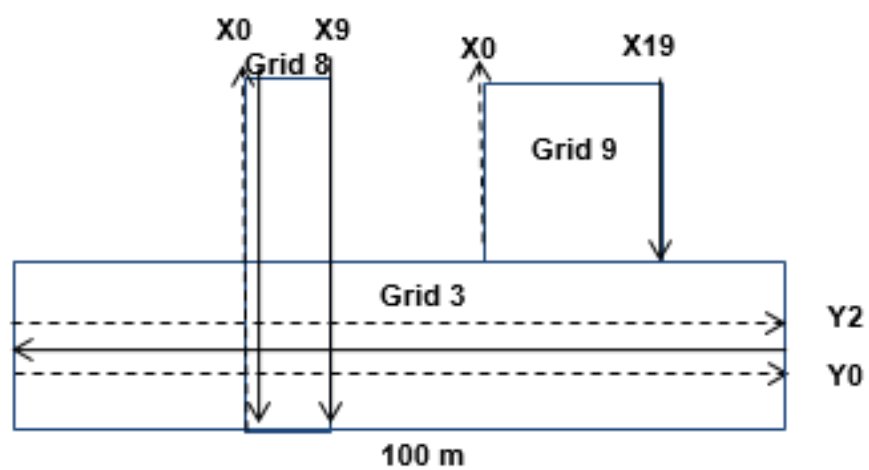


Figure 5.6. GPR survey grids at the Meteor Crater.

5.4 Results

The following sections detail the results of the data processing for grid 3, grid 8, and grid 9. The processing was undertaken using Sensors & Software processing package EKKOView Deluxe. The main steps in the standard data processing are time-zero correction, dewow, and spherical exponential gain (Ulriksen, 1982; La Fleeche et al., 1991; Fisher et al., 1992; Fisher et al., 1996).

5.4.1 Survey grid 3

A total of 10 GPR lines were acquired in grid 3 and each line was a 100 m long profile. The hyperbola matching over a distinct diffraction in grid 3 yielded a velocity of 0.102 m/ns as seen in Figure 5.7. The value is comparable to that of reported by Russell et al. (2013) which is approximately 0.110 m/ns. The calculated dielectric constant is 8.6 and the vertical resolution is 12 cm for this data.

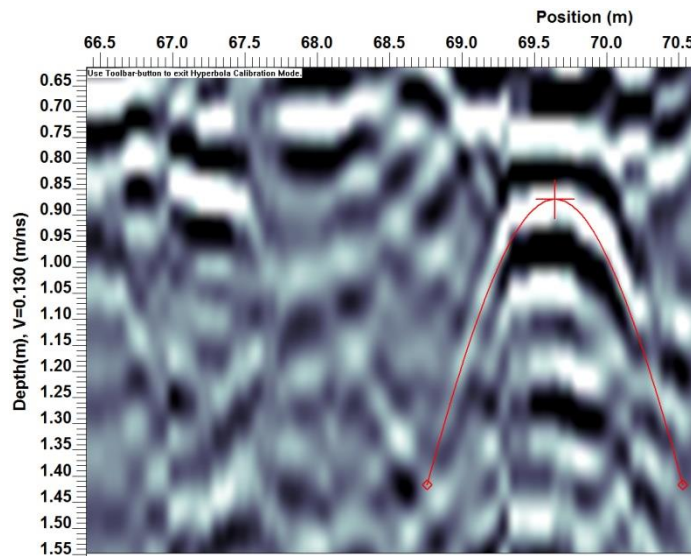


Figure 5.7. Hyperbola matching to extract radar velocity yields 0.102 m/ns.

Figure 5.8 shows an unmigrated GPR section of the 250 MHz data. The depth of penetration is approximately 4.5 m (shown by the dashed horizontal line) and the image quality is good. Distributed distinct anomalies characterized by high amplitude reflectors are marked by yellow circles in Figure 5.8. We interpreted the observed anomalies as ejecta materials which appear bright in GPR sections. Figure 5.9 shows a depth slice at 2 m shows a high amplitude area at about 72.5 m corresponding with the anomaly observed in Figure 5.8. Figure 5.10, Figure 5.11, Figure 5.12, and Figure 5.13 show the migrated GPR profile with varying velocities of 0.10, 0.11, 0.12, and 0.13 m/ns respectively. We observed variations in the signal intensity observed in the GPR images that may be due to variability in antenna and ground coupling.

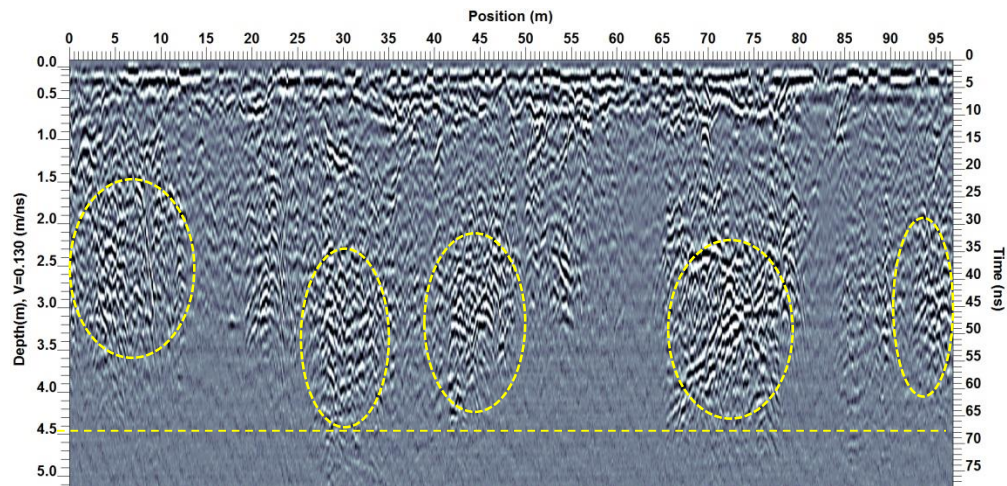


Figure 5.8. Unmigrated GPR profile (Line Y6).

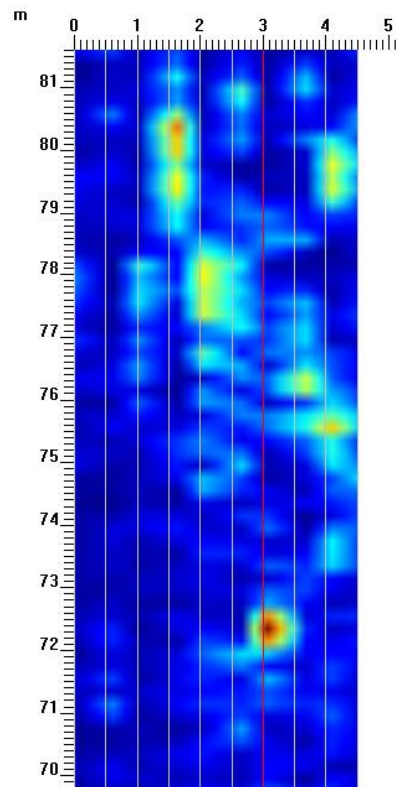


Figure 5.9. Depth slice of grid 3 at 2 m shows a high-amplitude area approximately at 72.5 m.

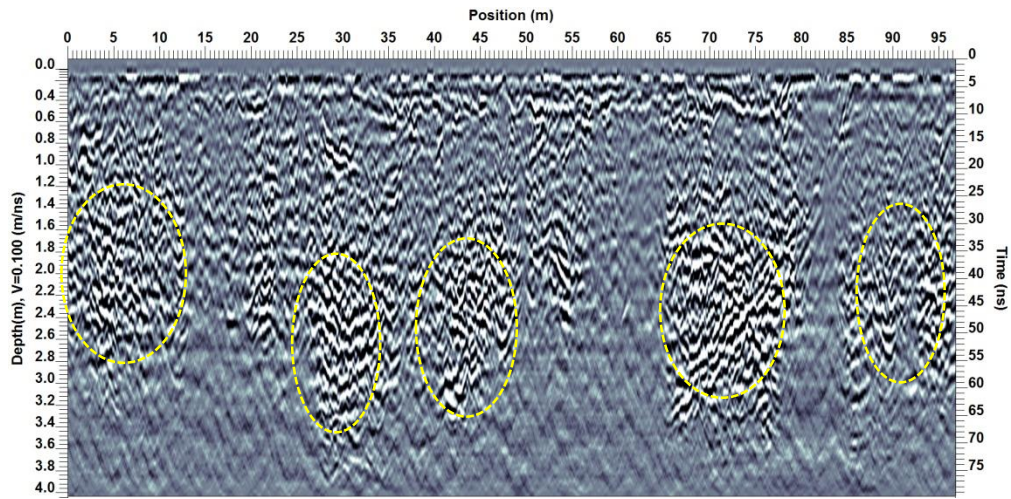


Figure 5.10. Migrated GPR profile with a velocity of 0.10 m/ns (Line Y6).

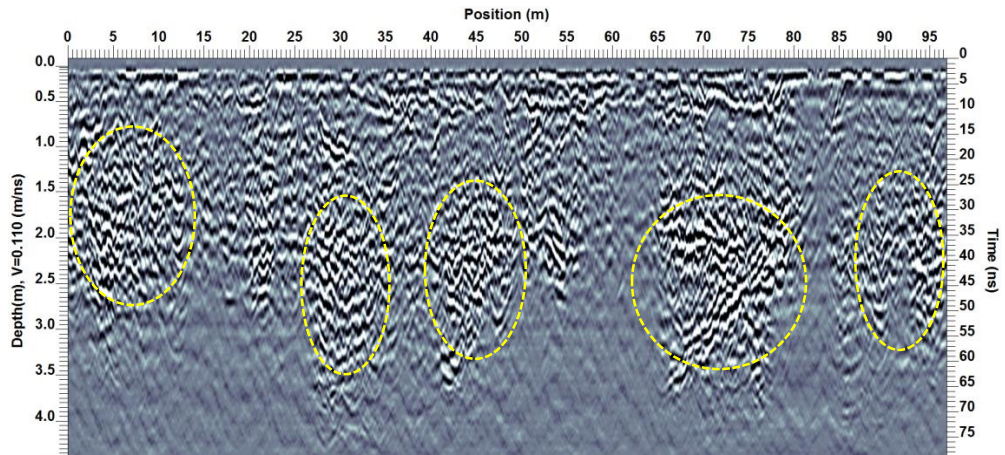


Figure 5.11. Migrated GPR profile with a velocity of 0.11 m/ns (Line Y6).

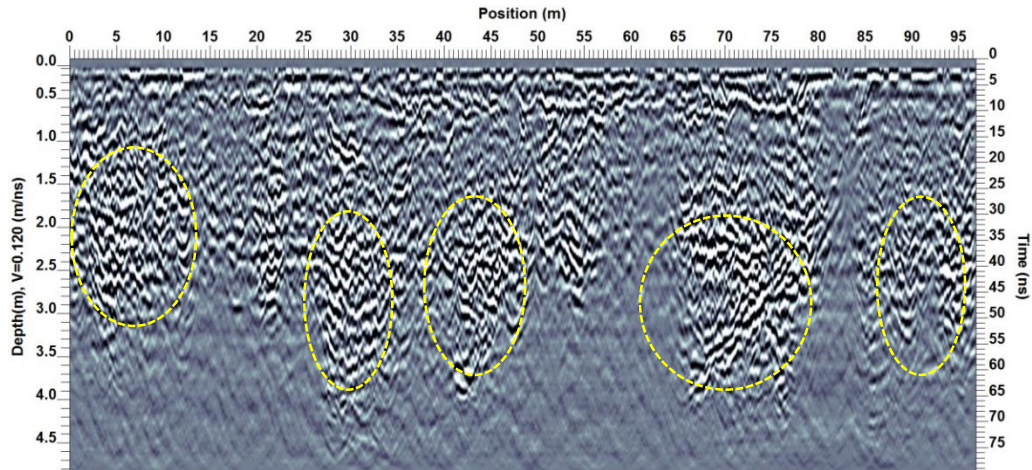


Figure 5.12. Migrated GPR profile with a velocity of 0.12 m/ns (Line Y6).

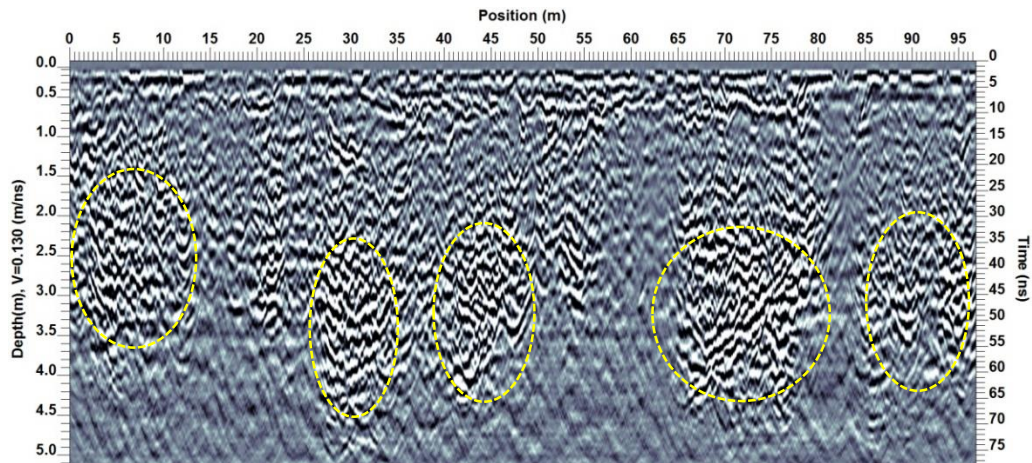


Figure 5.13. Migrated GPR profile with a velocity of 0.13 m/ns (Line Y6).

5.4.2 Survey grid 8

Survey grid 8 is perpendicular to the survey grid 3 line. We observe horizontal and high-amplitude reflectors approximately at 0.7 m depth which we interpret as recent alluvium marked by the yellow dashed lines as shown in Figure 5.14 and Figure 5.15. This layer is interpreted as a probable change from the alluvium film to the underlying ejecta materials. The alluvium thickness (0.7 m) is consistent with the drill-hole database (Roy and Stewart,

2012). Grant and Schultz (1991) reported the alluvium thickness is about 1-2 m. The anomalies marked by the yellow dashed circles in Figure 5.14 and Figure 5.15 and are interpreted as fragments.

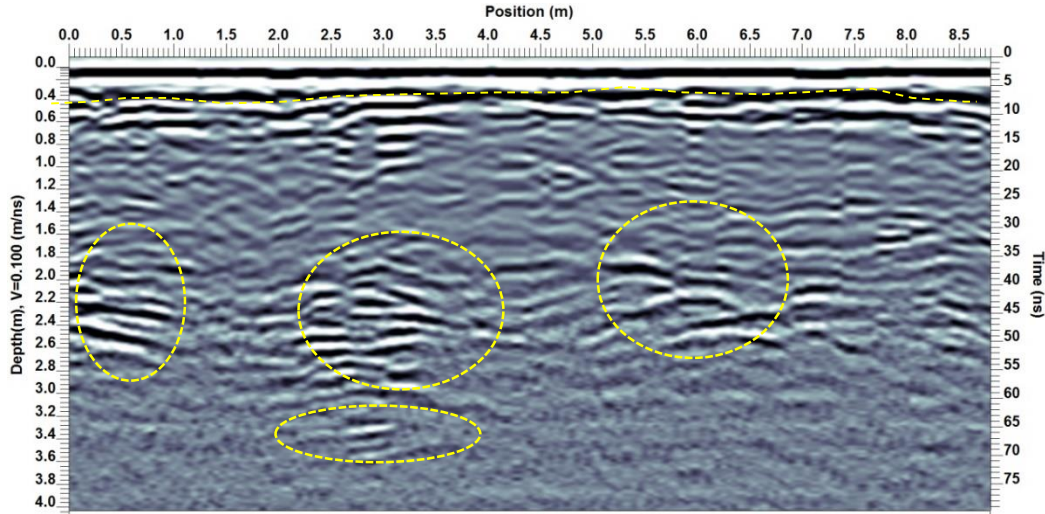


Figure 5.14. Unmigrated GPR profile shows various anomalies characterized by high amplitude reflectors at various locations marked by yellow dashed circles (Line X6).

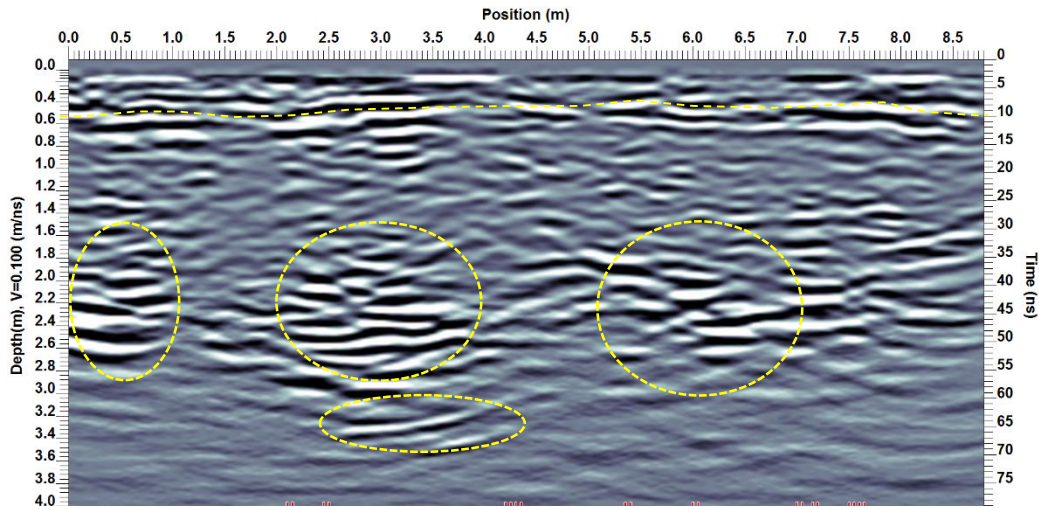


Figure 5.15. Migrated GPR profile with a velocity of 0.10 m/ns (Line X6) shows various anomalies characterized by high amplitude reflectors at various locations marked by yellow dashed circles (Line X6).

5.4.3 Survey grid 9

A total 20 GPR lines with 0.5 m spacing are acquired in grid 9. Several diffraction hyperbolas related to point reflectors (most likely some fragments or blocks embedded in the ejecta blanket) have been observed starting at a depth of 2 m marked by the yellow ellipsoid in Figure 5.16 (northwest-southeast). A hyperbola is observed at about 0.8 m depth as shown in the yellow ellipsoid. Figure 5.17 shows the migrated GPR profile with a velocity of 0.10 m/ns.

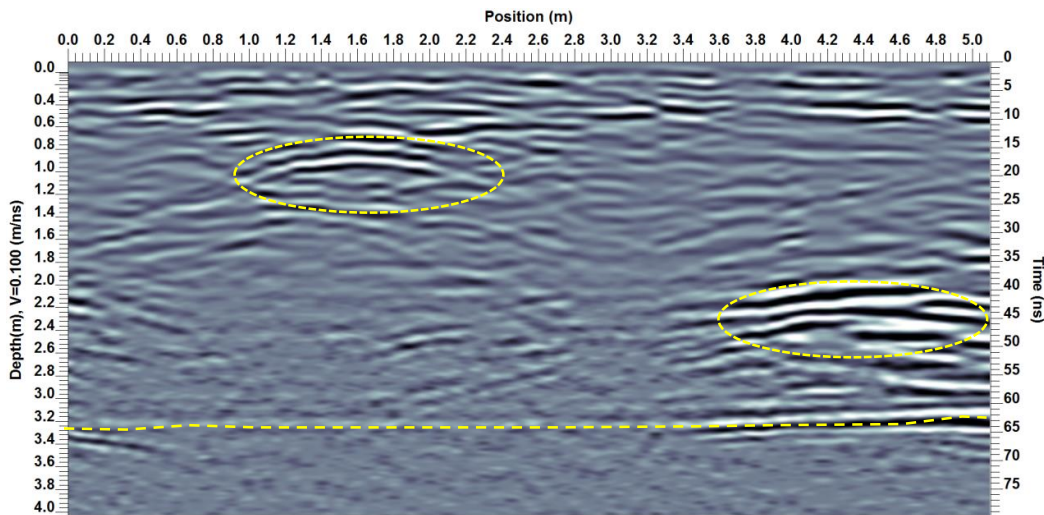


Figure 5.16. Unmigrated GPR profile (Line X4).

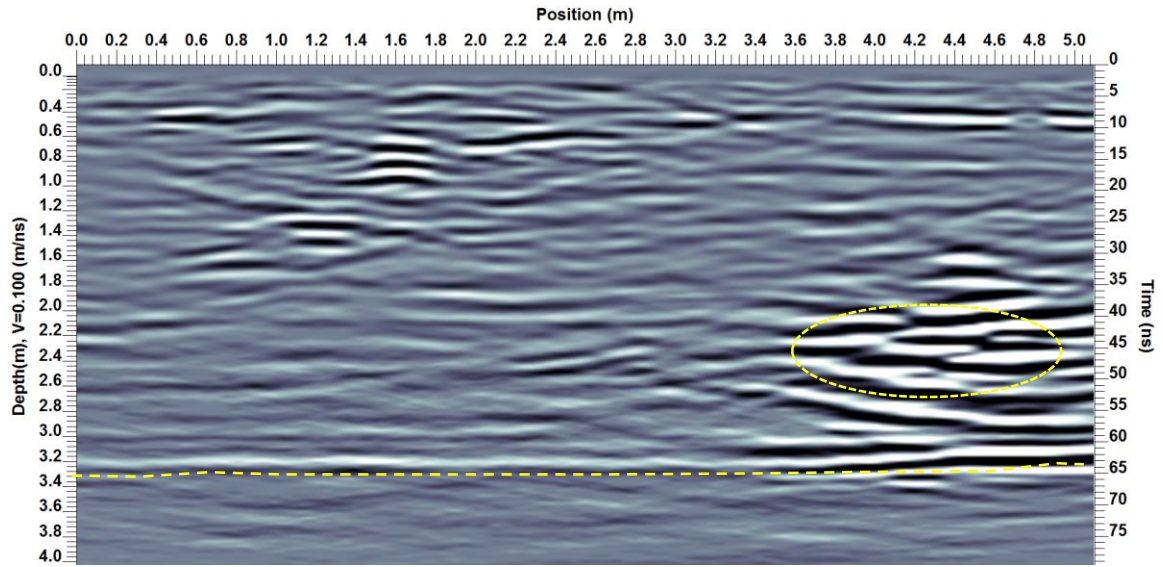


Figure 5.17. Migrated GPR profile with a velocity of 0.10 m/ns (Line X4).

We investigated the depth slice to observe the ejecta elements shown in Figure 5.17 and Figure 5.19. We observed a high-amplitude area at a depth interval of 2.38 m and 2.39 m in Figure 5.18 and Figure 5.19.

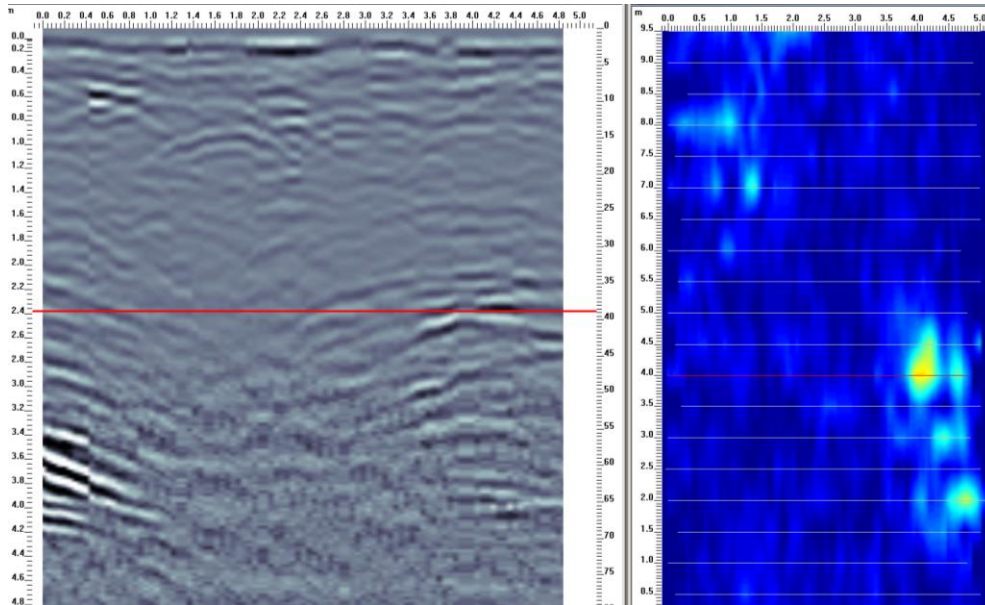


Figure 5.18. Depth slice at the interval of 2.38 m and 2.39 m shows the high-amplitude area interpreted as ejecta elements observed in the GPR profile.

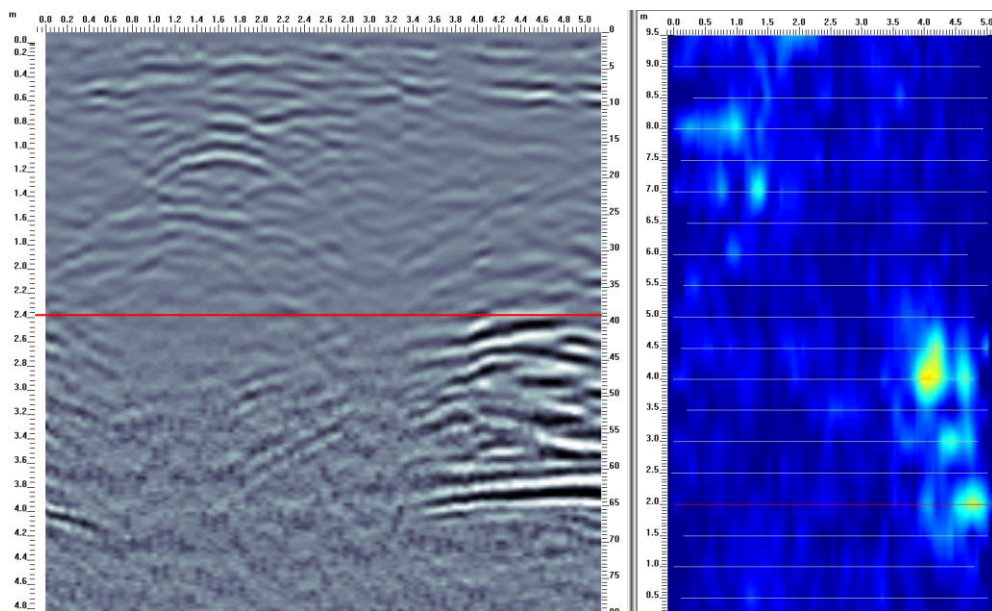


Figure 5.19. Depth slice at the interval of 2.38 m and 2.39 m shows the high amplitude area interpreted as ejecta elements observed in the GPR profile.

In Figure 5.20, we observed a hyperbola at a depth approximately 0.92 m. The corresponding anomaly that was identified by the amplitude is interpreted as an ejecta element with a dimension of 0.5 long and 0.25 m wide. We observed various high-amplitude areas at a depth interval of 0.92 m and 0.93 m in Figure 5.20 and Figure 5.21.

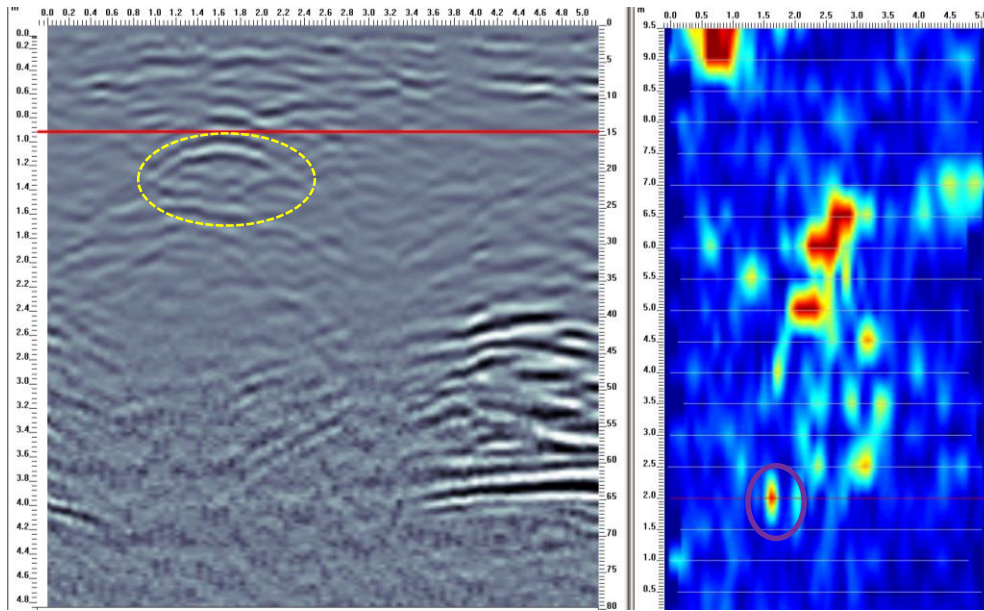


Figure 5.20. Depth slice at the interval of 0.92 m and 0.93 m shows various locations of high amplitude areas interpreted as ejecta elements observed in the GPR profile.

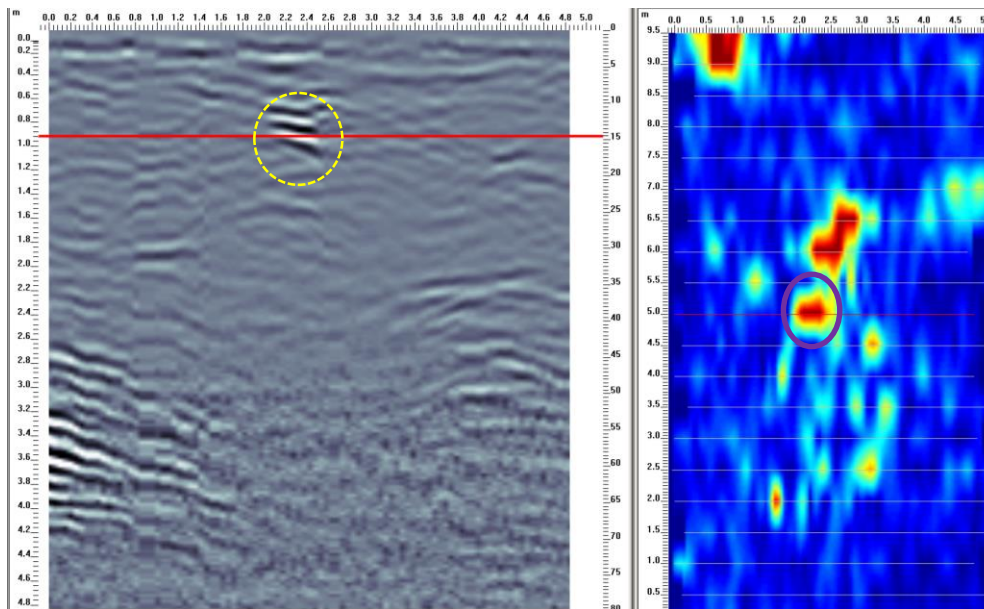


Figure 5.21. Depth slice at the interval of 0.92 m and 0.93 m shows various locations of high amplitude areas interpreted as ejecta elements observed in the GPR profile.

We also observed an anomaly at a depth of 0.84 m in the GPR section as marked by the dashed yellow circle. The depth slice at the interval of 0.84 and 0.85 m shows a high

amplitude area suggesting a bedrock.

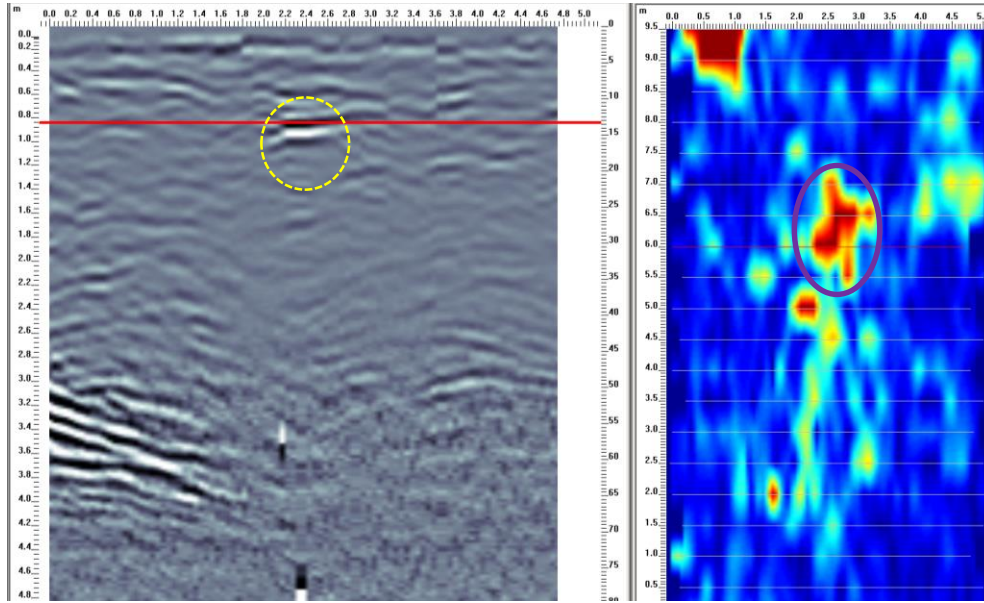


Figure 5.22. Depth slice at the interval of 0.84 m and 0.85 m shows various locations of high amplitude areas interpreted as ejecta elements observed in the GPR profile.

We observed the average change in the thickness of the alluvium in survey grid 8 which runs in the southeast to northwest direction as shown in Figure 5.23. Alluvium thickness is picked at the boundary between the recent alluvium and ejecta. The thickness is within between 40 cm and 60 cm. Thickness contour plot is seen in Figure 5.24.

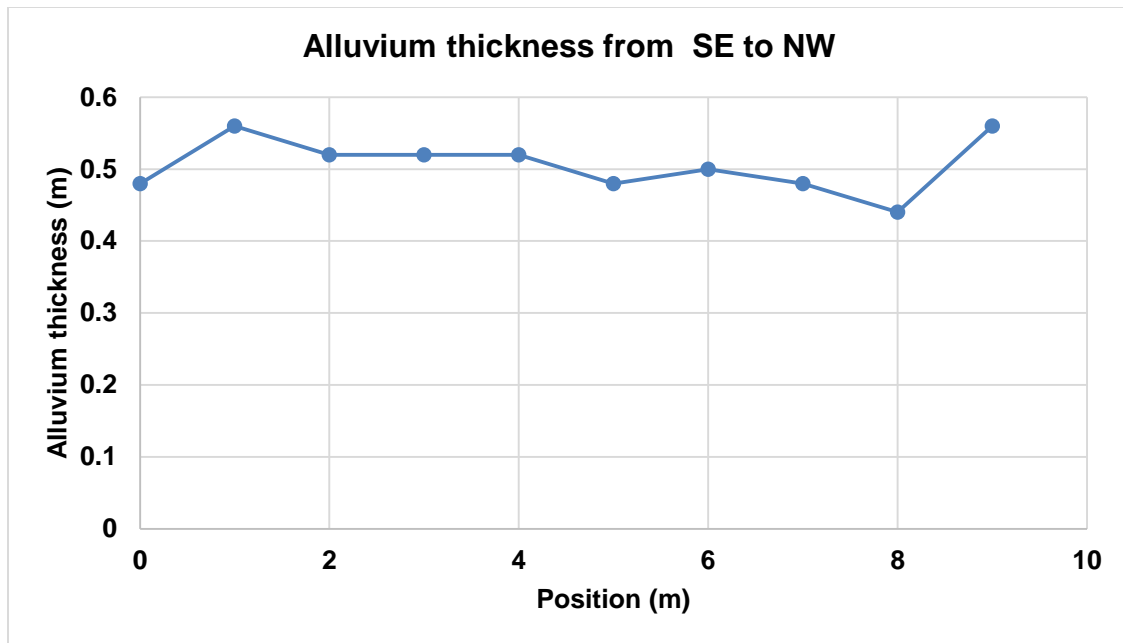


Figure 5.23. The alluvium thickness change from Southeast to Northwest at the survey grid 8.

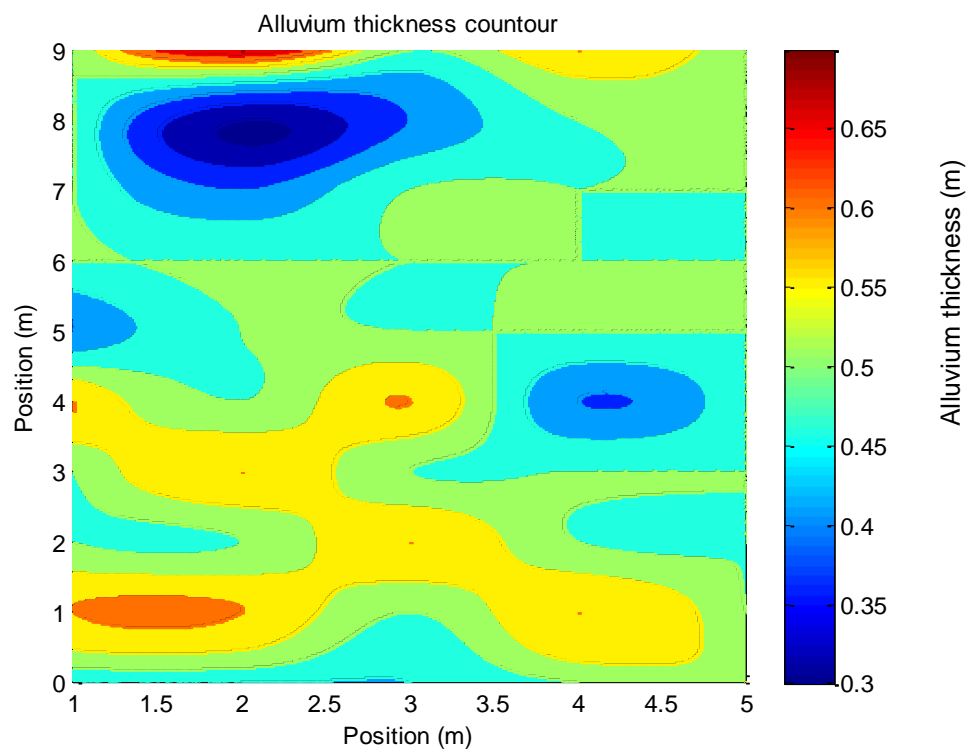


Figure 5.24. The alluvium thickness contour plot of the survey grid 8.

We also observed the average change in the thickness in survey grid 9 which is in the same orientation as grid 8 (Figure 5.25). The observed thickness is between 60 cm and 70 cm. The corresponding contour plot is shown in Figure 5.26.

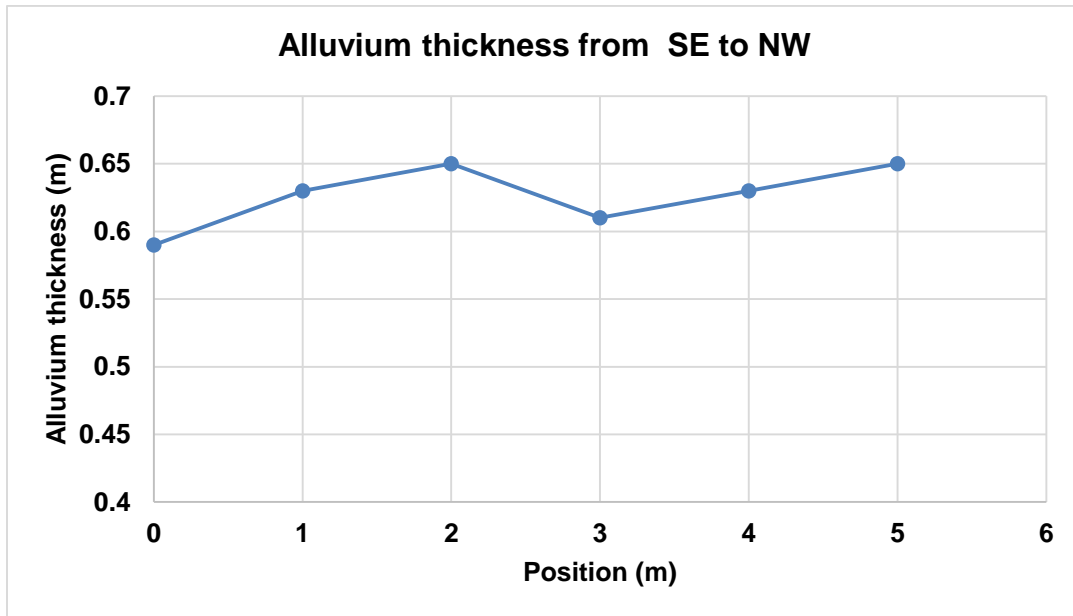


Figure 5.25. The alluvium thickness change from Southeast to Northwest at the survey grid.

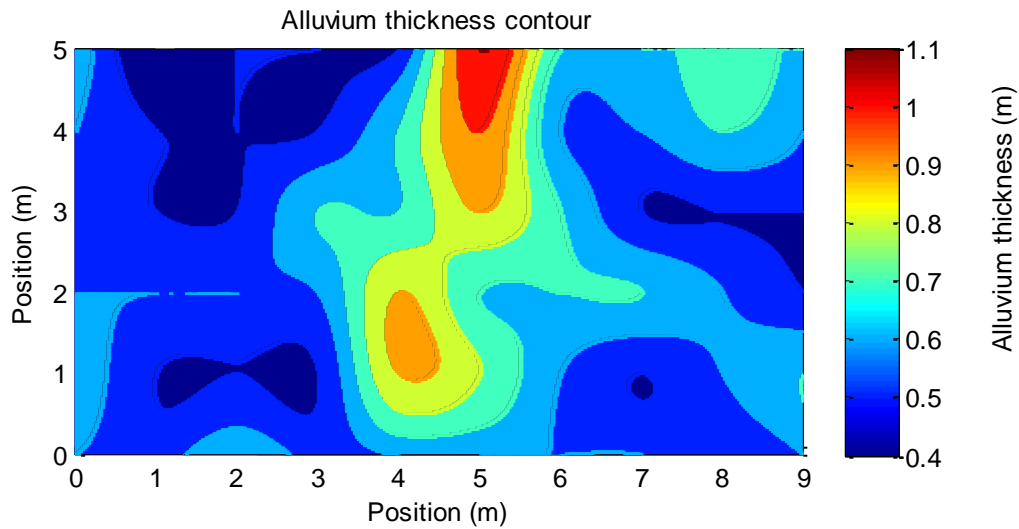


Figure 5.26. The alluvium thickness contour plot in survey grid 9.

We also estimated the alluvium thickness in the perpendicular direction of the survey grid 8 and grid 9 orientation. This was done in survey grid 3. The thickness of the recent alluvium is more irregular across the 100 m length as shown in Figure 5.27. The average thickness fluctuates between 0.8 to 1.6 m along the profile. Figure 5.28 shows the alluvium thickness contour in survey grid 3.

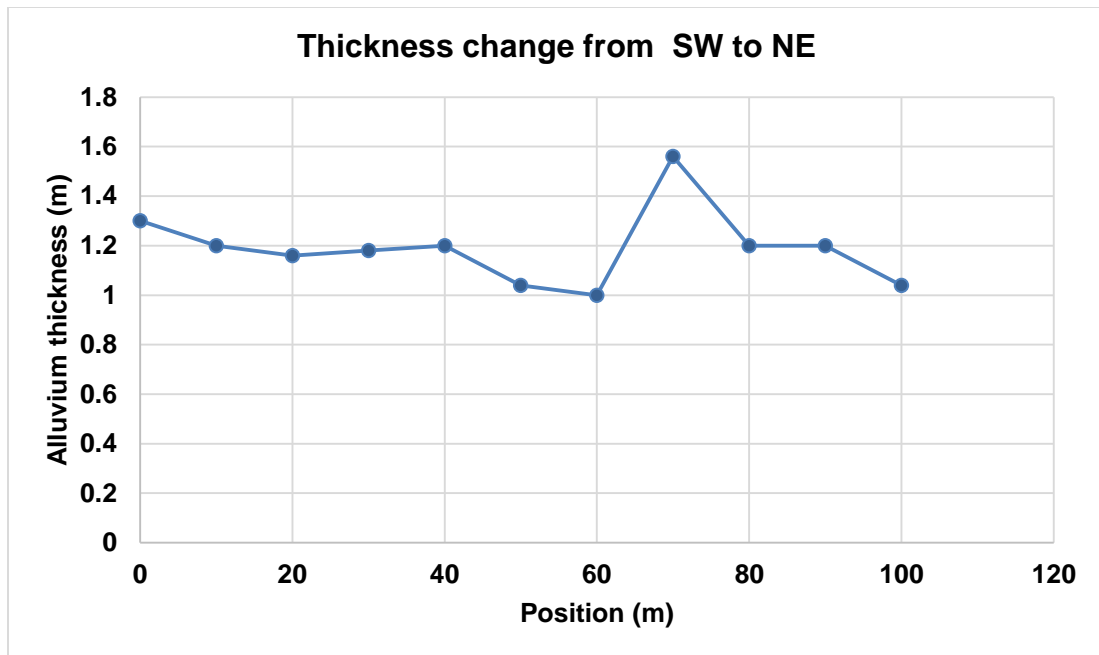


Figure 5.27. The alluvium thickness change from Southwest to Northeast at the survey grid.

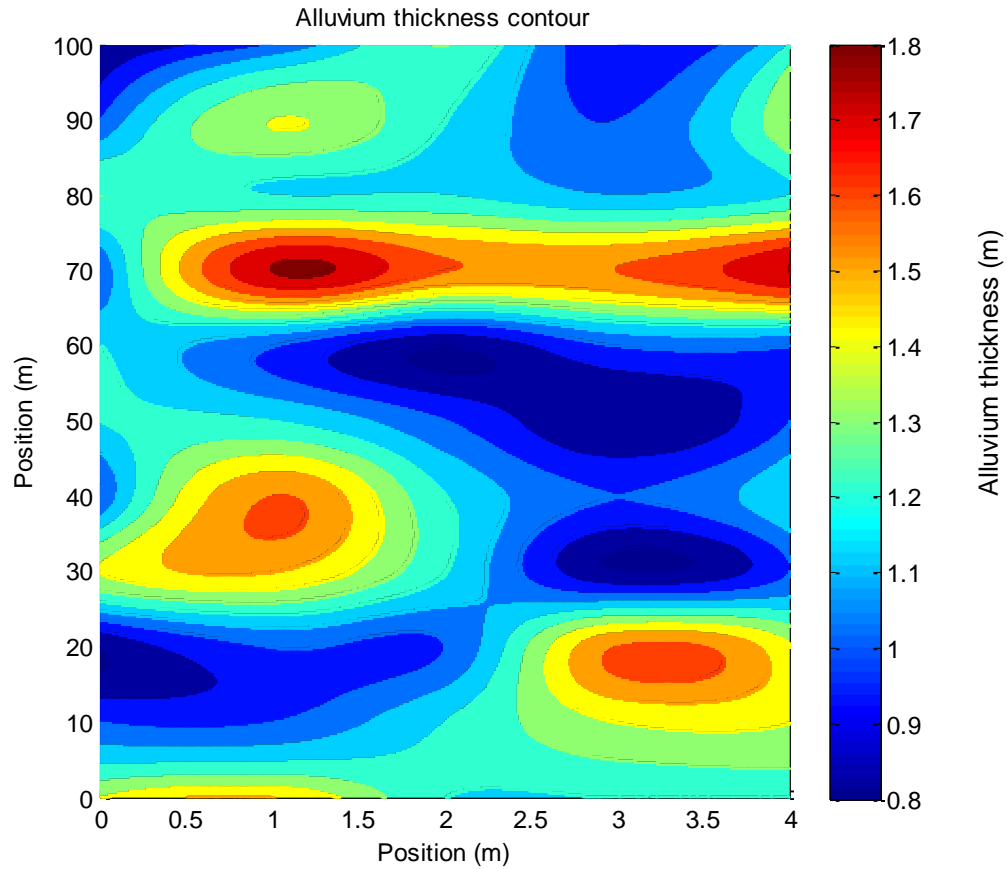


Figure 5.28. The alluvium thickness contour plot in survey grid 3.

In the future, the studies will be more interesting if we have longer radial line that crosses the crater's perimeter.

5.5 Conclusions

3D-GPR data collected at the Barringer (Meteor) Crater in Arizona reveal subsurface layers and geological elements that is useful to determine the geologic setting of the area. The GPR results from various grids at the survey location demonstrate the non-destructive and

high-resolution of the shallow subsurface around the crater impacts. We estimated the subsurface-radar velocity of approximately 0.102 m/ns and the dielectric constant was 8.6. The buried ejecta elements with varying sizes are evident in GPR data in all survey grids to a depth of 4.5 m. The average thickness of recent alluvium in the southeast to northwest direction is within 0.7 m. The observed average thickness of alluvium shows that the thickness shows irregularity in the southeast to northeast direction and it fluctuates between 0.8 to 1.6 m along the profile. The thickness infers the rugose post impact surface. The study demonstrates 3D GPR's ability to distinguish the thickness of the recent alluvium and the buried ejecta elements.

Acknowledgements

We would like to thank the Allied Geophysical Lab team for acquiring the GPR data.

References

- Fredericks, A. D., 2012, Desert Dinosaurs: Discovering Prehistoric Sites in that Big Hole in the ground: The Countryman Press.
- Grant, J. A., P.H. Schultz, 1991, Characteristics of ejecta and alluvial deposits at Meteor crater, Arizona and Odessa craters, Texas: Results from ground penetrating radar, Lunar and Planetary Science, Expanded abstracts, 481-482.
- Grant, J. A., T. A. Maxwell, A. K. Johnston, A. Kilani, and K. K. Williams, 2004, Documenting drainage evolution in Bir Kiseiba, southern Egypt: Constraints from ground-penetrating radar and implications for Mars.

- Khan, S. D., E. Heggy, J. Fernandez, 2007, Case History: Mapping exposed and buried lava flows using synthetic aperture and ground-penetrating radar in Craters of the Moon lava field, *Geophysics*: 72, B161-B174.
- Kring, D.A., 2007, Guidebook to the geology of Barringer Meteorite Crater, Arizona (a.k.a. Meteor Crater): Field guide for the 70th Annual Meeting of the Meteoritical Society.
- Pilon, J. A., R. A. F. Grieve, and V. L. Sharpton, 1991, The subsurface character of Meteor Crater, Arizona, as determined by ground-probing radar: *Journal of Geophysical Research*, 96, 563-576.
- Rowell, C. R., A. Pidlisecky, J. D. Irving, and R. J. Ferguson, 2010, Characterization of lava tubes using ground penetrating radar at Craters of the Moon National Monument, USA: CREWES Research report, 22.
- Roy, S. and R. R. Stewart, 2012, Near-surface seismic investigation of Barringer (Meteor) Crater, Arizona: *Journal of Environmental and Engineering Geophysics*, 17, 117-127.
- Russell, P.S., J. A. Grant, K. K. Williams, L. M. Carter, W. Brent Garry, I. J. Daubar, 2013, Ground penetrating radar geologic field studies of the ejecta of Barringer Meteorite Crater, Arizona, as a planetary analog: *Journal of Geophysical Research*, 118, 1915-1933.
- Stewart, R.R., 2003, Mars in Canada: The NASA Haughton-Mars Project: Devon Island, Nunavut: *CSEG Recorder*, 5, 5-9.
- Turolski, A., 2012, Near-surface geophysical imaging of complex structures: Meteor Crater, AZ and Jemez Pueblo, NM: M.S. thesis, University of Houston, Houston, Texas.

6 SUMMARY

6.1 Summary of contributions

Chapter 2 presented a case study of subsurface culvert imaging at the University of Houston Coastal Center near La Marque, Texas using 5 different antenna frequencies, (100, 250, 400, 900, and 1000 MHz), 2 different systems, and a variety of processing flows to examine the effect of frequencies on key parameters. GPR reflection and CMP surveys were conducted. The La Marque, Texas test survey area gave a dielectric constant of 5.2 from the lab measurement with a corresponding soil velocity of 0.13 m/ns (dry and unconsolidated). Velocities from the common-mid point (CMP) analysis using 100 MHz antenna were between 0.07 m/ns to 0.10 m/ns. The average velocity estimate of the 250 MHz data using the culvert top known depth and the picked time at the zero-offset yields 0.08 m/ns. Various migration velocities were used for the migration of each antenna data (to allow possible velocity dispersion). The 100 MHz data were best migrated using 0.07 m/ns, 0.08 m/ns for the 250 MHz data, 0.10 m/ns for the 400 MHz, 0.10 m/ns for the 900 MHz, and 0.12 m/ns for the 1000 MHz. We found that the best velocity used for the migration showed frequency dependency. We investigated the target detectability, shape, image clarity, propagation distance, and depth accuracy to evaluate the effect of varying frequencies in GPR imaging. The presence of diffraction hyperbolas in the GPR image confirmed that all the antenna frequencies were suitable to image the culverts. 100 MHz, 250 MHz, and 400 MHz defined the culvert top reasonably well and provided an image

which suggested the culverts' shape. The propagation distance decreases as the frequency increases. We found that the depth accuracy is consistent across the frequency except at the 100 MHz antenna. Higher percentage error at the lower frequency such as 100 MHz may be attributable to the higher dispersion and lower resolution image. This study suggests the 250 MHz and 400 MHz system are effective in detecting the culverts, providing the best representation of culverts' shape and size while retaining sharp images. The result highlights that antenna frequency selection is critical and it is controlled by a specific objective of the survey. The study also suggests objective criterion that can be established for selecting the most suitable antenna frequency to image buried culverts in the same soil conditions. If this study were to be replicated in the future, a several aspects of the methodology should be changed. All the data acquisitions for all the frequencies must be done in one day. This would reduce the effects of soil variability due to the changes in the moisture content.

In chapter 3, GPR, TLS, cemetery records, and oral histories were used to locate and characterize unmarked burials at the Mueschke Cemetery in Houston, Texas. The TLS survey was employed for the reconnaissance of the various types of burials in the cemetery. Concrete burials were used after 1940 while wooden burials were common before 1940. Strong correlations of TLS shallow surface depressions with known burials provide substantial motivation to follow-up with a detailed investigation with GPR. Excavation and lab experiments yielded relative dielectric constant (3-10), moisture content (14%-21%), and electrical conductivity (0.36-0.38 S/m) of the location's soil. Understanding the soil grain size, physical parameters, and stratigraphy supports the suitability of using

GPR in the area, the burial characterization on the GPR radargram, and the interpretation. Grain-size experiments indicated that the soil at the survey location is reasonable for GPR, which was subsequently reinforced by the high quality GPR images with a depth of penetration of about 2.5 m and a vertical resolution of 6 cm. Numerical modeling provided a signature of a concrete burial with a flat rectangular top while a wooden burial resembles a typical hyperbola shape. The burial characteristic from 2D GPR template surveys over concrete and wooden burials follow the numerical modeling findings. Three methods were used to estimate the soil velocity: CMP, time-to-depth, and hyperbola fitting. These techniques yielded a soil velocity of about 0.055-0.067 m/ns. 3D GPR surveys produced anomalies that were consistent with headstones, cemetery records, and oral histories. Multiple methods employed to obtain an accurate GPR velocity as a depth conversion is recommended. Taking GPR depth slices overlain on the TLS elevation profile and cemetery records helped to ascertain the locations of the two suspected unmarked graves. The discovery of the two unmarked burials assisted by the joint application of the GPR amplitude depth slice images and TLS surface data recommends that they can serve as direct burial indicators. The results demonstrate the discovery of two unmarked burials including the oldest burial of James West through the geophysical characterization of different burial types using GPR and TLS methods. The results from this work will be used by the Mueschke Cemetery Association as a part of the application process to secure a Texas Historic Marker along with Historic Texas Cemetery Designation. The effectiveness of 2D and 3D GPR template surveys to characterize burial over known burials suggest they can be possibly adopted as a systematic approach to finding historical unmarked burials. The choice of using 250 MHz antenna is sufficient to

probe the burial depth and to produce excellent burial GPR images in Houston soil condition. These results also highlight the power of the integration of GPR and TLS technique in characterizing the concrete and wooden coffin unmarked burials for the historical preservation effort. The presented geophysical approach can also be applied to other near-surface problems where GPR profiles and TLS surface tomography can be integrated, for example, in stratigraphy, hazard assessment, and fracture characterization. Further investigations of TLS dips which do not correlate with known burials by GPR surveys will reveal if the anomalies are not false negative. Also, studies about the GPR response of bones will provide more detailed evidence to detect wooden burials.

In chapter 4, 3D GPR usefulness was demonstrated to image the internal structure of shallow terminal distributary mouth bars and distributary channel in the Cretaceous Ferron Sandstone in Utah. GPR high vertical resolution of 12.5 cm revealed the geometry of architectural element such as small-scale bedding and the extent of major bounding surfaces. The thickness of the individual cross-sets ranges between 8 and 12 cm (measured from the 2D GPR section). The decrease in the cross-set thickness from west to east suggests a gradual thinning downstream. Interpretation of 2D and 3D radar profiles described the heterogeneity of the terminal distributary channel and suggested the complicated depositional environment that exhibit various degree of spatial variability. Three major radar facies were observed in this study includes terminal distributary channel filled with distributary mouth bars, progradational unit mouth bar with a dip angle between 18 to 20°, and laterally continuous basal planar bed deposited in an inertia-dominated river. The 3D GPR image showed a terminal distributary channel fill with a thickness of 1.25 m.

The preserved thickness of the channel fill (~ 1.25 m) also gives a channel depth of about 1.6 m, which conforms to the depth calculation from cross-set thickness. The GPR radargrams were not only capable of imaging the 3D architecture of individual unit bars, but also identified two significant proximal delta-front facies: upper friction-dominated dune-scale cross beds and bar-scale large foresets from lower inertia-dominated basal planar beds. Useful information like the cross bedding direction shown on GPR images can help to predict the maximum directional permeability. Unlike a 2D outcrop, GPR reveals true accretion directions. This helps to define mouth bar growth pattern (downstream, upstream or lateral). Horizontal depth slices obtained from the 3D GPR data help to define the 3D element of the distributary mouth bars. Depositional sequences identified from radar facies were used in reconstructing the 3D geometry of the mouth bars. The 3D-depositional model suggests the direction of the terminal distributary channel. GPR data analysis can facilitate or improve mapping outcrop heterogeneity and help define 3D geometry of sand bodies. The reported radar facies provide a reference for future studies to compare radar reflection pattern with architectural elements in similar outcrops.

In chapter 5, we conducted a 3D-GPR data collected at the Barringer (Meteor) Crater in Arizona to image subsurface layers and geological elements. The GPR results from various grids at the survey location demonstrates the non-destructive and high resolution of the shallow subsurface around the crater impacts. We estimated the subsurface radar velocity approximately 0.102 m/ns and the dielectric constant is 8.6. The buried ejecta elements with varying sizes are evident in GPR data in all survey grids to a depth of 4.5 m. The average thickness of recent alluvium in the southeast to northwest direction is within 0.7

m. The observed average thickness of alluvium shows that the thickness shows irregularity in the southeast to northeast direction and it fluctuates between 0.8 to 1.6 m along the profile. The thickness infers the rugose post impact surface. The study demonstrates 3D GPR ability to distinguish the thickness of the recent alluvium and the buried ejecta elements. To continue the study at Barringer with a longer line in the radial direction to study the variation of thickness of the ejecta interval.

A summary of future recommendations is listed below:

1. Keep detailed rainfall data for before & during the surveys, and try to measure soil saturation in the field more frequently.
2. Analyze the various velocity estimation techniques further with more data to improve the accuracy of these estimates.
3. Provide denser sampling grids or try some of the more sophisticated 3D-signal interpolation techniques currently being used in 3D-seismic processing.
4. Attempt better dip line imaging by designing acquisition to sample in the direction of fastest rate of change of the sub-surface with longer lines and denser samples especially for radial structures such as craters.
5. Try to determine if GPR experiences anisotropic velocities in a layered earth.

7 APPENDIX

A-1 Spherical divergence exponential gain

The following is the MATLAB script was written to apply Spherical Divergence Exponential Gain (Figure 7.1).

```
% Borrowed by Adrian Smith to add paths for data and functions
clear all
more off
add_function_path

% Borrowed by Adrian Smith to check to see if output already exists
fout = 'var/liney1.mat';
if exist(fout,'file') == 2
end

% Borrowed by Adrian Smith to load input data
fin = 'var/liney1.mat';
load(fin);

% Borrowed by Adrian Smith to load input data
ind = min(find(t>=0));
Azero = A(ind:end,:);
t = t(ind:end);
t = t* 1e-9; % Convert to s from ns

% Specify input
refl = Azero;

% Written by Azie Aziz to calculate Spherical Divergence Exponential Gain
% based on https://crewes.org/ForOurSponsors/ResearchReports/1992/1992-11.pdf
% (Fisher et al 1992)

% input of the data
refl = Azero;

% Find dimension of data (number of sample (nt) and number of trace (nx))
[nt,nx] = size(refl);

% Determine sampling interval between samples in a trace
dt = t(2)-t(1);

% Specify Spherical gain constant (n) I am comparing 10,50,100
```

```

n = 500;

% Calculate Spherical Divergence Exponential Gain based on Fisher et al 1992
for i = 1:nx
    for j = 1:nt
        drefl_gain(j,i) = j*refl(j,i)*exp(j*n*(dt/10000));
    end
end

figure

colormap(bone);
subplot(2,2,1);
imagesc([1:nx]*2*dx,[0:nt]*dt,refl);
xlabel('Position (m)');ylabel('Time (ns)');title(['No gain'])
subplot(2,2,2);
imagesc([1:nx]*2*dx,[0:nt]*dt,brefl_gain);
xlabel('Position (m)');ylabel('Time (ns)');title(['Gain with n = 10'])
subplot(2,2,3);
imagesc([1:nx]*2*dx,[0:nt]*dt,brefl_gain);
xlabel('Position (m)');ylabel('Time (ns)');title(['Gain with n = 50'])
subplot(2,2,4);
imagesc([1:nx]*2*dx,[0:nt]*dt,crefl_gain);
xlabel('Position (m)');ylabel('Time (ns)');title(['Gain with n = 100'])
print -djpeg a.jpg

```

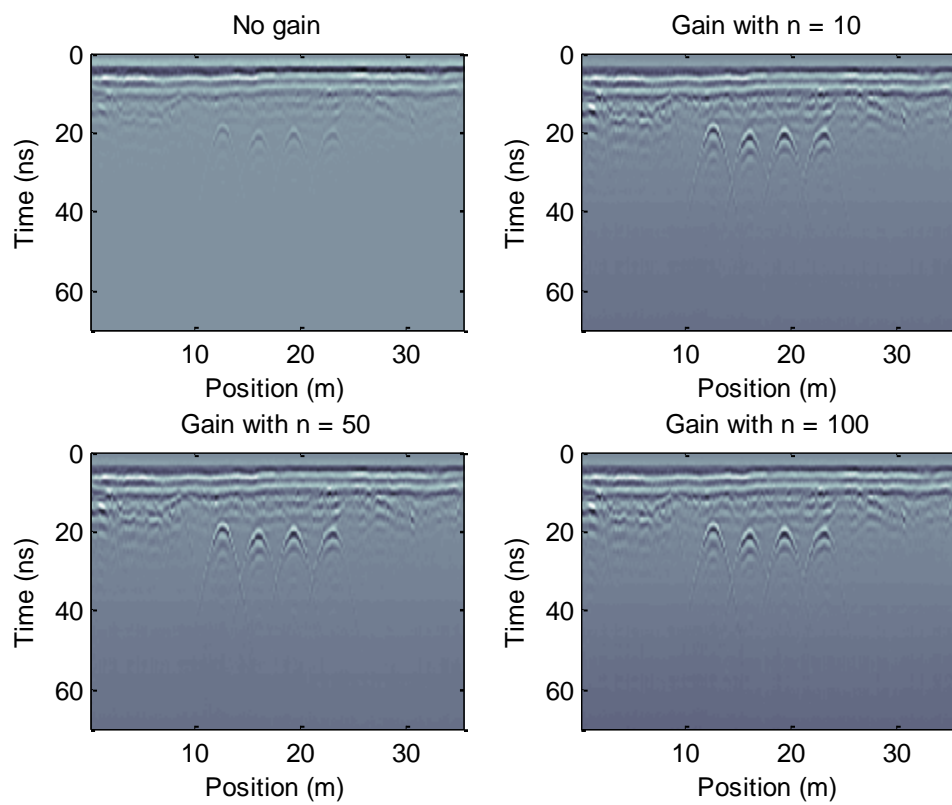



Figure 7.1. 250 MHz data with varying Spherical Divergence Exponential Gain applied.

A-2 Investigation into the interference between culverts

Porsani and Sauck (2006) stated that adjacent steel pipes created interference when the radar wave interacts with one of the pipes (Porsani and Sauck, 2006). This phenomena is observed in the 250 MHz data as shown in Figure 7.2. The interference creates an artifact between the adjacent pipes and the effect of the artifact can be observed through modeling. We modeled the buried culvert numerically to investigate the artifact we observed between the adjacent culverts in Figure 15 and to verify the numerical result.

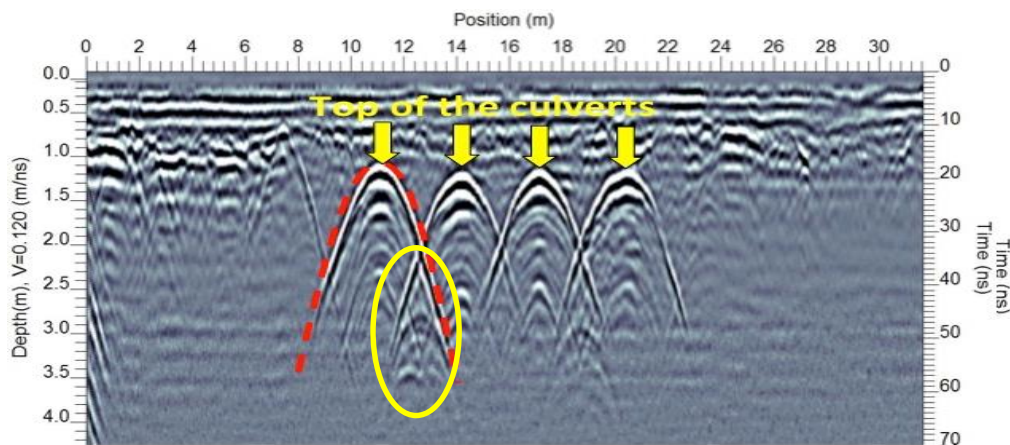


Figure 7.2. The interference between the culverts produces an artifact that appears as a third hyperbola in between the adjacent hyperbolas.

The photograph of the culvert with the dimensions annotated in Figure 7.3 . The dimension of the buried culverts; $h1$ and $h2$ are the depth of the first and the second culvert from the top respectively. The distance between culvert 1 and culvert 2 is d . The radius of the culvert is annotated as r . The red arrow represents the downgoing wave, the green arrow represents the wave from culvert 1 to culvert 2 and the purple is the wave that goes back to the surface from culvert 2.

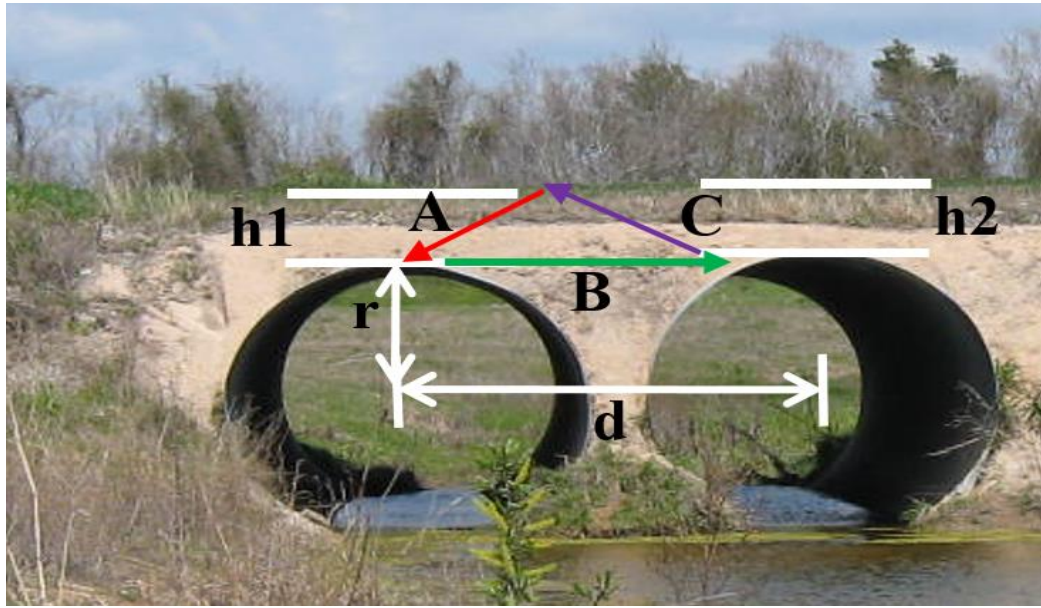


Figure 7.3. The photograph of the culverts with dimension of the buried culverts

We simulated the equations using MATLAB for the wave propagation of X (downgoing wave A), Y (upgoing wave C) and Z is the combination of downgoing, reflected and upgoing wave A, B and C. We presented the result of the simulation in Figure 7.4 and it shows an interference was produced due to the multipathing of traveling wave between the two culverts.

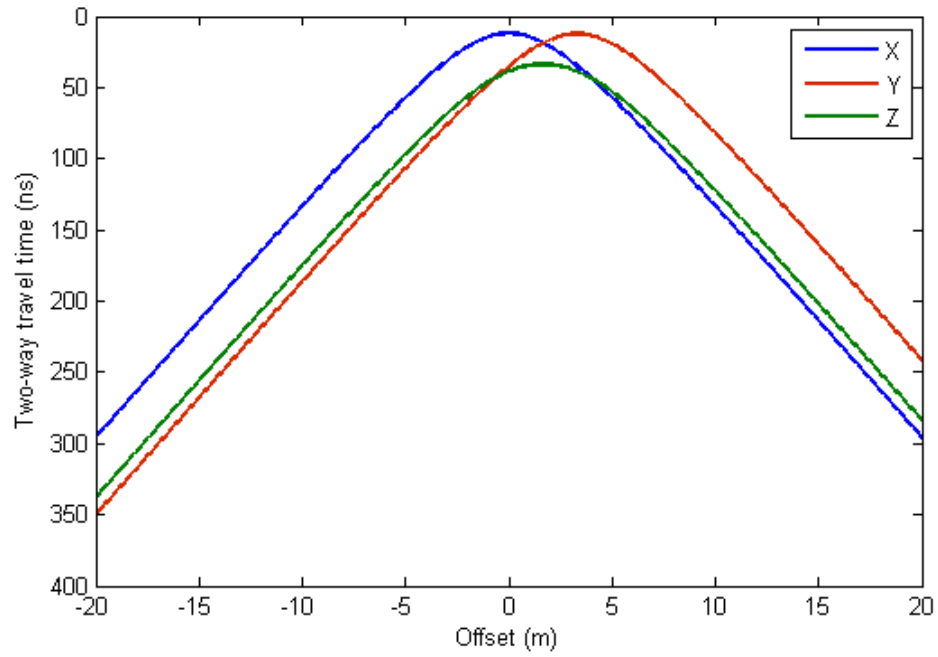
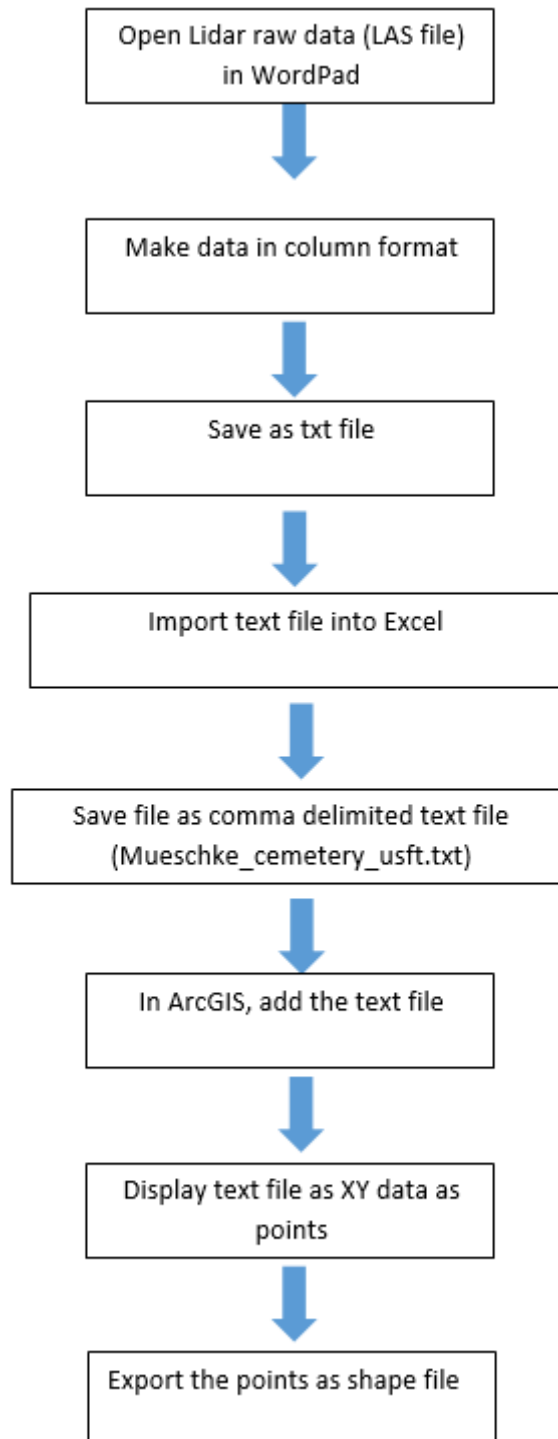


Figure 7.4. The simulated wave propagation based on equations (1), (2) and (3). It can be observed and an interference was produced due to the multipathing of traveling wave between the two culverts.

A-3 TLS processing flow chart

The process in analyzing the TLS data and obtaining the result (high and low points of the elevation) is illustrated in the following flowchart as shown in Figure 7.5.



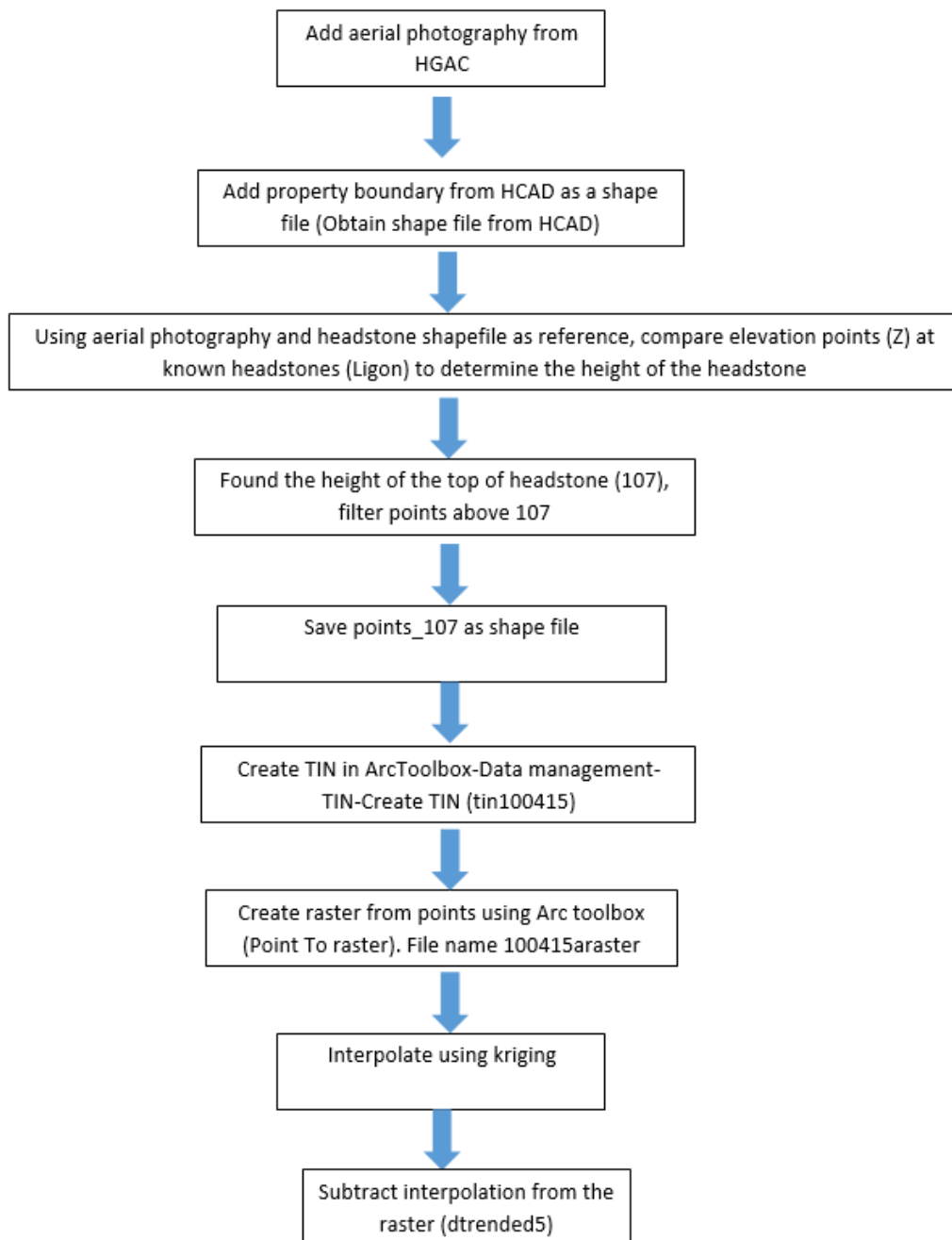


Figure 7.5. TLS processing flow.